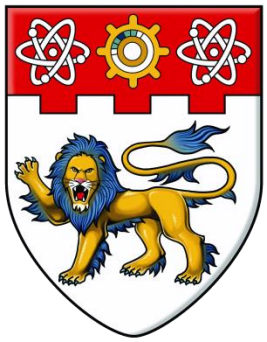

NANYANG TECHNOLOGICAL UNIVERSITY

INTERFACIAL SUPRAMOLECULAR ASSEMBLIES WITH ADVANCED FUNCTIONS

SHAO QI

SCHOOL OF MATERIALS SCIENCE AND ENGINEERING

2013

INTERFACIAL SUPRAMOLECULAR ASSEMBLIES WITH ADVANCED FUNCTIONS

SHAO QI

SCHOOL OF MATERIALS SCIENCE AND ENGINEERING

A thesis submitted to the Nanyang Technological University in partial fulfilment of the requirement for the degree of Doctor of Philosophy

2013

Acknowledgement

I wish to owe my gratitude to all the people who have made this report possible and because of whom this experience has been valuable and fruitful to my exposure in the research field. The project would not have been successfully completed without the help and guidance from all the mentors and staffs at the School of Materials Science and Engineering of NTU, as well as Prof. Wu Jishan and Mr. Zeng Zebing at the Faculty of Science of NUS.

I would like to first take this opportunity to thank the project supervisor, Prof. Chen Xiaodong, for his generous knowledge sharing, invaluable guidance, and advice throughout the whole period of the PhD study. He always shows keen interest in the research topic and encourages me to explore new ideas. It has been a great pleasure to be able to work with and learn from such a knowledgeable and patient advisor.

I would also like to express my heartfelt gratitude to Prof. Lam Yeng Ming, Prof. Huo Fengwei, and Prof. Lee Pooi See, for their invaluable suggestions, expertise and encouragement along the way.

A special thank to Prof. Mu Zhongcheng for sharing his invaluable experiences and providing very useful and important tutoring to me during the

course of my developing process of STM measurement. I would like to thank Dr. Ye Jun for providing the useful simulation results and willingness to discuss with me in one way or another. My gratitude also goes to all the group members, Benhui, Bowen, Dianpeng, Kaihong, Jianjun, Lin, Lili, Yueyue, Yanyan, Yinghui, Yuangang, Yuanjun, and Zhiqiang for their inspiration, share of knowledge, and encouragement during my PhD study.

Finally, I would like to thank my parents, husband, and friends for their unfailing love, understanding, and encouragement throughout my study.

Abstract

Supramolecular assemblies have a key component with regards to supramolecular electronics, the study of its self-assembly behavior as well as functional properties will bring great impact in the sense of understanding and improving the performance of such devices from a fundamental point of view.

We study supramolecular assemblies of hexa-peri-hexabenzocoronene (HBC) derivatives bearing different substituents, adsorbed on highly oriented pyrolytic graphite (HOPG) by using scanning tunneling microscopy at the solid-liquid interface. Two effects of intermolecular interaction were found to play a significant role in controlling the interfacial supramolecular assembly of these C_3-symmetric HBC derivatives at the solid-liquid interface. One is hydrogen bonding interactions; the other is intermolecular dipole-dipole interactions. This work demonstrates how intermolecular interactions could enable fine control over the self-assembly of disk-like π-conjugated molecules. Furthermore, a host-guest system is established by utilizing the hydrogen bonding assisted honeycomb network established from HBC derivatives, and by incorporating coronene inside the porous structure, it offers potential applications such as use as molecular rectifiers in the future.

Besides the bottom up approach of self-assembly of rigid molecules like HBC derivatives to establish a 2D π-conjugated structure, graphene has been

viewed as the alternative material from the top-down point of view to possess 2D large π-conjugated area for promoting electron transport. By chemically modulating the monolayer graphene devices, positive photoreponse has been achieved, and with the help of conductive atomic force microscopy (C-AFM), the photoreponse performance could be correlated to the degree of functionalization at spatial distribution with nanoscale resolution. The mechanism was found to be desorption and adsorption of gas molecules in light and dark conditions; the positive photoresponse is due to the n-type doping behavior after functionalization. From the spatially distributed correlation between photocurrent and functionalization, it makes us realize that every functionalized pixel (~ nm^2) offers a positive photoreponse, and the overall device performance is equivalent to the photoresponse of each individual pixel. This demonstrates that it is reliable to use the chemical method to generate a photoreponse from a 2D material like graphene.

In order to explore further the relationship between the assembly structure behavior and its functional properties, π-conjugation interrupted frameworks (CIFs) have been studied and it was found that they are not only offering great three dimensionality, but are also sensitive to dopants and post-modification of their nanostructure based thin film with diazonium salt, which rendered their electrical properties highly tunable by up to two degrees of magnitude. Hence, it has been demonstrated that the π-conjugation-interrupted frameworks and their doped counterparts broaden the options for organic electronics. As a result of the H-shaped conformation and photosensitive properties of CIFs, we envisage their

potential role as active components of memory devices and photodetectors in the future.

In conclusion, this study offers valuable platforms by rational designing the self-assembly building blocks for the development and advancement in the field of supramolecular assemblies. It demonstrates the correlation between their structural behavior and resulted functional properties by means of scanning probe microscopes. HBC derivatives are designed for the bottom up approach of generating 2D π-conjugated area for molecular electronics; while graphene has been referred as the top-down alternative of producing such extended 2D structures and with chemical modulation, photoreponse of such devices are achieved with great repeatability. From 2D to 3D, a class of π-conjugation interrupted dendrimers exhibits tunable electrical properties by decorating small molecules. Finally, the perspectives on future directions and unsolved challenges are also addressed.

Table of Contents

List of Figures

Page

List of Schemes

Page

List of Tables

Page

List of Charts

Page

Chapter 1 Introduction

This chapter first introduces the fundamental background of supramolecular assemblies, followed by description of how to characterize the structural behavior and functional properties by the family of scanning probe microscopies. Next, the state-of-art of particularly interesting self-assembled molecules at solid-liquid interface and possible applications in the field of molecular electronics are reviewed. Moreover, some other emerging techniques for optimizing the performance of molecular electronics consisting of supramolecular assemblies are discussed. Lastly, the research motivation and objectives, as well as the organization of the thesis are presented.

1.1 Introduction to Supramolecular Assemblies

1.1.1 Overview

Supramolecular assemblies have been intensively studied, due to their unique behavior that allows simple molecules as the building blocks to generate structurally and functionally complex entities for applications ranging from the field of physics, to chemistry and even biology.[1-17] Nowadays, supramolecular assemblies have developed more broadly cross many disciplines, attracting chemists for their complex yet organized structures, and scientists are constantly searching for novel molecular building blocks possessing remarkable properties, such as electrical, optical, optoelectronic, and catalytic and so on. Biologists are

more interested in investigating the possibility of utilizing biomolecules in establishing bio-active organs. Hence, it surpasses the conventional disciplinary boundaries of science and approaches a highly interdisciplinary area. And more importantly, it makes programmable materials to be generated in an easy and controlled manner.[18-21]

Among the different systems of supramolecular assemblies, one attractive direction focused on the disc-like π-conjugated molecules, providing tailored electronic properties of their flat conjugated systems which can be varied dramatically through synthetic modification of their sizes and topologies.[22-23] For example, hexa-*peri*-hexabenzocoronene (HBC) can self-assemble into highly ordered monolayer on the substrate surface and work as an active component for molecular electronics, such as molecular rectifiers and single-molecule chemical field-effect transistors.[22, 24-25] In this case, the ability to control the interfacial supramolecular architectures formed by disc-like molecules is important to promote the development of such molecules in molecular device application.

From nanoscience to nanotechnology, a number of examples have been demonstrated regarding using molecules for building up a molecular or supramolecular electronic device.[26-30] In particularly, a tetrathiafulvalene (TTF) derivative has been designed and self-assembled into a 1D nanowire at HOPG-1-octanoic acid interface. A large rectification behavior was observed by STM on top

of the TTF moieties, which suggested such a system could be employed in nanoscale molecular devices.[31]

1.1.2 Supramolecular Chemistry

Generally speaking, molecular chemistry, the chemistry of the covalent bond, takes into consideration the rules and forces that guide the structures, properties and transformations of individual molecules. Supramolecular chemistry has been referred as "chemistry beyond the molecule", which means that the higher complexity of assembled organization results from the association of at least two or more molecules held together by intermolecular interactions.[32-34] Therefore, one could understand these two concepts in this way: molecules are concerned with atoms and covalent bond, while supramolecules are interested in molecules and intermolecular interactions.

The advantage of supramolecular chemistry can be considered as the whole is greater than the summation of individuals; the final outcome of supramolecular assemblies are better than the individual ones.[35] We can learn from nature, which usually uses simple and repeatable units to build up highly complex supramolecular assemblies, such as ferritin.[36] Such assemblies are generated via weak intermolecular interactions, such as hydrogen bonding,[1-4, 14, 37-38] π–π interactions,[11, 13] metal-ligand interactions,[5, 7-9] and van der Waals interactions[10] to hold the subunits together. Similar to nature, directional bonds have also been

used by synthetic chemists, such covalent bonds, electrostatic attractions, and so on.[15, 39]

Even a slight variation of the molecular building block results in a tremendous effect on the final supramolecular assemblies, for example a basic fluorinated and non-fluorinated dendron have completely different outcome after supramolecular assembly, shown in Figure 1.1. From top to bottom, the molecular building block is self-assembled and finally self-organized into supramolecular assemblies. The basic molecule is shown in the middle of the figure. The non-fluorinated dendron on the upper left self-assembled into spherical assemblies, and then self-organized into a cubic structure, while the partially fluorinated dendron on the upper right self-assembled into a columnar structure and then self-organized into a hexagonal liquid-crystalline lattice.[40] Therefore, by designing and synthesizing molecular building blocks with specific functional groups, one can fine tune the intermediate and final supramolecular assemblies to a great extent.

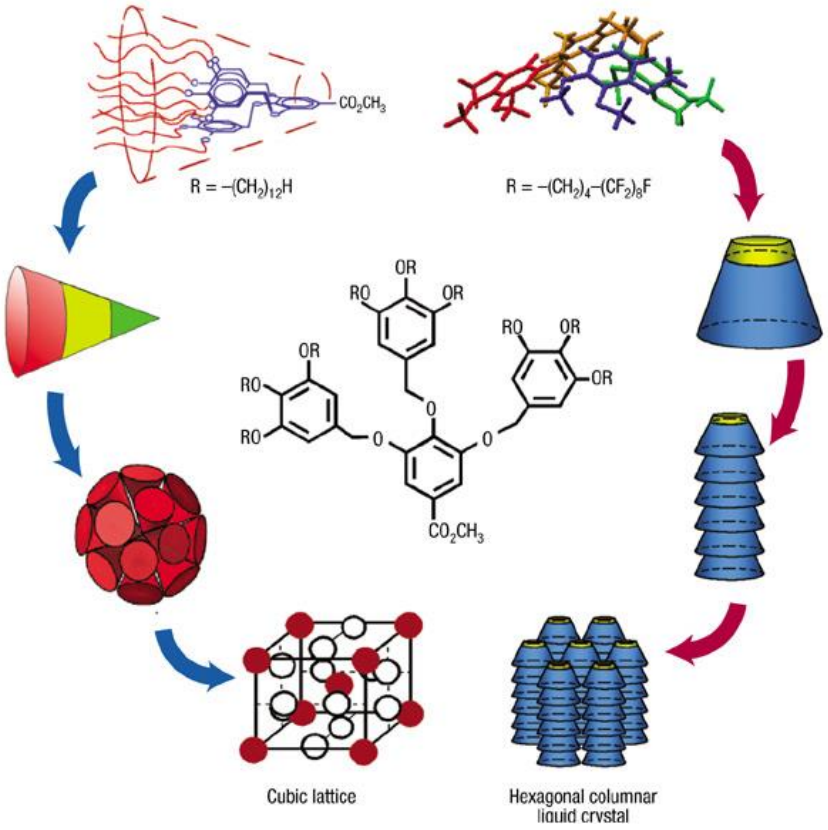

Figure 1.1 Supramolecular assemblies of the second generation dendrons. Left: non-fluorinated dendron as basic building blocks and forming a cubic lattice in the end; right: partially fluorinated dendron forming a hexagonal columnar liquid crystal.[40] Reprinted with permission from reference 30. Copyright 2003 Wiley-VCH Verlag GmbH and Co. KGaA.

1.1.3 Interfacial Supramolecular Assemblies

Among the field of supramolecular assemblies, one of the important aspects is interfacial supramolecular assembly. It provides the guidelines on how to design

molecular building blocks in order to achieve a balance among molecule-molecule, molecule–substrate, molecule–solvent, and solvent–substrate interactions.

Here is an example of solvent effect on the final outcome of interfacial supramolecular assemblies at the solid-liquid interface, which is caused by the interaction among substrate-solvent-molecule. Trimesic acid (TMA, 1,3,5-benzenetricarboxylic acid) has been found to exist in a polymorphism between flower and chicken wire structures. It was observed that the TMA molecules form a chickenwire structure at longer chain solvent, while the flower structure is discovered for TMA in shorter chain length solvent. So by selecting different solvent, the structures of supramolecular assemblies can tune to a large extent.[41]

Solvent-dependent polymorphism was also observed for an extended analogue of TMA, 1,3,5-benzenetribenzoic acid (BTB),[42] which demonstrates that the influence of solvents on the formation of porous networks is a common phenomenon. Figure 1.2 shows both the chemical structure of TMA and BTB in (a) and (b), and BTB molecules self-assembled into two polymorphs, exhibiting an oblique or hexagonal unit cell depending on the alkyl chain length of solvent molecules in Figure 1.2 (c) and (d). Therefore, either rectangular or circular cavities are formed at graphite-solvent interface. In order to correlate the relationship between the nature of solvents and polymorphism, it was found that the dielectric constant, polar effect, as well as viscosity of the solvent all have influence on the final structure.

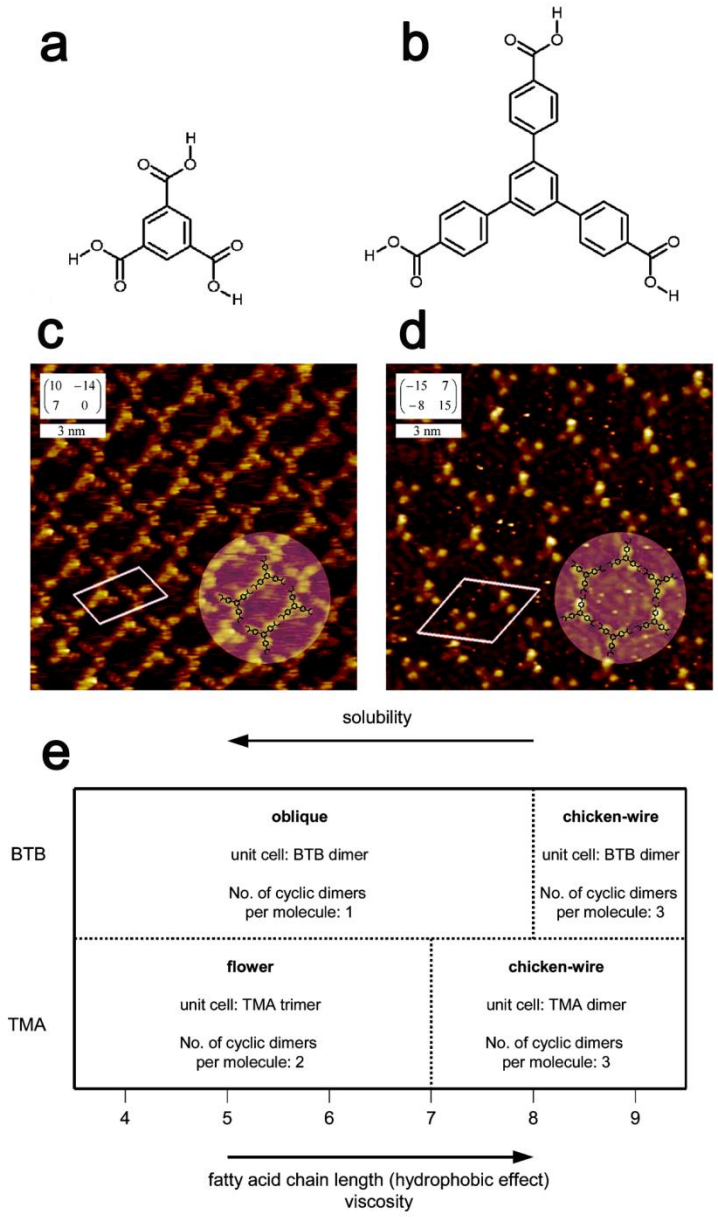

Figure 1.2 Solvent effect for interfacial supramolecular assemblies: (a) and (b) Chemical structure of molecule TMA and BTB. (c) and (d) STM images of the two polymorphs for BTB self-assemblies with oblique and honeycomb unit cell. (e) The general guidance on the effect of solvent towards the structure of TMA

and BTB at the interface.[42] Reprinted with permission from reference 32. Copyright 2006 American Chemical Society.

Now that the solvent's great influence on final supramolecular assemblies has been discussed, let's now look at the effect of the molecule itself. It was found that it is possible to have different interfacial supramolecular assemblies at solid-liquid interface for the same molecular building block, (Figure 1.2). For instance, if we change the concentration of the molecular solution, it controls the formation of supramolecular architectures; a transition from linear pattern to a porous structure is observed when the concentration is changed from high to low for alkoxylated dehydrobenzo[12]annulenes (DBA-OC_n) self-assembled structures at solid-liquid interface.[43]

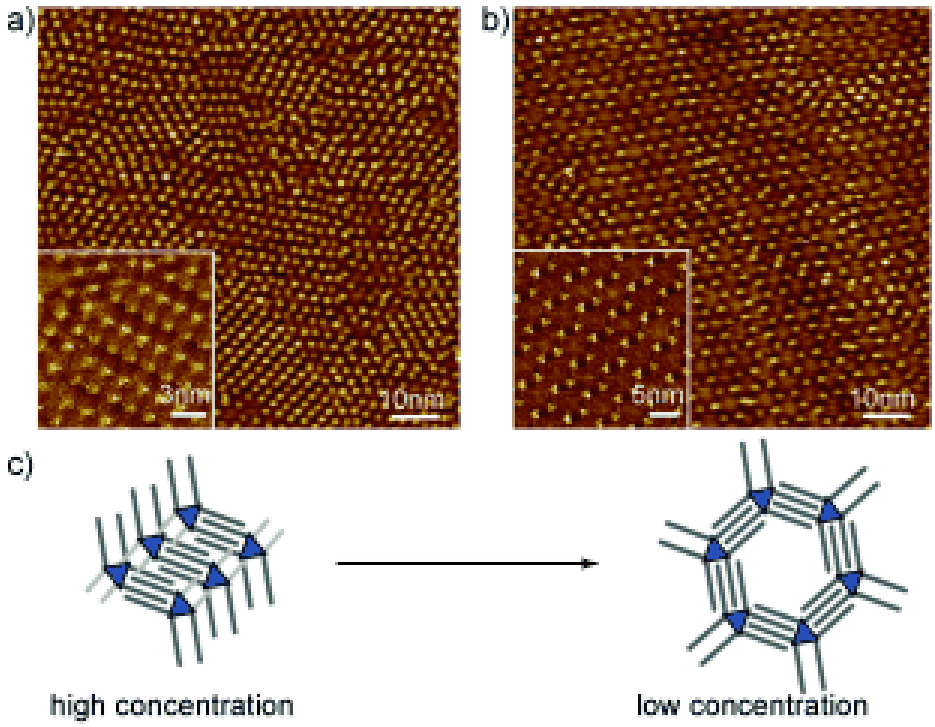

Figure 1.3 STM images of DBA-OC_{16} at high and low concentrations for (a) and (b) respectively. Under high concentration, it forms a linear pattern, while a honeycomb network is formed under low concentration. c) The molecular model for explaining the transition between high and low concentrated condition.[43] Reprinted with permission from reference 33. Copyright 2008 Wiley-VCH Verlag GmbH and Co. KGaA.

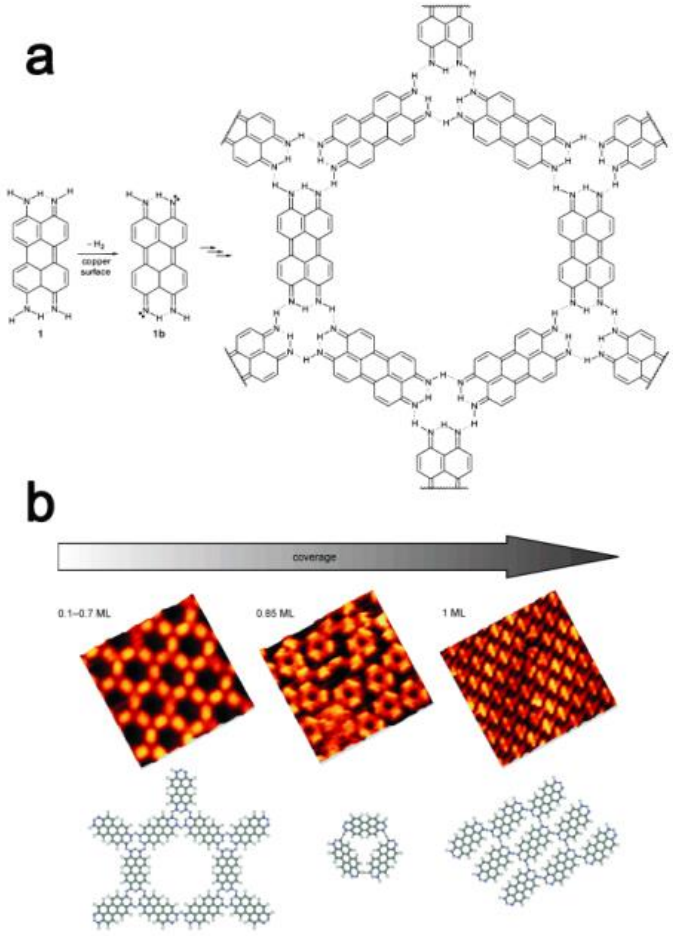

Figure 1.4 Surface coverage effect. (a) Thermally generated compound 1b on a

Cu(111) surface. (b) STM images and proposed molecular model of supramolecular assembly at different coverage of 1b.[44] Reprinted with permission from reference 34. Copyright 2005 Wiley-VCH Verlag GmbH and Co. KGaA.

Another factor influencing 2D interfacial supramolecular assemblies is the surface coverage. For instance, 4,9-diaminoperylenequinone-3,10-diimine (DPDI) has been used as molecular building block, which was deposited on Cu(111) surface and then annealed at 300 ℃ with different coverage ranging from less than 0.7 monolayer (ML), to 0.85 ML, to a full coverage 1ML. The DPDI molecule undergoes dehydrogenation to generate an auto-complementary compound 1b during the annealing process shown in Figure 1.4 a. By increasing the surface coverage from less than 0.7 ML, to 0.8 ML, till 1 ML, the corresponding supramolecular structures change from honeycomb network, to trimeric structure, to four adjacent monomers linked-up molecular motifs.[44]

From the above examples, one could see that there are many factors influencing the final structure of interfacial supramolecular assemblies either at solid-liquid interface, or solid- vapor interface. Even with the same molecular motif, it is possible to have different supramolecular structures by variable concentration, or surface coverage. Therefore, it is crucial to understand the root cause governing the behavior of interfacial supramolecular assemblies, not only for the purpose of predictable structure, but also the functional properties, and more

importantly it will provide significant guidance on how to design and synthesize suitable molecular building blocks for specific applications.

1.2 Working Principles of Scanning Probe Microscopy

Supramolecular chemistry offers plenty of advantages to the chemistry of target molecules, and by utilizing the weak intermolecular interaction. It is one of the easiest and fastest ways to establish supramolecular assemblies so far. In order to understand the underlying principle for the assembly behaviors at different interfaces, such as solid-liquid, solid-vapor and liquid-vapor, a family of scanning probe microscopy techniques has offered great possibility and pushed forward the development of supramolecular assemblies from the molecular level.[45]

1.2.1 Scanning Tunneling Microscopy

The scanning tunneling microscope (STM) was invented by Gerd Binnig and Heinrich Rohrer in 1981, which allowed researchers to see surface features at atomic resolution,[46-47] and then these two inventers shared the 1986 Nobel Prize in Physics.[48-49] The principle of that instrument is governed by the phenomenon called “tunneling”, which describes the current passing through the gap between tip and sample, and this phenomenon can happen only at a distance close to 10 Å. The direction of current flow depends on the polarity of the bias applied. The value of current at different position is collected to obtain an STM image. From the

functional properties point of view, a STM image not only reviews the topography of the sample surface, but also the electronic state, or in another word, the local density of state of the sample. Therefore, STM can also be used as a spectroscopic tool, which enables the ability to obtain information like electronic properties of molecular assemblies or structures at the single atomic and molecular level.[50-51], 44

STM is a powerful instrument with the submolecular resolution, and it has been proved to be useful for understanding the intermolecular interactions for supramolecular assemblies at different interfaces, such as solid-liquid, and solid-vapor[52] However, in order to not only understand but also control or even design a programmable molecular system, there is still plenty of work that needs to be done. [53]

At the early stage of development of the STM family, the STM can be categorized into three types, ultrahigh vacuum STM (UHV STM), ambient STM and electrochemical STM (EC-STM), although spin-polarized STM and inelastic electron tunneling spectroscopy (IETS) and some new members of the family emerged recently. For different research purposes, different instruments are selected accordingly. For instance, UHV STM is able to detect the reconstructed semiconducting or metal surface, such as 7×7 reconstruction on Si(111);[54] catalysis research,[55-58] nano-patterning,[59-62] and manipulation of atoms and molecules[63-73] and so on.[74] Hence, all these researches help in understanding supramolecular assemblies at the atomic scale.

Ambient STM can investigate samples at solid-liquid interface and solid-vapor interface. Self-assembled monolayers[75-76] (SAMs) are readily imaged by UHV STM or ambient STM at solid-vapor interface. When comparing self-assemblies formed at solid-liquid interface with those obtained at solid-vapor interface, self-assemblies are readily repaired at solid-liquid interface and easier to obtain repeatable images over a long period of time than those at solid-vapor interface. This is because of the excellent recoverability of the assemblies from the liquid reservoir of molecules.

Another category of STM is EC-STM, which mainly investigates the electrochemical properties of interest at the atomic scale in a liquid environment. For this technique, atomic resolution could be obtained like the ambient STM, moreover, by applying different bias or voltage pulse to the working electrode, tip or sample, the molecular structure could be controlled precisely. Initially, a two-electrode system was used to operate EC-STM in liquids,[77-78] and developed into a four-electrode system later on which allows the STM tip with an insulating layer as one electrode, and substrate to be the working electrode, and then reference electrode and counter electrode to provide current flow and potential in the circuit.[79-84]

By utilizing EC-STM, the mechanism of generating single molecular wires by electrochemical epitaxial polymerization could be understood. The one-

dimensional molecular wire is one of the most popular supramolecular assemblies due to its unique structure, and possibility to be fabricated into 1D molecular electronics. It was found that iodine plays a very important role, and nucleation of monomers and then propagation is the main principle. The detailed mechanism is shown in Figure 1.5. In the electrochemical cell containing 3-butoxy-4-methylthiophene (BuOMT) (monomer) and iodine, positive voltage pulses were applied to the Au working electrode. A value of 1.4 V has been found to form a cation radical from the monomer, and later the conjugated polymer starts to propagate.

As for the mechanism of the electrochemical epitaxial polymerization, the polymer-adsorption mechanism has been proved to be wrong. The new proposed mechanism is surface propagation method, meaning that the monomer will start to nucleate on the iodone adsorbed Au (111) surface first, then later propagate and form single polythiophene wires. This proposed mechanism is verified by experiments with applying different conditions in the electrochemical cell, and then monitoring the reaction in-situ by STM. This demonstrates that not only fabrication of the desirable polythiophene wires is realized, but also the underlying mechanism is understood. More recently, EC-STM has even been applied in the field of biology to understand fundamental phenomena that puzzle us, like the detection of nuclei, understanding of single-redox proteins, or for the application of biosensing and so on.[85-89]

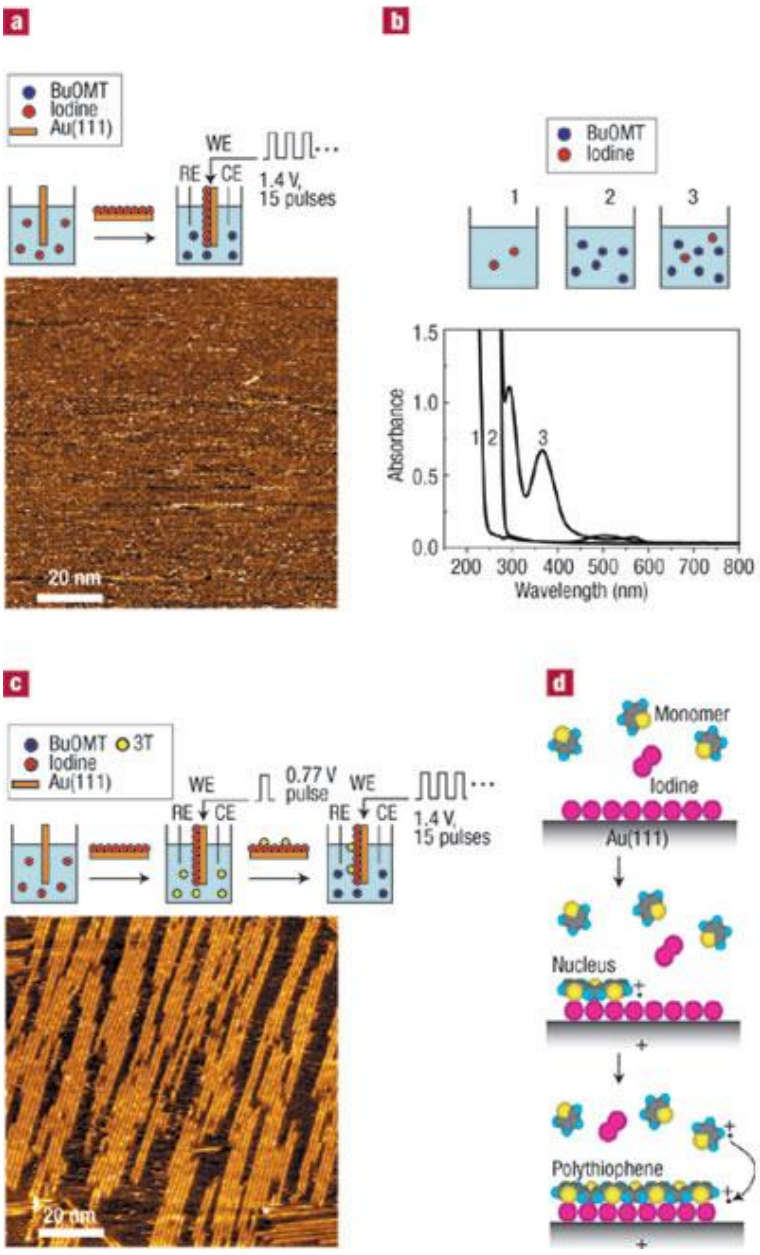

Figure 1.5 (a) The STM image of system containing iodine adsorption and electrolyte containing monomer BuOMT. (b) With adding iodine inside the electrolyte, adsorption peaks appear. c) STM image of system with implanting nucleus. d) Proposed mechanism of electrochemical epitaxial polymerization.[90] Reprinted with permission from reference 81. Macmillan

Publishers Ltd, Nature Materials, copyright 2004.

1.2.2 Atomic Force Microscopy

One of the disadvantages of STM is that the sample has to be conductive or semiconductive; fortunately, the invention of atomic force microscope (AFM) [91] allows us to image almost any type of surface, such as polymers, ceramics, mica, and biological samples. The working principles of AFM rely on the interatomic van der Waals interactions between the AFM tip (cantilever) and the sample. The bending motion of cantilever could be detected by a photodiode system. Nowadays, different modes of AFM and STM have been used in order to understand the fundamental phenomenon or driving force for specific applications, such as molecular electronics,[92-94] nano-structured organic field effect transistor,[95-96] and organic photovoltaics[97-98] etc.

One of the interesting fields that researchers have been focusing on is to use AFM to study biological specimens, which are often referred to as the supramolecular assemblies from the nature itself, like deoxyribonucleic acid (DNA), protein, and bacteria and so on. For instance, silanated mica has been selected to be one of the best substrates to image biomolecules, like DNA, however the interaction between the DNA and mica is very strong, which leads to entanglement of DNA molecules. In order to solve this problem, a method called "molecule combing" was created. By applying a liquid onto the substrate in a

paralleled fashion, the alignment of DNA molecules will be realized, so that straight and well aligned DNA strands could be imaged by AFM.[99-101]

More recently, the way of manipulating DNA in a controlled manner or understanding some dynamic process of DNA related biological structures have drawn much attention.[102-105] For example, by using a streptavidin modified AFM tip, the topography and recognition events could be imaged at the same time. In Figure 1.6, it explains that the topographic image reveals a bump during encountering of individual molecules. The AFM tethered tip experience a drag when leaving away from the molecule, and results in a trough in the amplitude oscillation. And it shows the recognized and un-recognized molecules in dotted and solid circles in B for comparison. It is even clearer to understand the red dot as the tagged molecule event on the composite image at B-4. A control experiment of AFM tip without biotin was also performed and didn't show any tag event in C. Hence, it has demonstrated that AFM is a powerful tool to characterize designed DNA nanostructures, which could be used as immobilization agents in the research fields of biosensing, biophysics, and cell biology.

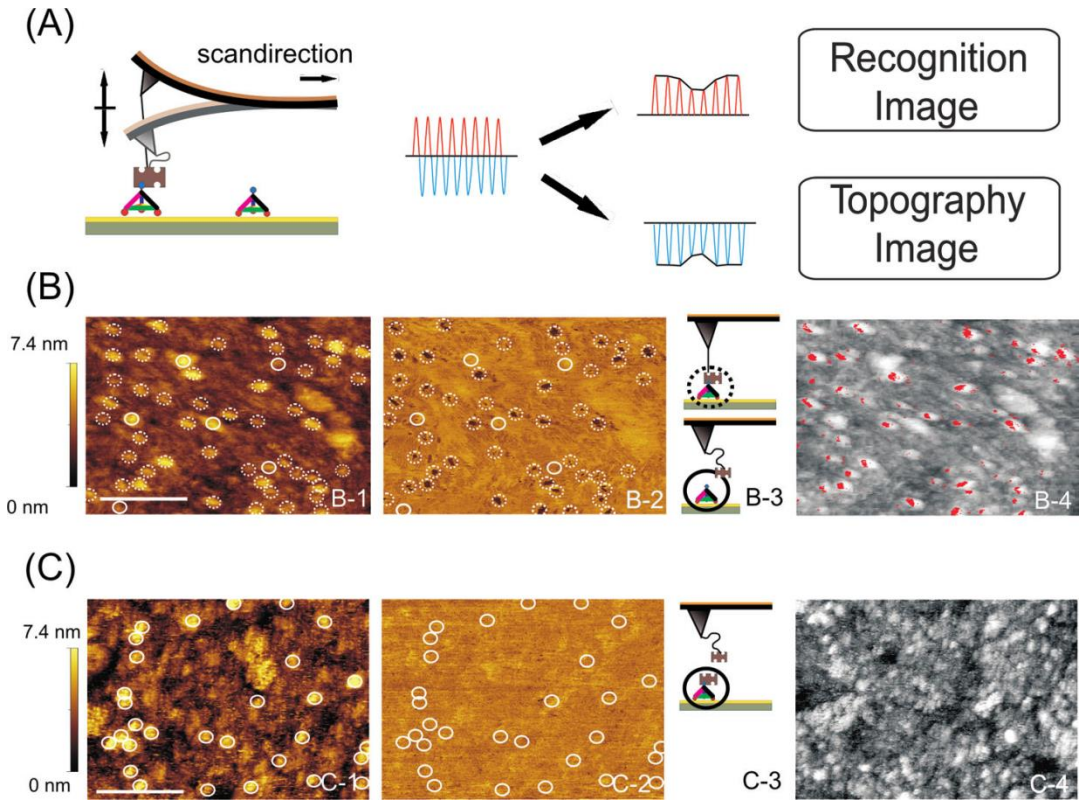

Figure 1.6 (a) Schematic illustration of the topography and recognition imaging principle. (b) The tetrahedra with and without recognition is marked in dotted and solid circle respectively. (c) Without streptavidin, the recognition event is not happening. [105] Reprinted with permission from reference 96. Copyright 2011 American Chemical Society.

1.2.3 Conductive Atomic Force Microscopy

Although the STM can resolve individual atoms on conducting surfaces,[106] the ability of AFM to topographically image any surface with nanometer resolution[91] had even greater impact. Moreover, AFM tips have been modified in

a myriad of ways to make them sensitive to, among many things, magnetic forces, chemical binding forces, and electrostatic forces. Now, a conductive-AFM (C-AFM) has been utilized in order to detect electrical signals from the sample.

As AFM tips are non-metallic, in C-AFM, the tip is typically coated with a thin metallic film to allow it to make height localized measurements of the conductivity of a given substrate, and to correlate these data with measurements of the topography. For example, copper phthalocyanine (CuPc) nano-crystals have been characterized by the C-AFM.[95] Subsequently, the differences between grain and grain boundary have also been investigated. Therefore, by obtaining current images with various channel length, the morphology dependant electrical properties have been revealed. More recently, electrical properties of nano-structured composite materials have been characterized via C-AFM, especially for the applications of energy storage materials and devices.[107-108]

Furthermore, the electrical transport behavior of variable conjugated molecular wires (CMW) on metal substrate under different temperatures was studied by using C-AFM intensively.[109-112] For instance, “click chemistry” is used to synthesize the CMW on Au substrate with length up to 10 nm, varied from 1 to 11 numbers of units (Figure 1.7). It was found that with increasing molecular length, a transition of electrical transport behavior from tunneling to hopping occurs.[109] Around that period of time, different groups also studied the electrical

properties of SAMs of unique group of molecules with C-AFM, such as I-V testing,[113] adhesion force, [114] and correlating results with simulation.[115]

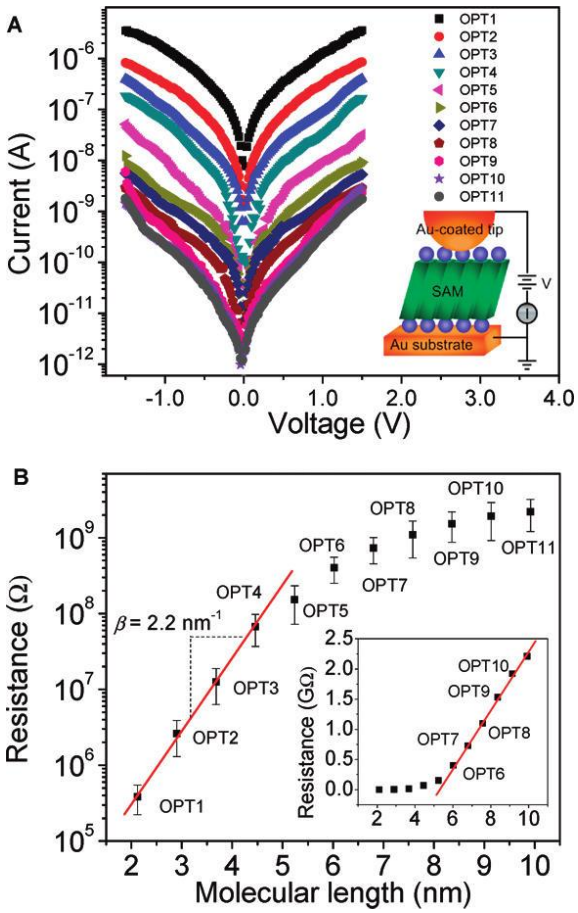

Figure 1.7 C-AFM characterization of OPT molecular wires. (a) Plot of I-V curves in semilog. (b) Plot of R versus L in semilog.[109] Reprinted with permission from reference 100. Copyright 2010 American Chemical Society.

Another advantage of a C-AFM is current mapping, which makes the correlation of morphological-electrical properties even simpler than before.[116] More recently, Samorì *et al* has demonstrated a local AFM tip could induce electrochemical reduction process of graphene oxide (GO), and hence the patterning of reduced GO was realized. The I-V characteristics of before and after

tip induced reduction are shown in Figure 1.8, as well as the evidence of patterning, current mapping at different bias are shown.[117] Riedo's group also used C-AFM with a heated tip to thermally reduced GO to rGO locally.[118]

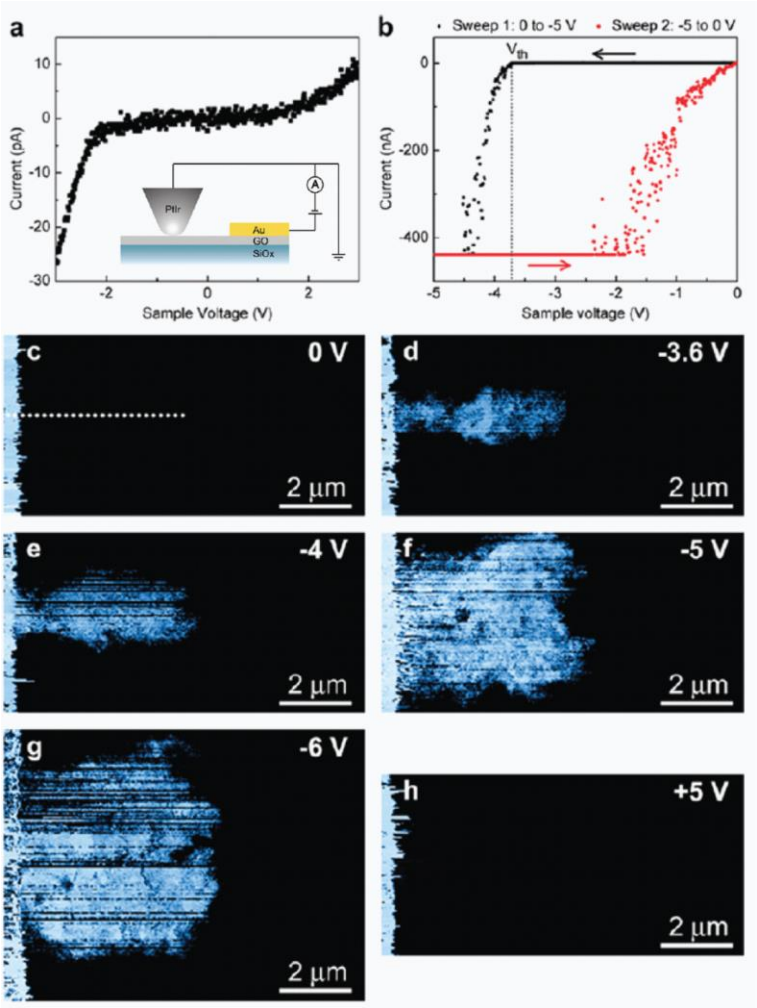

Figure 1.8 (a) I-V characteristics of a few-layer GO film before reduction. (b) The current will only increase until negative bias applied larger than -3.6 V. (c-f) Current mapping under different bias. [117] Reprinted with permission from reference 108. Copyright 2010 American Chemical Society.

Besides electrical properties of supramolecular assemblies, such as SAMs, and GOs being measured and manipulated by C-AFM, it can also measure the single-molecule conductance by establishing a junction among tip, molecule and substrate.[119-120] However, several elaborate assembly steps have to be conducted, and the contact resistance between the conductive probe and Au nanoparticle may induce a Coulomb blockade effect, which makes the measured resistance not only take consideration of the conductance of the single molecule.

1.3 Structural Behavior and Functional Properties of Self-Assemblies

It is important to design and control nano-objects at interfaces in order to push forward the development of nanoscience and nanotechnology.[121] As far as control on the nanometer scale (between 1 and 10 nm) is concerned, molecules are the favorite building blocks to decorate, structure, and functionalize surfaces. Following a bottom-up strategy, the tools of interfacial supramolecular chemistry provide the guidelines on how to design molecular building blocks in order to achieve a balance among molecule, substrate, and solvent leading to the targeted functional patterns.[93]

1.3.1 Host-guest System

Among the two dimensional interfacial supramolecular assemblies, nanoporous networks have attracted much attention, due to their potential to establish a host-guest system, which can be further developed to a variety of molecular electronics. One way for obtaining 2D porous networks is by using macrocycle molecules, which possess porous structures by themselves.[122-124] The other way of forming a 2D nanoporous network is more commonly implemented, that is self-assembly of molecules by intermolecular interactions, such as hydrogen bonding,[125-126] metal-ligand interaction,[27, 127-128] and van der Waals interaction[129-132] at the interface.[93, 127]

One classical molecule to form a 2D honeycomb network is TMA with a three-fold symmetric structure and bearing three carboxylic acid groups.[41-42] It has been demonstrated that a TMA formed porous structure has a pore of 1.1 nm in diameter. The network is very robust even under the disturbances such as scanning motion of an STM tip. The coronene molecule has been selected as a guest molecule to fill inside the pores (Figure 1.9 A). Furthermore, it is a dynamic process, since the coronene molecule could temporarily be vacated from the cavities and later re-occupy the pore again (Figure 1.9 B).[126]

Besides the rigid porous network as a host, it is also possible to use a flexible porous network to accommodate guest molecules, in particular, alkoxylated DBA molecules formed honeycomb network with a nanographene as the guest molecules. Due to the flexibility of this host network, the numbers of

guest molecules are able to be adjusted with modifying the alkyl chain length of DBA, for instance, using the longest alkoxy chains ($OC_{20}H_{41}$), a number of six nanographene molecules could be hosted (Figure 1.10 c-e).[130]

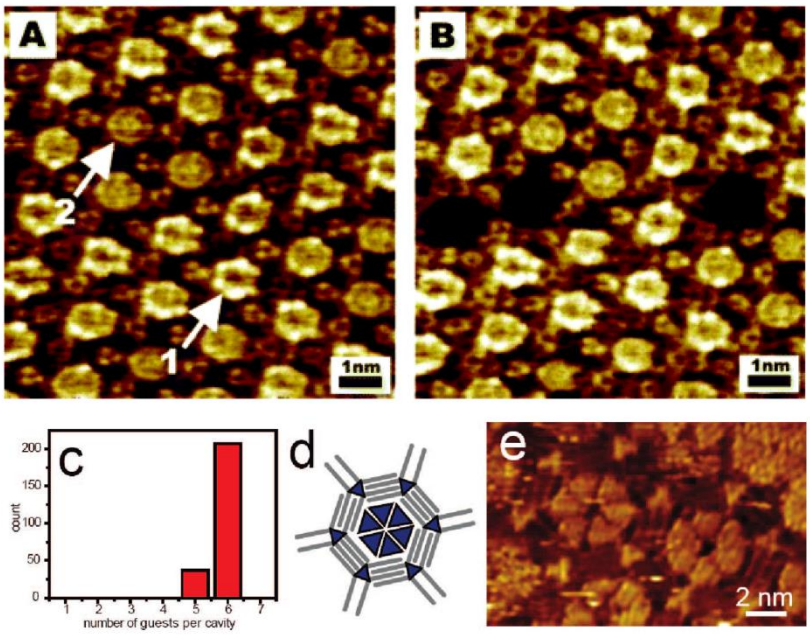

Figure 1.9 (a) STM image reveals the inclusion of coronene molecules in the TMA host structure. (b) A dynamic process is observed with vacancy of coronene molecules in the pores.[126] Copyright 2004 American Chemical Society. (c-e): A host-guest system is formed by DBA-OC_{20} and nanographene molecules.[130] Reprinted with permission from reference 122. Copyright 2008 American Chemical Society.

1.3.2 Disk-like π-conjugated Self-assemblies

It is convenient and straightforward to utilize the method of interfacial molecular self-assembly for establishing complicated architectures and fabricating functional surfaces on the nanoscale.[93, 128, 133-135] One of the important structure is self-assembly of disk-like π-conjugated molecules, because its advantages of promoting electron transfer through the π-π interaction. Moreover, by chemically modulating the functional groups being attached to the backbone of that molecule, the self-assembly behavior could be tuned correspondingly.[22-23, 136-140] For instance, it has been demonstrated that a series of designed hexa-peri-hexabenzocoronene (HBC) self-assemblies could be used as an active component for molecular electronics, like molecular rectifiers and single-molecule chemical field-effect transistors.[22, 24] Therefore, it is critical to rationally design the disk-like molecule with specific self-assembly structures in order to be used for molecular electronics. Moreover, the self-assembled structures have a great influence on the performance of the device using such molecules.[141] Hence, it is fundamentally important to understand the behavior of interfacial self-assembly at surfaces for the purpose of providing useful information for molecular devices.

Due to the mentioned needs in studying the interfacial supramolecular assembly behaviors of HBC molecules, different derivatives with different functional groups has been investigated tremendously.[142-148] STM has been used as a powerful tool to resolve the self-assembly behavior of HBCs at solid-liquid or solid-vapor interface. However, in most of the HBC; assembled in a closely packed hexagonal pattern, different contrast was observed for donor and acceptor parts.

For example, HBC with alkyl chains self-assembled in a hexagonal motif shown in Figure 1.10.[144] This is because of the six fold symmetry of the HBC derivatives. Therefore, one of the challenges is to enrich the architecture based on HBC derivatives with a greater control and manipulation.

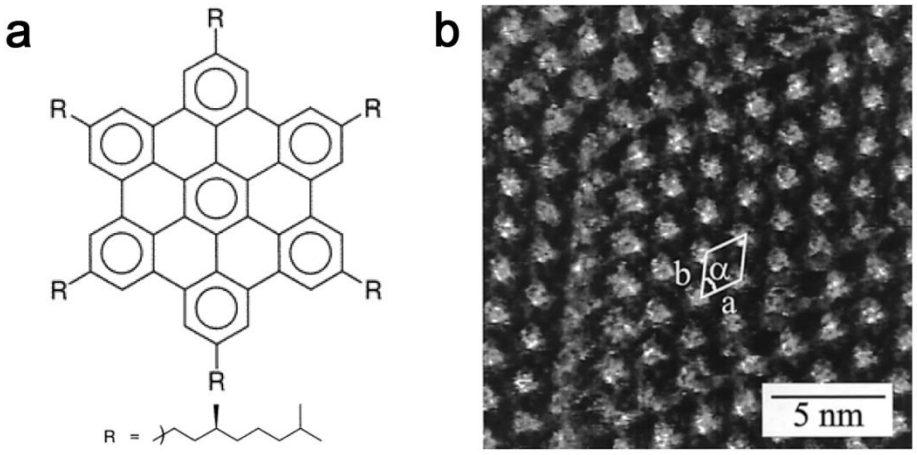

Figure 1.10 Self-assembly behavior of HBC-C_8: (a) chemical formula, (b) STM image of HBC-C_8 at the solid-liquid interface.[144] Reprinted with permission from reference 139. Copyright 2001 American Chemical Society.

1.3.3 Molecular Electronics

Building up an electronic device from individual molecules has become one of the ultimate goals in the field of nanoscience and nanotechnology. In order to achieve that goal, different molecular systems have been intensively studied, especially with the help of scanning probe microscopy. However, the ability to

control molecules with absolute precision and pre-programmed engineering protocols remains one of the challenges for molecular electronics. Therefore, feasible method for well controlled nanoscale organic structures have to be created, and functional properties should also be considered. In this section, we reviewed the development of highly ordered molecular structures formed at solid-liquid interface, which possesses the great potential to be used for establishing molecular electronics.

There were types of molecular systems possible to be implemented in the nanoscale circuit in the future.[149-150] Besides the rectification behavior that has been proved from TTF derivatives, systems with donor and acceptor components have also been designed to reveal the energy transfer process by using STM and scanning tunneling spectroscopy (STS) at the interface.[151-153] For instance, by changing the voltage applied between the tip and sample, brightness of the moieties corresponding to their local density of state varied accordingly (Figure 1.11). Upon applying a negative bias, HOMO level of oligo(p-phenylene vinylene) (OPV-donor, indicated as blue in the band structure at Figure 1.11) is closer to the Fermi level of HOPG, hence it is easier for the current to tunnel from the HOPG to the tip via $HOMO_{OPV}$ level, resulting in brighter contrast of OPV moieties in the STM image. And vice versa for the $LUMO_{PDI}$ level. Therefore, it proved that the electrical properties of the donor and acceptor parts could be revealed by the contrast in bias-dependent STM imaging.[151]

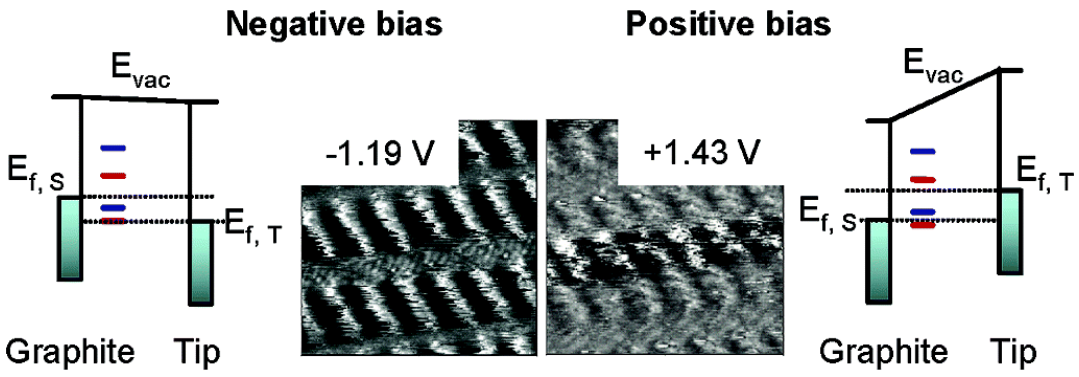

Figure 1.11 The 2D crystal lattice structure and bias-dependent contrast of a D-A-D triad molecule.[151] Reprinted with permission from reference 151. Copyright 2003 American Chemical Society.

1.4 Other Emerging Techniques for the Development of Supramolecular Materials and Devices

It has provided tremendous help for the field of interfacial supramolecular assemblies from the family of scanning probe microscopes, like STM, AFM and C-AFM. Moreover, the development of scanning probe microscopy has constantly accelerated the understanding of fundamental phenomenon across the inter-disciplinary field of chemistry, physics and biology. Particularly, the interfacial phenomenon at molecular or even atomic level has been focused extensively, since the introduction of single molecule force spectroscopy (SMFS) and STM break junction technique (STM-BJ) in the late 1990 and early 2000 respectively.

1.4.1 Single Molecule Force Spectroscopy

It has been a dream comes true for scientists to investigate individual molecules and quantitatively reveal the mechanical force involved along the dynamic process. Especially, biological molecules have been intensively studied, such as DNA or proteins with a length of several thousand nanometers. A number of techniques have been developed in a parallel fashion, and one of them is a derivative from the family of scanning probe microscopes, that is single molecule force spectroscopy (SMFS).

SMFS has been extensively utilized in the field of biology; it has been used mainly for understanding the folding and unfolding of biological species, like unfolding of subunits of titin muscular proteins,[154] polysaccharides,[155-156] study of the interaction for antibiotics,[157] and the mechanical behavior of yeast membrane[158] and so on.[159-162]

What more we could explore by using this SMFS technique is to discover the molecular behavior at different interfaces. For instance, it has been demonstrated that the bond-rupture forces between tip and surfaces covered with hydroxyl- and thiol-terminated silane groups could be measured by obtaining the adhesion force at force distance curves.[163] Furthermore, with using dynamic force microscope (DMF) oscillation amplitude along with conventional force curves, the stiffness data could be obtained along with force values, which allows it to gain the

knowledge whether an elastic behavior dominates the pulling region or not. This makes SMFS possible to study more complex behavior, such as modulus of the molecules and so on.[164] More recently, researchers have used SMFS in an aqueous condition, for example single polyethyleneimine molecules have been imaged in terms of topography, adhesion and contact stiffness by using a pulsed-force mode of the SFM.[165] It was found that the molecule-substrate interaction between a pyrene molecule and graphite is about 55 pN and single molecular rupture events were witnessed, therefore it demonstrates the possibility of employing SMFS techniques to investigate π-π interactions in the future.[166]

The system of supramolecular assemblies has been intensively studied via SMFS technique,[164, 166-173] and SMFS has even been combined with a C-AFM to reveal the effect of N-Au bond rupture on the molecular backbone. The detailed design of experiments is shown in Figure 1.12, a schematic drawing of the modified C-AFM with SMFS is presented, and one of the typical curves of conductance and force versus distance respectively is shown in B, with the red curve indicating conductance and blue force. From the characteristic curves, one can see that the conductance is decreased with increasing distance in a stepwise manner. Meanwhile, the required force exhibits a sawtooth pattern revealing elastic and plastic deformation at the junction. Overall, it proves that 1,4-benzenediamine has the weakest bond with Au substrate, and the pyridine-Au interaction shows the strongest force among the four molecules that have been measured.

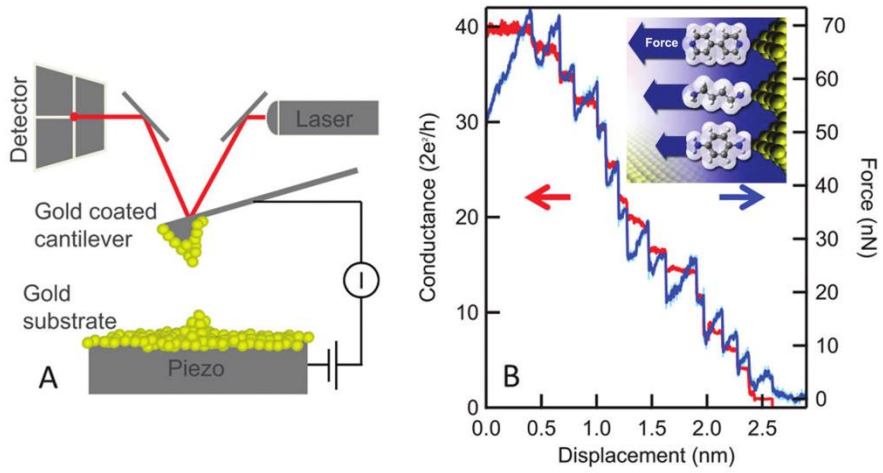

Figure 1.12 (a) Schematic drawing of combined C-AFM with SMFS technique. (B) A typical set of curves during junction break, conductance (red) and force (blue) with respect to tip substrate distance.[174] Reprinted with permission from reference 174. Copyright 2011 American Chemical Society.

In summary, this force spectroscopic tool, SMFS allows us to understand molecular structures and functions with precise control, which will constantly push forward the development of supramolecular assemblies, molecular electronics, and even biology in the future.

1.4.2 STM Break Junction

To discuss the prospects of SPM for molecular imaging, it is important to also take a look at the spectroscopic techniques and STM modes that assess different measurement signals. Various modes of scanning tunneling spectroscopy

(STS) have already proved their value in revealing interesting properties of molecules on the submolecular scale. For example, by using inelastic electron tunneling spectroscopy (ITES), the excitation of vibrational modes with submolecular resolution is realized.[175-177]

Substantial advances have been made towards the goal of measuring, controlling and understanding electron transport through single molecules covalently bonded to electrodes.[178] One of the earliest groups (N. J. Tao's) demonstrated the measurement of single-molecule conductance at ambient condition by using the STM break junction technique shown below. In Figure 1.13, a gold contact between tip and substrate was first formed, and then the contact was broken step by step while pulling away the tip from the substrate. 1000 such curves in Figure 1.13 (a) are used to generate a conductance histogram shown in (b) with peaks at multiple numbers of G_0 (= $2e^2/h$). Then molecules migrated to the gap between Au tip and substrate, and formed another set of conductance steps in (c) and generated the histogram in (d). The peaks revealed numbers of molecules in between the junction. A control experiment without molecules was also done, and no steps or peaks were observed.[179] Hence, it proves that single-molecular junction is detected and measured by such break junction technique, and the statistical analysis makes the result even more convincing.

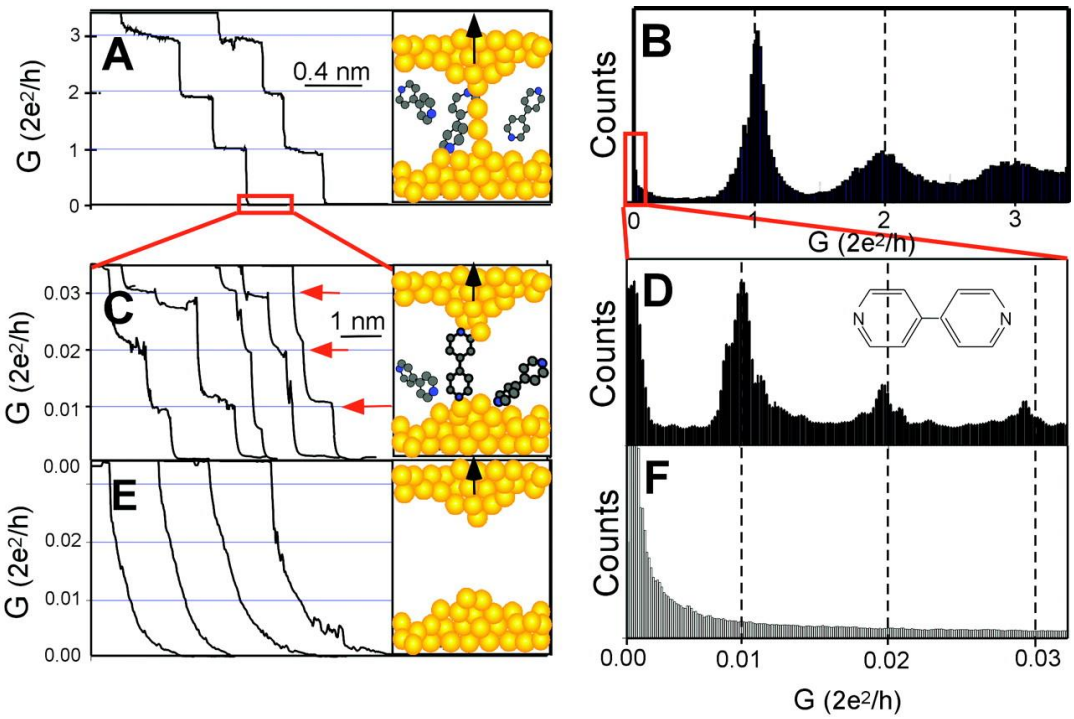

Figure 1.13 Single-molecule conductance measurement at ambient condition by using STM break junction technique: (a,b) Break junction formed between Au tip and substrate, typical conductance curve and corresponding histogram. (c,d) Molecule migrated from the solution to the Au break junction. (e and f) Control experiment without molecules in the solution.[179] Reprinted with permission from reference 179. Copyright 2003 American Association for the Advancement of Science.

More recently, another group proposed a modified method according to STM break junction, which is called "gentle touch" method. In this method, the Au tip and substrate is not forming molecular wire first, but the Au tip is rather directly in contact with molecule, and hence establish a molecular junction between tip and

substrate by carefully control the feedback loop of the system.[180] Despite different measurement of single alkanedithiol molecule conductance,[181-182] the tunneling background is an issue during statistical analysis, since it represents electron tunneling via space but not conduction through a molecular junction.

In order to solve the background problem, Tao's group demonstrated by combining the AC and DC components of the current, it could determine whether the molecule is at the junction. Hence, they could remove the tunneling background from the histogram and measure the I-V characteristics more accurately.[183] STM break junction is a great technique, which enables the measurement of single-molecule conductance, but the utilization of such technique in the field of molecular electronics is beyond that.[184-193]

1.5 Research Motivation and Objectives

The structures and functional properties of supramolecular assemblies at different interfaces have been presented in the previous sections. With the challenges of controlling matter at the molecular level with specific molecular functional systems in the field of nanoscience,[53] as well as the ultimate goal toward integration of single molecule electronics has been presented. However, this study is still in its infant stage where more fundamental scientific studies are required. Hence, an in-depth study on both structural behavior and functional properties of interfacial supramolecular assemblies are required in my PhD study.

First, in order to investigate the effect of intermolecular interactions in controlling the supramolecular assembly at the solid-liquid interface, a new class of C_3-symmetric HBCs with alternating substituents is studied by using STM.

Second, with the aim of establishing a host-guest system, coronene molecules are filled inside the hydrogen bond assisted honeycomb network, which could be used as molecular rectifiers in the future.

Third, in order to explore large π-conjugated system with functionalization ability, chemical modulated graphene is studied at solid-vapor interface and photoreponse is demonstrated.

At last, with the intention of exploring the structural and functional properties of three dimensional aggregates, a class of π-conjugation interrupted dendrimers is investigated, and tunable electrical properties are obtained.

1.6 Organization of the Thesis

This thesis is divided into six chapters. Chapter 1 provides a solid introduction into the field of supramolecular assemblies, starting with the fundamental concept of supramolecular chemistry and then addressing on the tools that help in understanding this fundamental phenomenon at the molecular level. Subsequently, self-assembly behavior at the solid-liquid interface and potential applications like molecular electronics were presented, with the state-of-art of development in both structural and functional properties at the interface, and finally addresses the challenges undertaken in the correlation and combination of

the two fields. Chapter 2 presents how to form 2D honeycomb network via specific intermolecular interactions at the solid-liquid interface. Chapter 3 demonstrates an example of host-guest system, by utilizing the hydrogen bond assisted nanoporous network with matched sizable molecules. Chapter 4 reveals photoresponse behavior of chemically modulated graphene via photocurrent mapping at nanoscale. Chapter 5 investigates a series of 3D aggregates, which reveals tunable electrical properties with decorating small molecules. Finally, the thesis closes with conclusions and future perspectives for this project as addressed in Chapter 6.

Chapter 2 2D HONEYCOMB NETWORK VIA SPECIFIC INTERMOLECULAR INTERACTIONS

In this chapter, 2D honeycomb networks are obtained at solid-liquid interface via specific intermolecular interactions, namely, hydrogen bonding and dipole-dipole interaction. Through rational molecular design, we report on how the specific intermolecular interactions can play a critical role in controlling the interfacial supramolecular assembly of a new class of C_3-symmetric hexa-*peri*-hexabenzocoronene (HBCs) with alternating substituents on a HOPG surface. The alternating substituents drive the specific intermolecular interactions, such as carboxylic acid group (-COOH), fluorinated methylene ($–CF_3$), cyano (–CN), nitro ($–NO_2$), and chloro (-Cl). STM is used to observe and investigate the formation of supramolecular architectures at the solid-liquid interface.

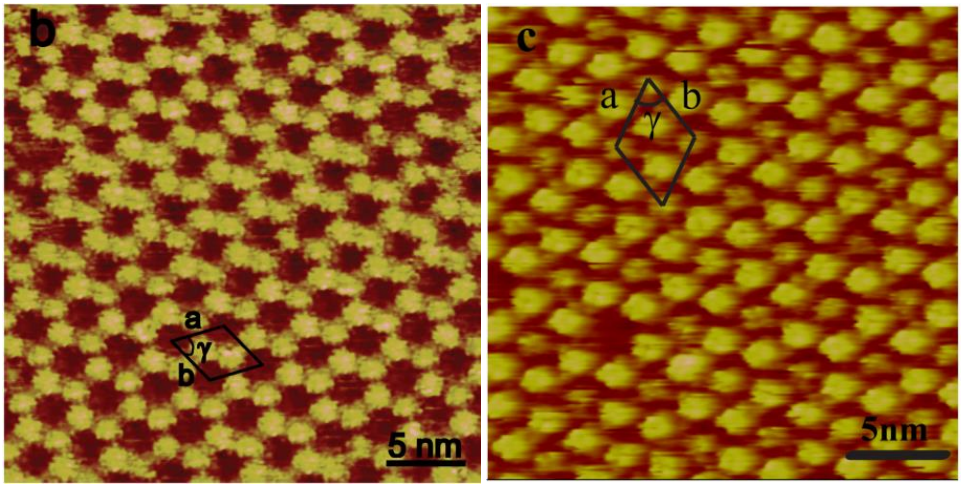

2.1 Introduction

Interfacial molecular self-assembly has attracted considerable attention because it is an important way to create ordered nanoscale structures and fabricate functional surfaces.[121, 194-197] Of particular interest are disc-like π-conjugated molecules, providing tailored electronic properties of their flat conjugated systems which can be varied dramatically through synthetic modification of their sizes and topologies.[22-23] For example, hexa-*peri*-hexabenzocoronene (HBC) can self-assemble into highly ordered monolayer on the substrate surface and work as an active component for molecular electronics, such as molecular rectifiers and single-molecule chemical field-effect transistors.[22, 24-25] In this case, the ability to control the interfacial supramolecular architectures formed by disc-like molecules is important to promote the development of such molecules in molecular device application. In addition, the spatial arrangement of the disc-like molecules plays a critical role to determine the device performance of such molecules.[141] Therefore, the study of interfacial self-assembly of molecules on a flat solid substrate will give more information on the molecular interactions and their spatial packing.

Over the past decade, the interfacial supramolecular assembly of a variety of HBC derivatives with different substituents and peripheral decorations has been widely investigated.[142-148] Among those intensive studies involving the self-assembly of HBC derivatives on substrate surface by scanning tunneling microscopy (STM), one thing in common is that most of them formed closely

packed hexagonal motif, despite multiple contrast have been found for some HBC derivatives due to the donor or acceptor properties. For instance, HBC with alkyl chains attached to the aromatic core via a phenylene spacer results in a molecular lattice with a hexagonal superstructure,[144] which is mostly due to the six fold symmetry of the HBC derivatives. So far, there is a challenge towards enriching the architecture based on HBC derivatives with a greater control and manipulation. In general, the self-organization of molecules on surfaces is entropically driven and governed by several parameters such as intermolecular interactions as well as molecule-substrate interactions.[198-199] Obviously, the introduction of different substituents onto the HBC core may modulate the intermolecular interactions and therefore help to expand the interfacial supramolecular structures for HBCs. However, the use of the specific intermolecular interactions (e.g. dipole-dipole interactions and hydrogen bonds) between the HBC molecules for interfacial supramolecular assembly have not been sufficiently addressed.[146]

In this context, we report how the intermolecular dipole-dipole interactions can play a critical role in controlling the interfacial supramolecular assembly of a new class of C_3-symmetric HBCs with alternating substituents on HOPG surface, where STM is used to directly observe and investigate the formation of supramolecular architectures at solid-liquid interface. For HBC-COOH, the carboxylic acid groups attached onto the HBC core can induce hydrogen bonding as the intermolecular interactions. For HBC-CF_3, HBC-CN and HBC-NO_2, the fluorinated methylene (–CF_3), cyano (–CN), and nitro (–NO_2) functional groups

attached onto the HBC core through phenylene vinyl spacer serve as strong electron withdrawing groups. In this case, the unbalanced electron distribution in HBC cores results in a three-fold symmetric dipole moment for these three molecules. We expect that through this molecular design, the intermolecular hydrogen bonding as well as dipole-dipole interactions might drive the molecular assembly and enable fine control over the supramolecular architectures at the solid-liquid interface. For comparison, HBC-Cl which does not have specific intermolecular interactions was also designed and synthesized.

2.2 Experimental Section

2.2.1 STM Imaging

Prior to imaging, compounds under study were dissolved in 1-phenyloctane (Aldrich, 99%), and a drop of this solution was applied to a freshly cleaved surface of highly oriented pyrolytic graphite (HOPG). STM experiments were performed using a scanning probe microscope (Veeco Multimode SPM system with a NanoScope V control station) in constant current mode under ambient conditions. STM tips were prepared by mechanically cutting a 0.25 mm thick Pt/Ir (80/20) wire. All STM images contain raw data and are not subjected to any manipulation or image processing.

2.2.2 Synthesis of Hexa-*peri*-hexabenzocoronenes Derivatives

The Synthesis of the HBC derivatives was not the key part that we want to address in this thesis; therefore only one synthetic route of the HBC derivatives will be explained in details in this section. The HBC-COOH was successfully synthesized according to Scheme 2.1. The asymmetrically substituted 3',4',5'-tris(butan-1-yloxy)-4-methyl ethynylbenzoate 1, in which one ester group and three alkoxy groups were introduced, was first synthesized according to similar procedures reported in literature.[200-202] Cyclotrimerization of 1 in the presence of catalytic amount of $Co_2(CO)_8$ provided two HPB isomers 2 and 3, in 25% and 50% yield, respectively. The relatively large polarity of the ester group makes the separation of the two isomers by column chromatography feasible due to sufficient polarity difference. The key step is the oxidative cyclodehydrogenation of the HPB precursor 2. Precursor 2 was treated with $FeCl_3$ in nitromethane and dichloromethane (DCM) and the desired D_{3h}-symmetric HBC compound 4 was obtained in a relatively low yield (30%) due to a slow reaction rate and formation of complicated by-products. This synthetic difficulty can be explained by the deactivation effect of the electron-withdrawing ester group and ether cleavage during the oxidative cyclodehydrogenation process. Nevertheless, the target compound 4 still can be obtained because three 1,2,3-tributoxyphenyl groups are introduced into the HPB precursor 2 and the electron rich character of these three phenyl rings can compensate for the electron deficient character of the other three phenyl rings substituted by electron-withdrawing ester groups. HBC-COOH was then prepared by hydrolysis of 4 in aqueous potassium hydroxide followed by

acidification with 2M HCl acid. The pure product was obtained in a 63% yield after further purification by precipitation in mixed solvents (hexane/tetrahydrofuran = 10/1 (v/v)) and washing with chloroform and methanol. The attachment of tributoxy chains in the HBC-COOH molecule also makes it soluble in THF and partially soluble in DMSO, but insoluble in other normal organic solvents such as chloroform.

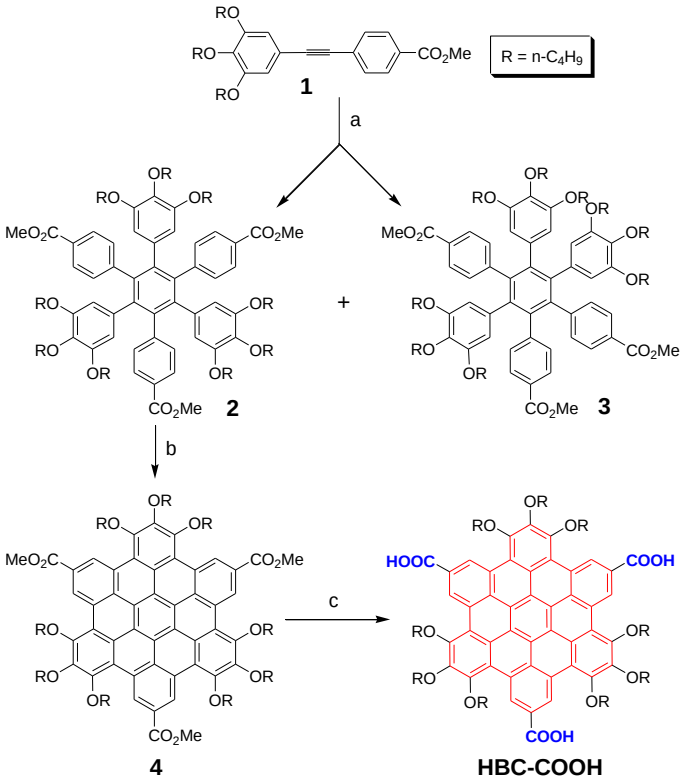

Scheme 2.1 Synthetic route of HBC derivatives, HBC-COOH for example. Conditions: (a) $Co_2(CO)_8$, dioxane, reflux, 24h (2, 25% yield; 3, 50% yield); (b) $FeCl_3$, CH_3NO_2, DCM, 30%; (c) i) 3 M KOH, reflux, 12h; ii) 2 M HCl, 63%.

2.2.3 Molecular Mechanics and Dynamics Simulation

The formation of interfacial supramolecular structures was investigated by a classical molecular mechanics method with the full ab-initio COMPASS[203] force field integrated in the Materials Studio package. The Forcite module was used for performing molecular mechanics and dynamics simulations. The COMPASS force field has a functional form as follows:

$$E_{total} = \sum_b [k_2(b - b_o)^2 + k_3(b - b_o)^3 + k_4(b - b_o)^4] + \sum_\theta [k_2(\theta - \theta_o)^2 + k_3(\theta - \theta_o)^3 + k_4(\theta - \theta_o)^4] + \sum_\phi [k_1(1 - cos\phi) + k_2(1 - cos2\phi) + k_3(1 - cos3\phi)] + \sum_\chi k_2\chi^2 + \sum_{b,b'} k(b - b_o)(b' - b_o') + \sum_{b,\theta} k(b - b_o)(\theta - \theta_o) + \sum_{b,\phi}(b - b_o)[k_1 cos\phi + k_2 cos2\phi + k_3 cos3\phi + \sum_{\theta,\phi}(\theta - \theta_o)[k_1 cos\phi + k_2 cos2\phi + k_3 cos3\phi] + \sum_{b,\theta} k(\theta' - \theta_o')(\theta - \theta_o) + \sum_{\theta,\theta,\phi} k(\theta - \theta_o)(\theta' - \theta_o') cos\phi + \sum_{i,j} \frac{q_i q_j}{r_{ij}} + \sum_{i,j} \epsilon_{ij} [2(\frac{r_{ij}^o}{r_{ij}})^9 - 3(\frac{r_{ij}^o}{r_{ij}})^6] \quad (1)$$

where both diagonal and off-diagonal cross-coupling terms were used to describe valence interactions. Furthermore, a LJ-9-6 function has been applied to describe the non-bond interactions. A 6th order combination law has been used for those unlike atom pairs. The COMPASS force-field covers broad variety of covalent molecules including most common organics, small inorganic molecules, and polymers. Therefore the force-field has been chosen aiming for best reproduction of experimental results.

To approach global minimum of supramolecular structure as much as possible, molecular dynamics and simulated annealing were performed to each structure. For each structure, the simulated annealing dynamical evolution was performed with canonical ensemble (NVT) over the temperature range of 300-500 K, where a total of 10 heating cycles were applied during the 100 ps duration of each trajectory. The time step was chosen as 1 fs throughout the structures.

Geometry optimization was carried out for each dynamical run of a specific structure with the following requirements: energy difference < 2.0×10^{-5} kcal/mol, force difference < 0.001 kcal/mol/Å, and displacement difference < 1.0×10^{-5} Å. A cutoff distance of 18.5 Å was applied for both electrostatic and van der Waals energies. The unit cells of the 2D nanostructures were determined by the following method: for the STM -observed hexagonal structures (i.e., HBC-Cl, HBC-B-NO_2 and HBC-CN), the size of the initial supercell for the HOPG with three layers of graphene was determined by the measurements made on the STM images. The lattice parameters of the supercell were integer multiples of the graphite (0001) surface unit cell with lattice parameter a = b = 2.46 Å. In addition, a vacuum layer of 80 Å was included for both graphite (0001) surface and supercell to avoid the neighboring interaction in the c direction. The initial unit cell for each adsorbate was chosen in such a way that a and b were close to the experimental measurements. Supercells with ± 1 or 2 graphite (0001) surface unit cells were also constructed to compare with the initial choice. After comparing the interaction energy including adsorbate-adsorbate and adsorbate-substrate

determined by $E_{int} = (E_{unit\text{-}cell} - E_{substrate} - N \times E_{adsorbate})/N$, where N is the number of adsorbate molecules in the supercell, the proposed most energy preferable configuration could be determined. Here the $E_{adsorbate}$ term is the energy for the free-standing adsorbate molecule with optimized structure using the methods listed above.

The results of interaction energies of different configurations as well as functional groups are listed in Table 2.1. For HBC-CF_3 and HBC-COOH, there are 2 molecules per supercell, and for the other structures, there are four molecules per supercell. In Table 2.1, the parameters of the supercell as well as the corresponding interaction energies for each HBC derivatives are listed. The structures with the lowest interaction energy (indicating the most stable structure) are selected to be the simulated model for each HBC derivatives in this section.

Table 2.1 Interaction Energies for Various Configurations of HBC Derivatives Adsorbed on HOPG.[204] Reprinted with permission from reference 205. Copyright 2011 American Chemical Society.

HBC-COOH	
Supercell Size	E_{int} (kcal/mol)
13×13	-161.42
12×12	-153.06
14×14	-150.18

15×15		-149.31	
11×11		-124.6	
HBC-NO_2		**HBC-CN**	
Superce ll Size	E_{int} (kcal/mol)	Superce ll Size	E_{int} (kcal/mol)
19×19	-178.66	20×20	-186.44
21×20	-173.46	19×19	-185.82
18×18	-172.31	22×22	-184.39
20×20	-171.11	21×21	-182.95
17×17	-160.33	18×18	-173.67
HBC-Cl		**HBC-CF_3**	
Superce ll Size	E_{int} (kcal/mol)	Superce ll Size	E_{int} (kcal/mol)
17×17	-138.18	17×17	-162.45
16×16	-137.70	15×15	-161.27
18×18	-136.82	18×18	-160.44
15×15	-130.84	19×19	-159.35
19×19	-130.45	16×16	-158.15

2.3 Results and Discussion

2.3.1 Hydrogen Bond Assisted 2D Honeycomb Network

2.3.1.1 Rational Design of Molecular Structure

To explore the opportunities of fabricating a surface with new functionalities such as electronic conduction or charge transfer, we are interested in introducing electronic active components into the 2D network. Polycyclic aromatic hydrocarbons (PAHs)[23] are good candidates for this purpose because they are π-conjugated systems and usually exhibit interesting optical and electronic properties. Actually, many disc-like PAHs such as hexa-*peri*-hexabenzocoronene (HBC) can form ordered 2D structures at solid-liquid interface because of strong π-π interactions and van der Waals interactions between the molecules and the highly oriented pyrolytic graphite (HOPG) substrate.[129, 143, 205-208]

The structure of HBC-COOH mimics the simplest analog TMA molecule, as shown in Chart 2.1, with the benzene ring in TMA[93] replaced by a "superbenzene" core (HBC). Thus, one can expect formation of a porous 2D honeycomb network by a combination of π-π interactions, van der Waals interactions and hydrogen bonding interactions. The porous structure also allows us to do further modifications, such as putting guest molecules into the empty cavities.

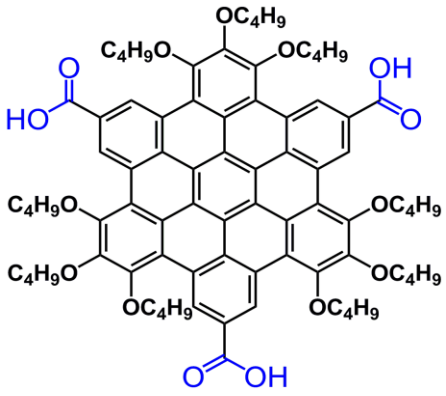

Chart 2.1 Chemical structure of C_3-symmetric hexa-*peri*-hexabenzocoronene

tricarboxylic acid.

2.3.1.2 HBC-COOH Forming 2D Honeycomb Network

The self-assembly of HBC-COOH was studied by STM techniques by dropping the solution of HBC-COOH in the 1-phenyloctane onto a freshly exfoliated HOPG substrate followed by measurements at solid-liquid interface. The results of a fully saturated solution of HBC-COOH are shown in Figure 2.1; a large-area ordered 2D porous network was clearly observed at the solid-liquid interface. Even in a large scanning area of 195.3 ×195.3 nm^2, molecules covered nearly the whole surface and only few defects could be found (Figure 2.1a). This

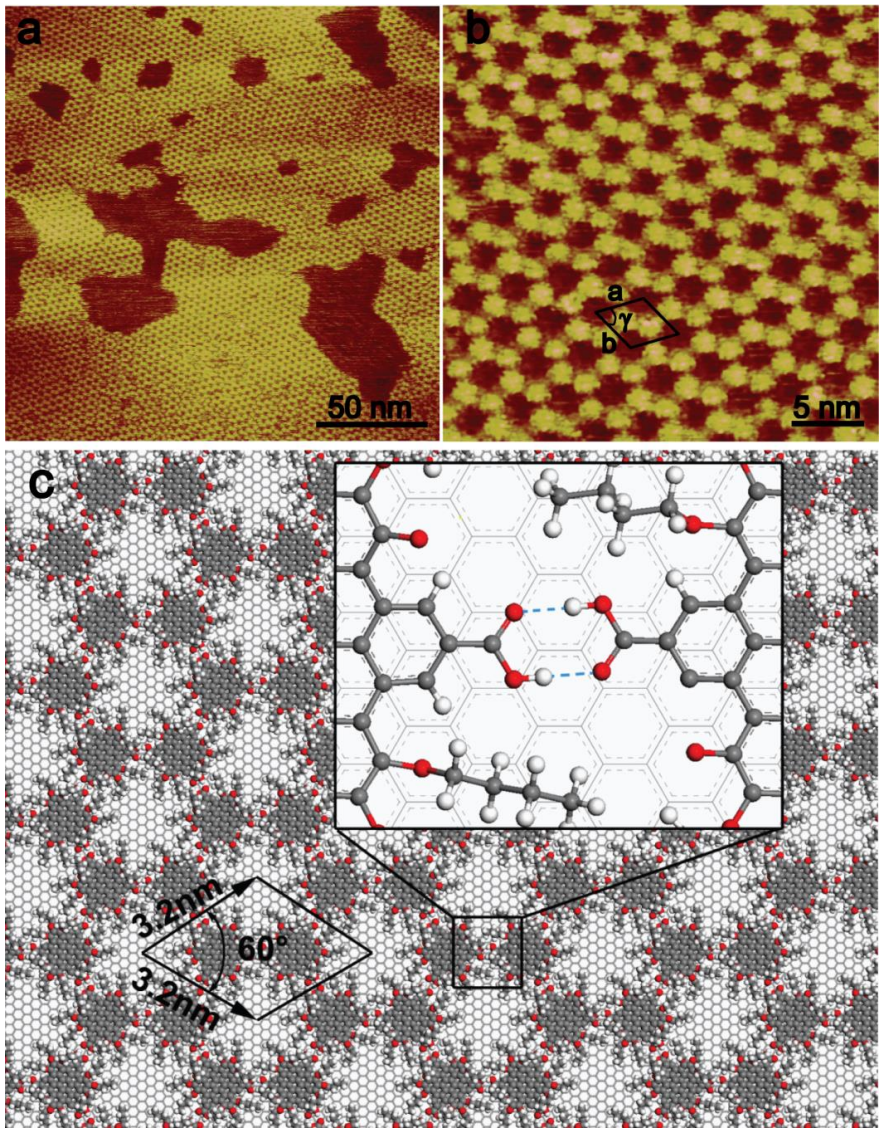

Figure 2.1 STM images and simulated patterns of the HBC-COOH adlayer deposited from 1-phenyloctane solution onto the basal plane of HOPG: (a) large-scale STM image of HBC-COOH (195.3 × 195.3 nm^2, I_{set} = 0.16 nA, and V_{bias} = -0.8 V); (b) high-resolution STM image of HBC-COOH (30.0 × 30.0 nm^2, unit cell: a = b = 3.1 ± 0.1 nm, γ = 60 ± 1°. I_{set} = 0.16 nA, and V_{bias} = -0.8 V); and (c) the simulated self-assembly pattern of HBC-COOH on graphite (0001) surface with the simulated unit cell of a = b = 3.2 nm, and γ = 60°.

indicates that there are strong intermolecular interactions among the HBC-COOH molecules and also between the molecules and the HOPG substrate. High resolution STM images showed a submolecular level pattern of these HBC molecules on the interface (Figure 2.1b). Due to the semiconducting character of the HBC molecules, each of the bright spots in the STM images can be assigned to one HBC core due to its higher tunneling current,[209] and the spot size is also in agreement with the molecular size of the HBC core. The dark area (cavity) could be filled by either the aliphatic chains on the HBC core or solvent molecules, which cannot be identified due to the limited resolution and high flexibility of alkyl chains.

Therefore, it is very clear that the three-fold symmetric HBC molecules self-assemble into a 2D honeycomb network by linking six separate bright discs in a hexagonal pattern *via* hydrogen bonding. It is worth noting that a flower pattern arising from a hybrid combination of dimeric and trimeric associations was also observed for some TMA molecules,[210-212] however, for our HBC-COOH molecule, only a rigid 2D honeycomb network was observed, presumably due to the stronger interactions between the HBC molecules with the HOPG substrate. A hexagonal unit cell can be determined for the 2D honeycomb pattern (Figure 2.1b) with parameters $a = b = 3.1 \pm 0.1$ nm and $\gamma = 60 \pm 1°$, which are in agreement with the calculated parameters ($a = b = 3.2$ nm, $\gamma = 60°$) of a unit cell of HBC-COOH molecules, as indicated in Figure 2.1c.

In the simulated results, it is clearly seen that the superstructure consists of a hexagon with one HBC-COOH molecule at each corner, and that all three carboxylic groups in each molecule form hydrogen bonds with neighboring molecules *via* a typical dimeric hydrogen bonding mode. The strong hydrogen bonding interactions between the molecules and π-π interactions between the molecules and HOPG surface eventually lead to a rigid 2D honeycomb network similar to that of the TMA molecules.

2.3.2 Effect of Concentration on HBC-COOH Nanoporous Structures

Furthermore, the effect of concentration with respect to HBC-COOH self-assembly behaviors is tested by using 0.5, 0.2, and 0.1 times of saturated solution. From Figure 2.2, it can be proved that no structural change occurs even after the saturated solution has been diluted for 10 times both with respect to large scale and high resolution STM images. The size of the domain at all condition is homogeneous and large, indicating a strong π-π interaction between the molecule and HOPG substrate, as well as strong intermolecular interactions among molecules. In addition, the size of the unit cell at all conditions has the consistent values. This further proves that this 2D porous network is stable and rigid, which creates the opportunities to establish a host-guest system in the next step. This is the first HBC derivatives that has shown the ability to establish a 2D rigid porous

network, which has great potential to establish a host-guest system in order to enrich the diversity of molecular electronics.

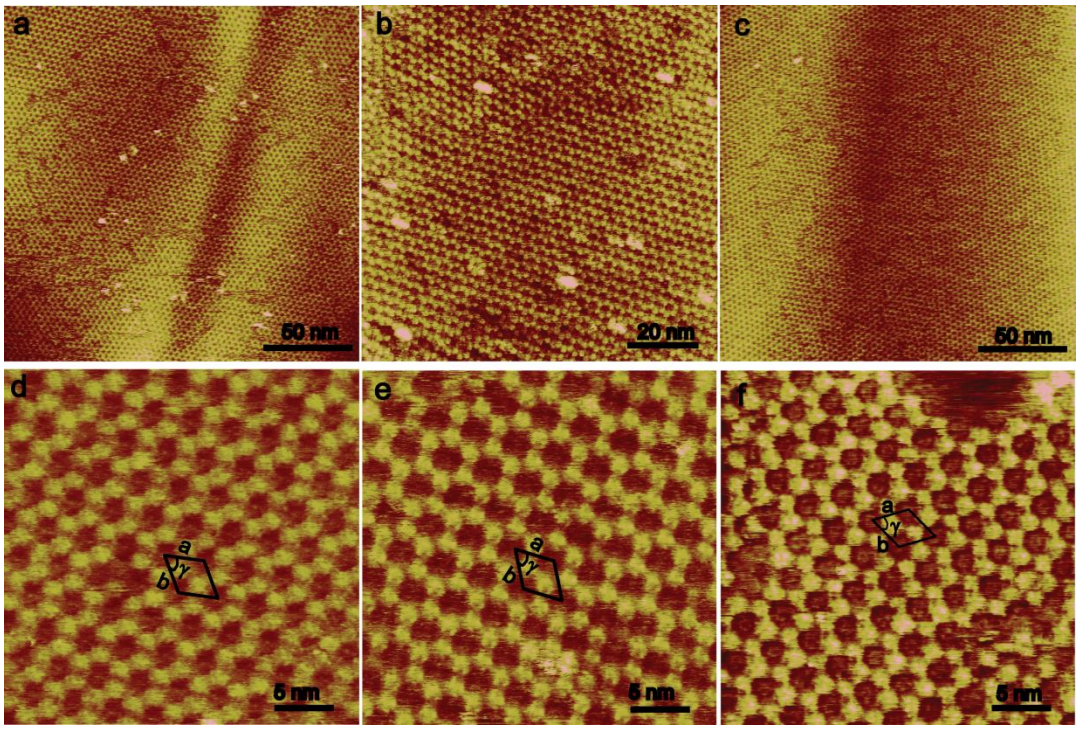

Figure 2.2 STM images of the HBC-COOH adlayer deposited from different concentration of 1-phenyloctane solution onto the basal plane of HOPG: (a) large-scale STM image from 0.5 saturated solution of HBC-COOH (200 × 200 nm^2, I_{set} = 0.165 nA, and V_{bias} = -0.8 V); (b) large-scale STM image from 0.2 saturated solution of HBC-COOH (100 × 100 nm^2, I_{set} = 0.17 nA, and V_{bias} = -1.4V); (c) large-scale STM image from 0.1 saturated solution of HBC-COOH (200 × 200 nm^2, I_{set} = 0.165 nA, and V_{bias} = -0.8V); (d) high-resolution STM image from 0.5 saturated solution of HBC-COOH (30.0 × 30.0 nm^2, unit cell: a = 3.1 ± 0.1 nm, b = 3.2 ± 0.1 nm, γ = 60 ± 1°. I_{set} = 0.165 nA, and V_{bias} = -0.8

V); (e) high-resolution STM image from 0.2 saturated solution of HBC-COOH (30.0 × 30.0 nm^2, unit cell: a = 3.1 ± 0.1 nm, b = 3.2 ± 0.1 nm, γ = 60 ± 1°. I_{set} = 0.17 nA, and V_{bias} = -1.4V); and (f) high-resolution STM image from 0.1 saturated solution of HBC-COOH (30.0 × 30.0 nm^2, unit cell: a = b = 3.2 ± 0.1 nm, γ = 60 ± 1°. I_{set} = 0.165 nA, and V_{bias} = -1.2V).

2.3.3 Antiparallel Dipole-dipole Interactions

2.3.3.1 Rational Design of Molecular Structures

It has been shown that hydrogen bonding is a good way to establish a 2D honeycomb structure at solid-liquid interface for HBC derivatives. This makes us wonder if there are other type of intermolecular interactions that could help in building up the nanoporous network as well. According to the literature, the strength of several noncovalent forces is listed in Table 2.2. The strength of dipole-dipole interactions is comparable with the hydrogen bonding interaction, which makes us want to investigate whether the intermolecular dipole-dipole interactions can play a critical role in controlling the interfacial supramolecular assembly of a new class of C_3-symmetric HBCs with alternating substituents (Chart 2.2) on HOPG surface.

Table 2.2 Strength of Several Noncovalent Forces.[213] Reprinted with permission from reference 214. Copyright 2005 American Chemical Society.

Strength of Several Noncovalent Forces

type of interaction or bonding	strength (kJ mol^{-1})
covalent bond	100−400
Coulomb	250
hydrogen bond	10−65
ion−dipole	50−200
dipole−dipole	5−50
cation−π	5−80
$\pi-\pi$	0−50
van der Waals forces	<5
hydrophobic effects	difficult to assess
metal−ligand	0−400

STM is used to directly observe and investigate the formation of supramolecular architectures at solid-liquid interface. For HBC-CF_3, HBC-CN and HBC-NO_2, the fluorinated methylene (–CF_3), cyano (–CN), and nitro (–NO_2) functional groups attached onto the HBC core through phenylene vinyl spacer serve as strong electron withdrawing groups. In this case, the unbalanced electron distribution in HBC cores results in a three-fold symmetric dipole moment for these three molecules. We expect that through this molecular design, the intermolecular dipole-dipole interactions might drive the molecular assembly and enable fine control over the supramolecular architectures at the solid-liquid interface. For comparison, HBC-Cl which does not have specific intermolecular interactions was also designed and synthesized.

Chart 2.2 Chemical Structures of C_3-symmetric HBC Derivatives.[204] Reprinted with permission from reference 205. Copyright 2011 American Chemical Society.

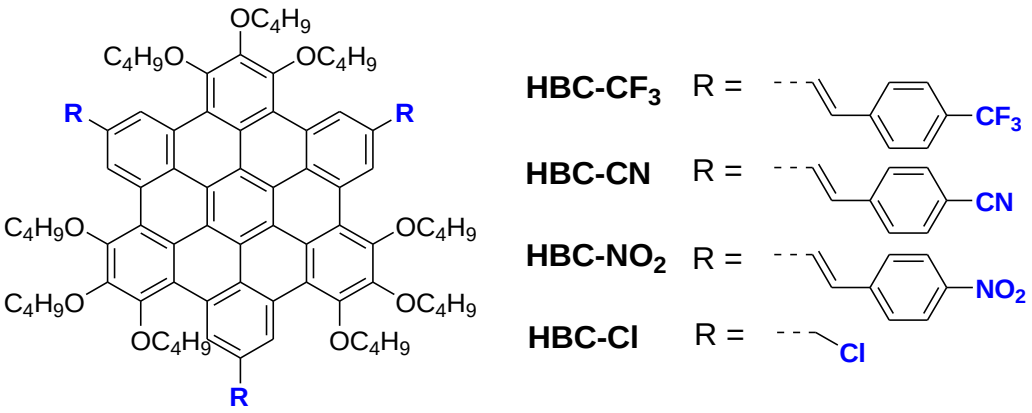

2.3.3.2 HBC-CF_3 Forming 2D Honeycomb Network via Antiparallel Dipole-dipole Intermolecular Interactions

First, we studied the interfacial supramolecular assemblies of C_3-symmetric HBC-CF_3 on the HOPG surface. In addition to $–CF_3$ being a strong electron-withdrawing group, molecules bearing one or more $–CF_3$ groups have shown unique packing properties when compared to those molecules without $–CF_3$.[214] For these reasons, we synthesized HBC-CF_3 to determine how the introduction of $–CF_3$ groups to the core of HBC can influence the supramolecular organization of HBC-CF_3 at the solid-liquid interface. Experimentally, we found that HBC-CF_3 formed a 2D porous network structure in a homogeneous and ordered large area, as

indicated in Figure 2.3. The monolayer of HBC-CF_3 is stable over the whole period of the experiment, which suggests that strong intermolecular interactions among molecules as well as the interactions (mostly π-π interaction) between molecules and HOPG basal plane do exist. Moreover, even with this large-scale image, the honeycomb-like structure on HOPG surface is clearly observable.

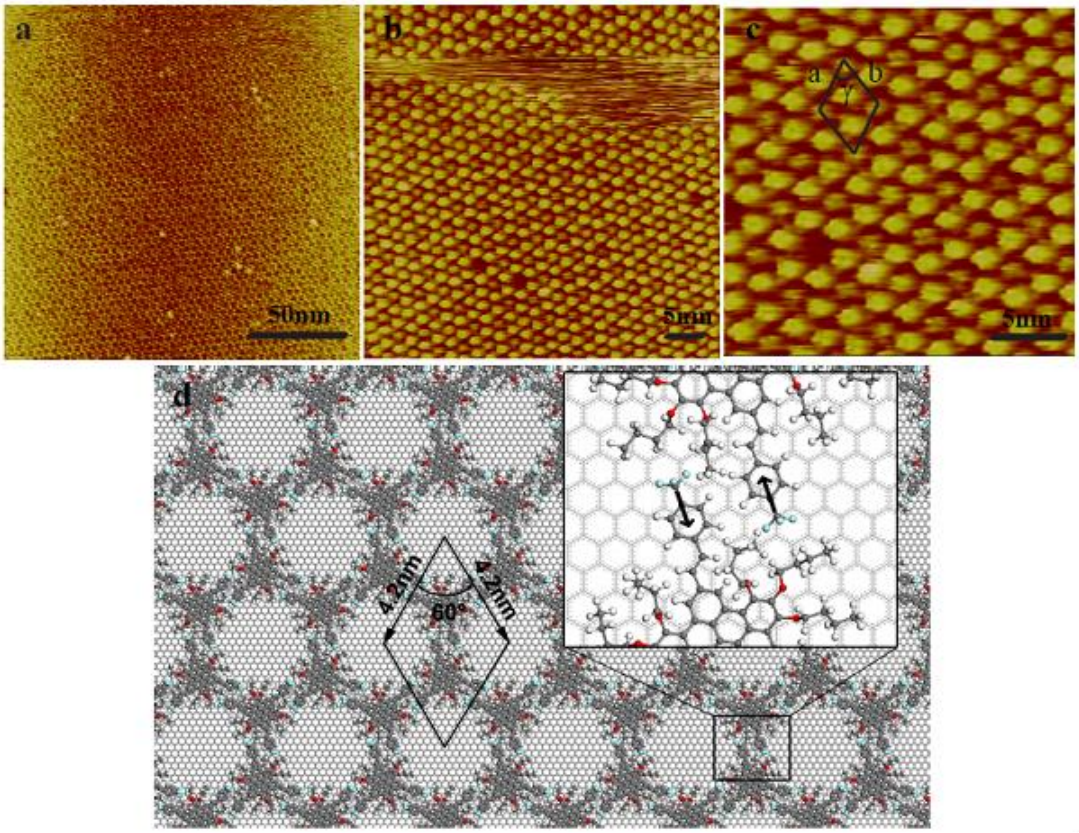

Figure 2.3 STM images and the simulated pattern of the HBC-CF_3 adlayer on the basal plane of HOPG: (a) large-scale STM image of HBC-CF_3 (200.0 × 200.0 nm^2, I_{set} = 0.15 nA, and V_{bias} = -1.2 V); (b) STM images of HBC-CF_3 (60.0 × 60.0 nm^2, I_{set} = 0.14 nA, and V_{bias} = -1.3 V); (c) high-resolution STM image of HBC-CF_3 (26.6 × 26.6 nm^2, unit cell: a = 4.0 ± 0.1 nm, b= 4.1 ±

0.1nm, and $\gamma = 60 \pm 2°$. I_{set} = 0.14 nA, and V_{bias} = -1.3 V); and (d) the simulated self-assembly pattern of HBC-CF_3 on graphite (0001) surface with the simulated unit cell of a = b = 4.2 nm, $\gamma = 60°$, where the inset shows the interaction pattern of the functional groups. (For the enlarged view of the functional group interaction pattern, some alky chains have been hidden for clarity.)[204] Reprinted with permission from reference 205. Copyright 2011 American Chemical Society.

The high resolution STM images (Figure 2.3b, c) revealed that the molecules are assembled in a hexagonal circle with one less bright spot inside. The bright areas correspond to the aromatic core of HBC-CF_3 because of the higher electronic density of state,[209] and the size of each bright spot also matches the molecular size of the HBC core. The less-bright spots are mostly due to the adsorption of solvent molecules.[198] Then, the question is, what is the driving force for the formation of such 2D porous network structures? Generally speaking, the strength of dipole-dipole interaction (5-50 kJ/mol) is stronger than that of van der Waals interaction (<5 kJ/mol) but weaker than that of hydrogen bonding (10-65 kJ/mol). As the alkyl chains on HBC core are too short to contribute significantly to the intermolecular interaction, dipole-dipole interactions built up between adjacent HBC-CF_3 molecules are considered to be the main driving force for their self-assembly behavior at the solid-liquid interface. From these, it is suggested that the C_3-symmetric HBC-CF_3 molecules self-assemble into a 2D honeycomb

network via the linking of six separate bright cores in a hexagonal pattern via the dipole-dipole interactions.

To have a better understanding of how HBC-CF_3 molecules can self-assemble on the graphite surface to form honeycomb structures, the self-assembly behavior of HBC-CF_3 molecules was simulated using the classical molecular mechanics method with the COMPASS[203] force field integrated in the Forcite module of the Materials Studio package. To approach global minimum as much as possible, molecular dynamics and simulated annealing have been performed for all structures. The simulated self-assembly pattern of HBC-CF_3 on graphite (0001) surface is displayed in Figure 2.3d. The substructure consists of a hexagon with one HBC-CF_3 molecule at each corner. Because the -CF_3 group is highly electronegative in nature, this 4-trifluoromethylphenyl part of the HBC-CF_3 molecules can be treated as a dipole, and the direction of the dipole moment is indicated in the enlarged image in Figure 2.3d. It is evident that the two dipoles are aligned in an anti-parallel fashion, which is viewed as a stabilized state and gives rise to a lower overall energy. These simulated results of HBC-CF_3 organization are in accordance with the experimental observation by STM, which further proves the intermolecular dipole-dipole interactions between HBC-CF_3 molecules to drive the formation of the 2D supramolecular architecture. In addition, the parameters of a unit cell in Figure 2.3c have been determined to be a = 4.0 ± 0.1 nm, b= 4.1 ± 0.1nm, and $\gamma = 60 \pm 2°$, which are in agreement with the calculated parameters of a

unit cell of HBC-CF_3 molecules, a = b = 4.2 nm, γ = 60°, as indicated in Figure 2.3d.

So far, 2D porous networks have been assembled by direction-oriented intermolecular forces like hydrogen bonding,[42, 126, 211] metal-ligand interactions,[215-216] and van der Waals interactions of interdigitating alkyl chains.[129, 217-218] Note that we presented here that the anti-parallel intermolecular dipole-dipole interactions are considered as the main driving force to form a 2D porous honeycomb structure, and this would be the first example to show that intermolecular dipole-dipole interactions can be used to form a 2D porous honeycomb structure. This 2D porous honeycomb structure of HBC-CF_3 provides the opportunity to form a guest-host system, which allows molecules of comparable size to be brought into the cavity to further modulate the electronic properties of supramolecular assemblies further.

2.3.4 Control Experiment of Non-specific Intermolecular Interactions

In order to confirm that the anti-parallel dipole-dipole interactions between HBC-CF_3 molecules are mainly responsible for the formation of the 2D nanoporous network, instead of the interactions between alkyl chains or between alkyl chain and substrate, a control experiment utilizing HBC-Cl was conducted, in which the –CF_3 groups were replaced by –CH_2Cl groups. The results revealed the importance of the intermolecular dipole-dipole interactions in 2D nanoporous

network formation. Similar to other HBC derivatives, HBC-Cl molecules in 1-phenyloctane also form stable and homogeneous monolayers on graphite (Figure 2.4a). From the high-resolution image (Figure 2.4b), one can observe bright spots that reflect the locations of the aromatic cores of HBC-Cl molecules due to higher electronic densities,[209] while instead of forming a honeycomb structure like HBC-CF_3, HBC-Cl molecules are assembled into a closely packed hexagonal motif. The parameters of a unit cell have been determined to be a = b = 2.0 ± 0.1 nm, γ = 60 ± 1°, which are very closely matched with the simulated results, a = 2.2 nm, b = 2.1 nm, γ = 62 °shown in Figure 2.4c.

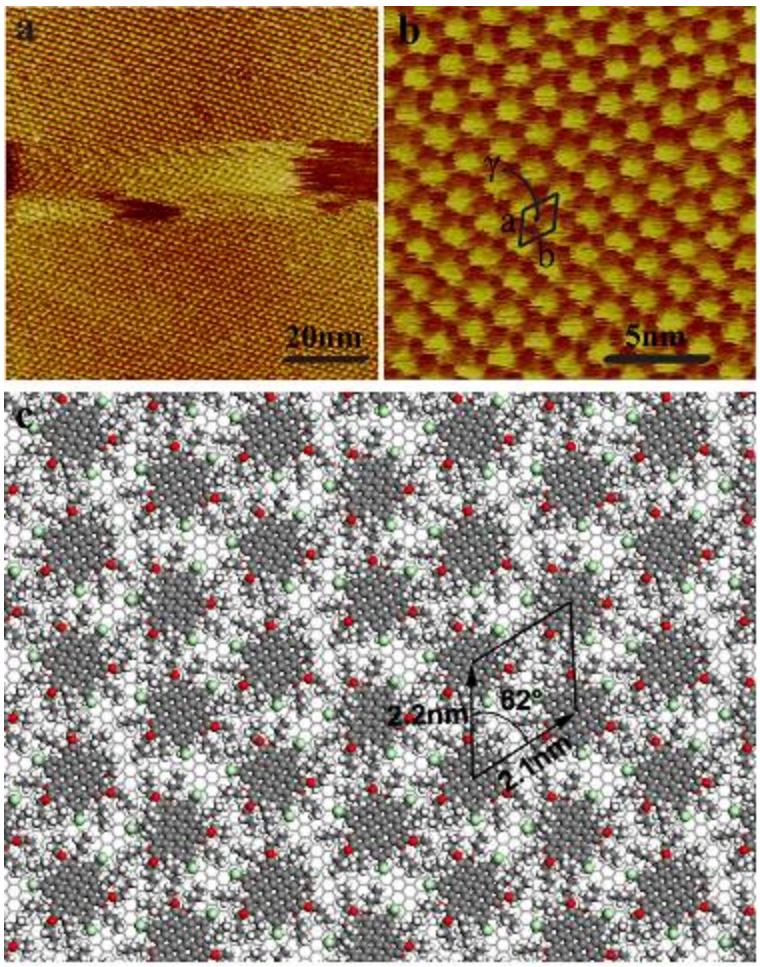

Figure 2.4 STM images and simulated patterns of the HBC-Cl adlayer deposited from 1-phenyloctane solution onto the basal plane of HOPG: (a) large-scale STM image of HBC-Cl (100.0 × 100.0 nm^2, I_{set} = 0.15 nA, and V_{bias} = -0.8 V); (b) high-resolution STM image of HBC-Cl (20.0 × 20.0 nm^2, unit cell: a = b = 2.0 ± 0.1 nm, γ = 60 ± 1°. I_{set} = 0.17 nA, and V_{bias} = -1.4 V); and (c) simulated self-assembly pattern of HBC-Cl on graphite (0001) surface with the simulated unit cell of a = 2.2 nm, b = 2.1 nm, and γ = 62°.[204] Reprinted with permission from reference 205. Copyright 2011 American Chemical Society.

By comparing the packing mode and the unit cell parameters of HBC-CF_3 and HBC-Cl, it is easily found that HBC-Cl molecules are not packed in the same manner as HBC-CF_3 molecules, not only in terms of the packing behavior but also in terms of the packing density. This is because the underlying mechanisms for intermolecular interactions for these two molecules are different, which is in agreement with our simulated results shown in Figure 2.4c. The simulated model for HBC-Cl indicates that there is no specific preferred interaction among molecules like in the case of HBC-CF_3. The HBC-Cl molecules are packed more densely than HBC-CF_3, which could provide a higher possibility for alkyl chain entanglement to contribute more to the intermolecular interactions through van der Waals interactions.

2.3.5 Other Functional Groups Induced Intermolecular Dipole-dipole Interactions

We further investigated the self-assembly of HBC derivatives bearing other electron-withdrawing groups, such as HBC-CN and HBC-NO_2. From STM images (Figure 2.5a, b, d, e), it is clearly seen that both HBC-CN and HBC-NO_2 form homogeneous and ordered large-area adlayers with a closely packed hexagonal motif, which is different from the 2D honeycomb structures for HBC-CF_3. The bright areas of the high resolution STM image correspond to the aromatic core of HBC-CN, and the spot size also matches by the molecular size of the HBC core. All of these spots have the same brightness, which is in contrast to HBC-CF_3 shown in Figure 2.3c. The parameters of a unit cell have been determined to be a = b = 2.6 ± 0.1 nm, and γ = 60 ± 2°, which are in agreement with the calculated parameters (a = b = 2.5 nm, γ = 60°) of a unit cell of HBC-CN molecules, as indicated in Figure 2.5c. Similarly, the parameters of a unit cell for HBC-NO_2 have been determined to be a = 2.5 ± 0.1nm, b = 2.6 ± 0.1 nm, and γ = 60 ± 2°, which are in close agreement with the calculated parameters (a = 2.3 nm, b = 2.4 nm, γ = 61°) of the unit cell of HBC-NO_2 molecules indicated in Figure 2.5f.

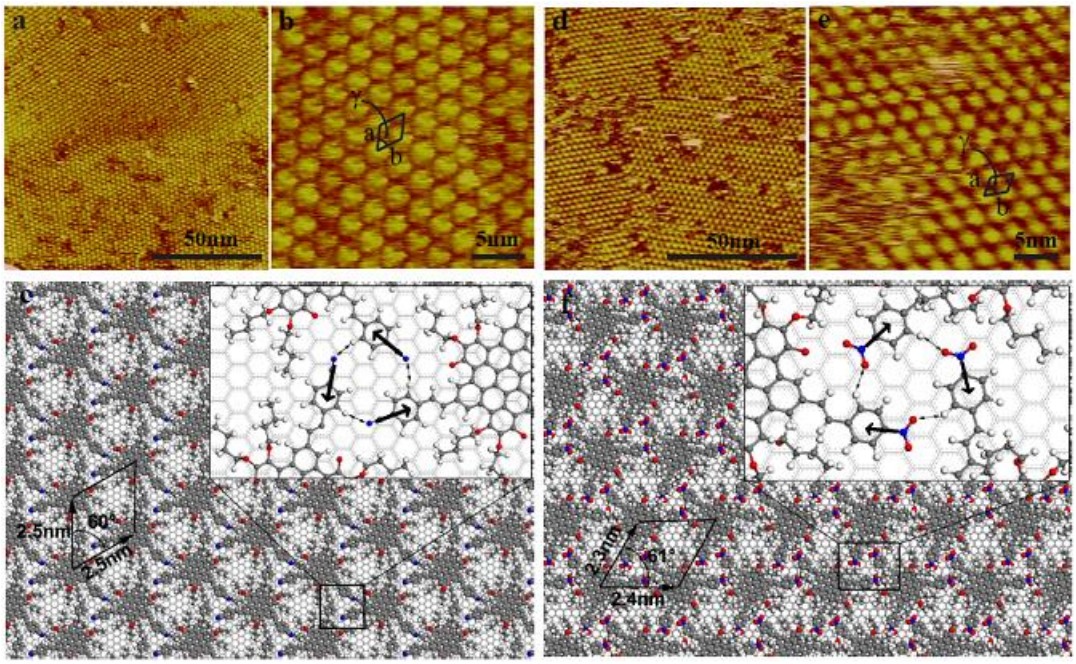

Figure 2.5 STM images and simulated patterns of the HBC-CN and HBC-NO_2 adlayers on the basal plane of HOPG: (a) large-scale STM image of HBC-CN (120.0 × 120.0 nm^2, I_{set} = 0.16 nA, and V_{bias} = -1.2 V); (b) high-resolution STM image of HBC-CN (25.0 × 25.0 nm^2, unit cell: a = b = 2.6 ± 0.1 nm, and γ = 60 ± 2 °, I_{set} = 0.15 nA, and V_{bias} = -1.4 V); (c) simulated self-assembly pattern of HBC-CN on graphite (0001) surface with the simulated unit cell of a = b = 2.5 nm, γ = 60°; (d) large-scale STM image of HBC-NO_2 (100.0 × 100.0 nm^2, I_{set} = 0.017 nA, and V_{bias} = -1.6 V); (e) high-resolution STM image of HBC-NO_2 (30.0 × 30.0 nm^2, unit cell: a = 2.5 ± 0.1 nm, b= 2.6 ± 0.1nm, and γ = 60 ± 2°, I_{set} = 0.017 nA, and V_{bias} = -1.6 V); and (f) simulated self-assembly pattern of HBC-NO_2 on graphite (0001) surface with the simulated unit cell of a = 2.3 nm, b = 2.4 nm, γ = 61°.[204] Reprinted with permission from reference 205. Copyright 2011 American Chemical Society.

In the simulated supramolecular model shown in the enlarged image of Figure 2.5c, it is suspected that the intermolecular interaction is dominated by interactions between the nitrile group (-CN) and hydrogens of the benzene group from the adjacent molecule. In other words, because of the electronegativity of the nitrile group, the 4-cyanophenyl unit itself forms an intrinsic dipole moment. Its direction is indicated in the enlarged images shown in Figure 2.5c. From the energy point of view, polarized molecules tend to align themselves in a way that minimizes the overall polarity and hence leads to a lower overall energy. That is exactly what we obtained in the simulated model where the 4-cyanophenyl group arranged themselves in a windmill pattern without a common center. If we sum up the dipole moment according to the rule of vector addition, the overall dipole moment around that area is actually zero. Hence, it leads to a lower energy state by forming this pattern, which is a hexagonal circle with one HBC-CN molecule inside. From the zoomed-in image of Figure 2.5e, it can be assumed that the intermolecular interaction is dominated by the weak [C─H•••NC─] hydrogen-bonding interactions between -CN groups and hydrogen of the benzene groups on the adjacent molecule. Similarly, the proposed molecular model for HBC-NO_2 shown in Figure 2.5f also reveals a self-assembly pattern of hexagonal circle with one molecule inside on the HOPG substrate. A similar explanation for HBC-CN can also be applied to HBC-NO_2, by considering the direction of the dipole moment for the 4-nitrophenyl group and additional [C─H•••O_2N─] hydrogen-

bonding interactions, and the packing pattern is shown in the enlarged image in Figure 2.5f.

2.4 Conclusion

By rationally designing a HBC-COOH molecule bearing three carboxylic groups, their self-assembly were able to form a 2D honeycomb network via hydrogen bonding. Since the strength of dipole-dipole interaction is comparable with hydrogen bonding, we designed a series of HBC derivatives bearing electronegative functional groups, and also synthesized HBC-Cl as a control experiment, due to non-specific intermolecular interaction. Along the way, the STM experimental results are correlated with simulated models, and the detailed intermolecular interactions were proposed one by one. HBC-CF_3 was the first example to demonstrate that it is possible to obtain a 2D honeycomb network via intermolecular dipole-dipole interaction.

In conclusion, we have shown how intermolecular dipole-dipole interactions could enable fine control over the self-assembly of disklike π-conjugated molecules. The new large-size aromatic carboxylic acid HBC-COOH can self-assemble into a highly porous and rigid 2D honeycomb network via intermolecular hydrogen bonding interactions at a 1-phenyloctane-HOPG interface. In addition, the antiparallel intermolecular dipole-dipole interactions between HBC-CF_3 molecules are considered to be the main driving force in forming a 2D

porous honeycomb structure, and this is the first example to show that intermolecular dipole-dipole interactions can be used to form a 2D porous honeycomb structure, although for HBC-CN and HBC-NO_2, they could form hexagonal superstructures as a result of a special trimeric arrangement induced by dipole-dipole interaction and weak hydrogen-bonding. Molecular mechanics and dynamics simulations were performed to prove the detailed functional group interactions as well as the 2D superstructures. In this sense, a delicate balance between the different substituents of the molecular building blocks is important for engineering the interfacial supramolecular structures of HBC derivatives.

Chapter 3 HOST-GUEST SYSTEM FROM 2D NANOPOROUS NETWORK

In the preceding chapter, we present how to establish a 2D nanoporous network. In the meantime, this chapter continues to explore how interactions of molecule, substrate and solvent enable fine control over the self-assembled structures at solid-liquid interface. We report that HBC-COOH formed a rigid two-dimensional (2D) honeycomb network at solid-liquid interface via intermolecular hydrogen bonding interactions. Guest molecules such as coronene can be filled into the cavities of this porous 2D network.

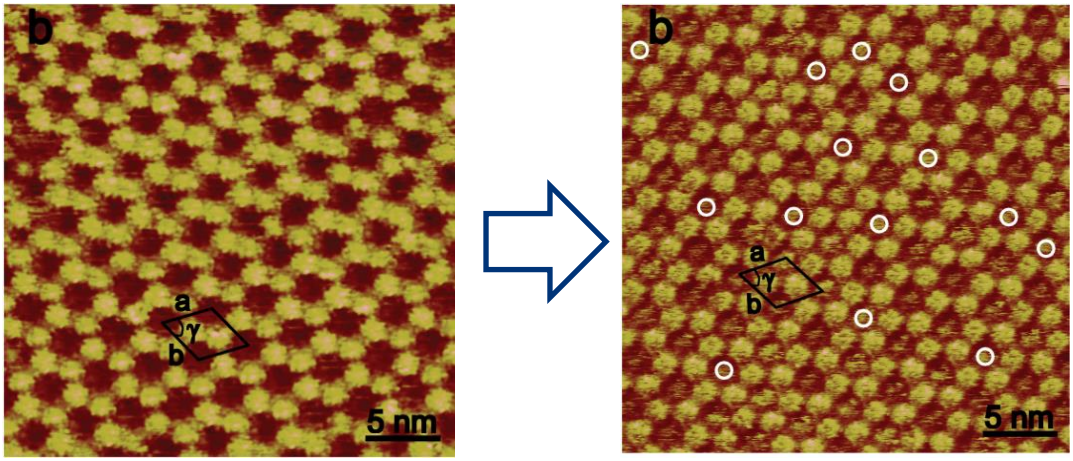

3.1 Introduction

The self-assembly of a molecular building unit at the solid-liquid interface is driven by weak interactions with the substrate, solvent and the molecule itself.

One interesting pattern for such self-organized molecular adlayers at solid-liquid interface is the 2D porous network, which can be achieved by hydrogen-bonding interactions of appropriate building units.[35, 93, 219] For example, simple trimesic acid[126, 210-211] (TMA, known as benzene-1,3,5-tricarboxylic acid) can form a 2D rigid honeycomb network via intermolecular hydrogen bonding interactions. The size of the cavity in the network can be further expanded by using larger size building blocks such as C_3 symmetric benzenetribenzoic acid (BTB)[220] and star-shaped oligofluorene carboxylic acids.[221] Guest molecules such as fullerene can fill in the cavities of some of the 2D porous networks to form a host-guest structure at solid-liquid interface.[222] Due to the existence of large-size cavities within the hexagonal lattices, the self-assembled network formed by HBC-COOH can act as a supramolecular host system to study the interactions between guest molecules (e.g. coronene) and the nanoporous network.

3.2 Experimental Section

3.2.1 STM Imaging

Prior to imaging, compounds under study were dissolved in 1-phenyloctane (Aldrich, 99%), and a drop of this solution or mixed solution was applied to a freshly cleaved surface of highly oriented pyrolytic graphite (HOPG). STM experiments were performed using a scanning probe microscope (Veeco Multimode SPM system with a NanoScope V control station) in constant current mode under ambient conditions. STM tips were prepared by mechanically cutting a

0.25 mm thick Pt/Ir (80/20) wire. All STM images contain raw data and are not subjected to any manipulation or image processing.

3.2.2 Molecular Mechanics and Dynamics Simulation.

The formation of interfacial supramolecular structures was investigated by a classical molecular mechanics method with the COMPASS force field integrated in the Forcite module of the Materials Studio package. The detailed information has been explained in the previous chapter.

3.3 Results and Discussion

3.3.1 Rational Design of a Host-guest System

From the previous chapter, we know that the diameter of the HBC-COOH self-assembled circular cavity is about 1.8 nm (Figure 3.1b), indicating that some guest molecules with appropriate size and interactions can be accepted by the pores. Thus six-fold symmetric coronene with a lateral diameter of about 1 nm (Figure 3.1b) was chosen as a guest molecule. According to previous investigations,[126] coronene molecules at the liquid-solid interface without host architecture did not show ordered structures.

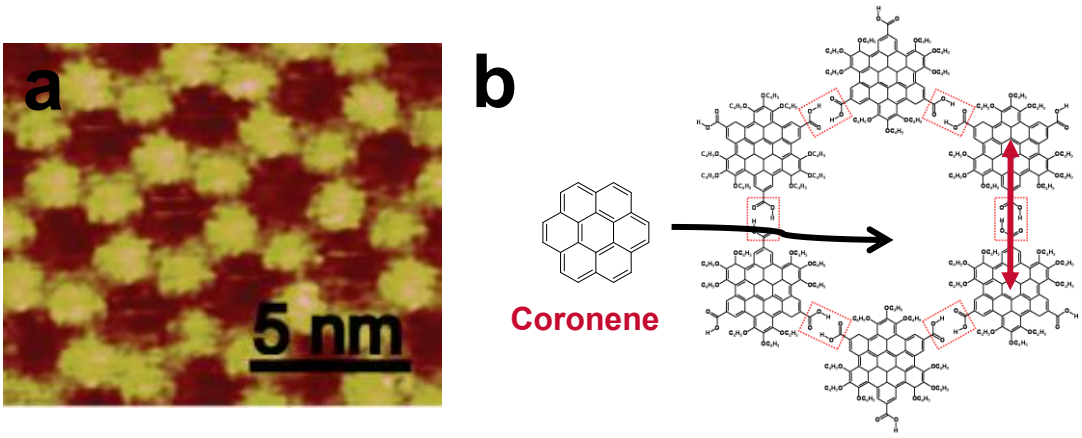

Figure 3.1 The rational design of a host-guest system: (a) 2D honeycomb network formed by HBC-COOH network at the solid (HOPG) – liquid (1-phenyloctane) interface. (b) Explanation of molecular dimensions of coronene and 2D nanoporous network.

3.3.1 HBC-COOH with Coronene

The highly porous honeycomb-like structure presents the opportunities to bring guest molecules into the host cavities. Addition of coronene to the solution of HBC-COOH in 1-phenyloctane and subsequent STM imaging measurements exhibited a similar 2D network with a hexagonal lattice (Figure 3.2a). At first, the ratio between host and guest molecules was 1:1. The lattice constant of the hexagons is nearly same as that of the pure HBC-COOH molecules, indicating that the 2D framework is formed by the HBC-COOH itself. Interestingly, some of the cavities are now filled with smaller-size and less-bright spots, which can be identified as coronene molecules based on the

size and the different contrast. Therefore, the 2D honeycomb network formed by HBC-COOH actually serves as a template to induce the assembly of the coronene molecules on the HOPG surface. The reason why the coronene molecules can go into the cavities could be ascribed to the size and shape matching between nanosized pores and the planar D_{6h} symmetric coronene molecules.

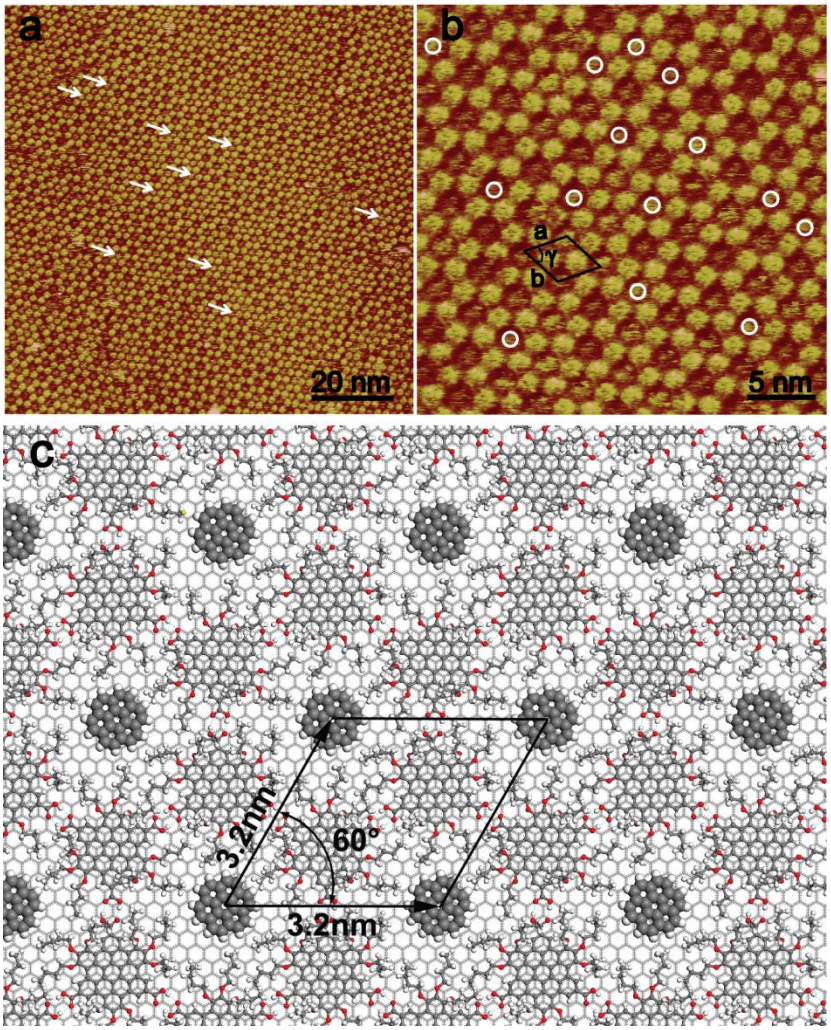

Figure 3.2 STM images and simulated patterns after adsorption of coronene

guests within the supramolecular honeycomb network at the solid (HOPG) – liquid (1-phenyloctane) interface: (a) large-scale STM image of HBC-COOH with Coronene inside (100 × 100 nm^2, I_{set} = 0.16 nA, and V_{bias} = -0.8 V); (b) high-resolution STM image of HBC-COOH with Coronene inside (30.3 × 30.3 nm^2, unit cell: a = 3.2 ± 0.1 nm b = 3.1 ± 0.1 nm, γ = 59 ± 1°. I_{set} = 0.16 nA, and V_{bias} = -0.8 V); and (c) simulated self-assembly pattern of HBC-COOH with Coronene inside on graphite (0001) surface with the simulated unit cell of a = b = 3.2 nm, and γ = 60°.

It is noteworthy that although most of the cavities can be filled with coronene molecules, the contrast of all the coronenes is different throughout, implying that the interaction between the coronene molecules and the HOPG substrate is relatively weak. This probably could be owing to the underlying aliphatic chains of HBC molecules between the coronene and HOPG surface which reduce the π-π interactions between the coronene and the HOPG. In fact, a weaker interaction and a dynamic phase transition of HBC molecules on long aliphatic chains modified HOPG surface were previously observed.[223] The non-perfect size matching may also have negative effect on the hosting of coronene in the framework.

In order to discover an optimized condition of adsorbing coronene molecules inside HBC-COOH honeycomb network, experiments with different host/guest ratio has been conducted. In Figure 3.3, it was shown that the

coronene adsorption with host/guest ratio of 1:0.5 (Figure 3.3a and b) and 1:2 (Figure 3.3c and d). From both the large scale images and high resolution imges, it is revealled that the adsorption behavior of individual coronene molecules into the porous cavities act similarly with the case of 1:1 ratio. Therefore, we could conclude that the host/guest raito didn't affect the adsorption of coronene inside the host honeycomb network significantly. And in order to understand the reason for the different contrast of coronene molecules inside the cavity, a dynamic equilibrium process is proposed in the next section.

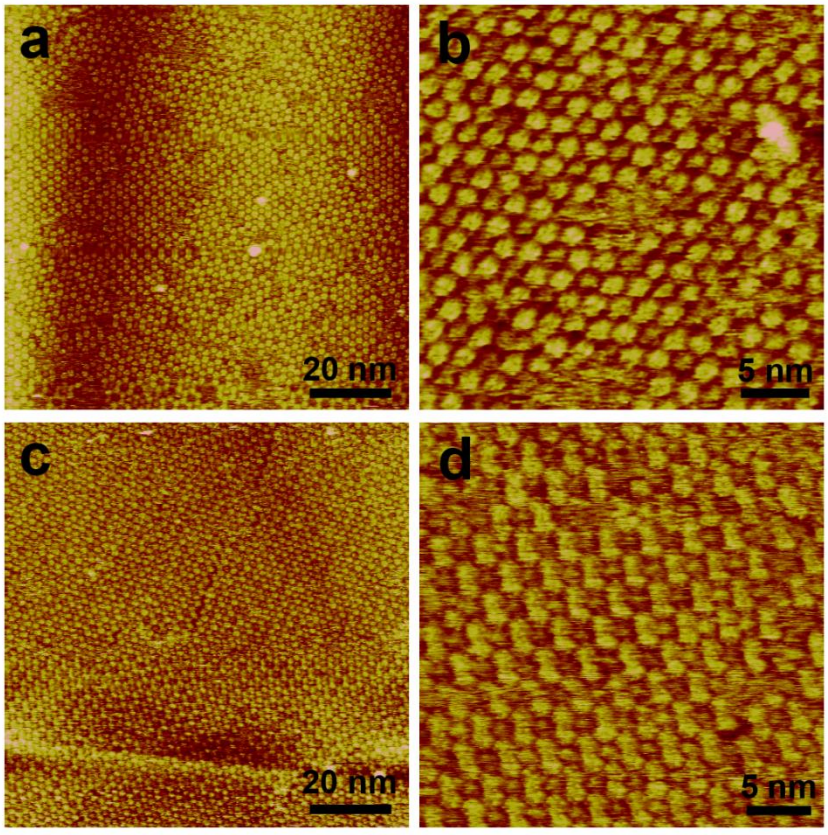

Figure 3.3 STM images of adsorption of coronene guests within the supramolecular honeycomb network with different host/guest ratio at the solid

(HOPG) – liquid (1-phenyloctane) interface: (a) large-scale STM image of HBC-COOH with Coronene inside, with host/guest ratio of 1:0.5 (100 × 100 nm^2, I_{set} = 0.16 nA, and V_{bias} = -0.8 V); (b) high-resolution STM image of HBC-COOH with Coronene inside, , with host/guest ratio of 1:0.5 (30.0 × 30.0 nm^2, I_{set} = 0.17 nA, and V_{bias} = -0.8 V); (c) large-scale STM image of HBC-COOH with Coronene inside, with host/guest ratio of 1:2 (100 × 100 nm^2, I_{set} = 0.165 nA, and V_{bias} = -0.8 V); and (d) high-resolution STM image of HBC-COOH with Coronene inside, with host/guest ratio of 1:2 (33.0 × 33.0 nm^2, I_{set} = 0.165 nA, and V_{bias} = -0.8 V).

3.3.2 Dynamic Equilibrium

In order to understand the reason for different contrast of coronene molecules inside each cavity, molecular mechanics and dynamics simulations were performed, and the adsorption and desorption of the coronene were studied respectively. The desorption energies were calculation by manually adjusting relaxed structure with the coronene molecules adsorbed in the cavity until the coronene-substrate distance is larger than the van der Waals cut-off distance. The adsorption energies were calculated by manually adjusting the coronene molecules well above the relaxed HBC-COOH supramolecular structure until the optimum coronene adsorption distance of ~3.5Å is reached. During the manual adjustment of coroene-substrate distances, no further geometry relaxations were performed. For better understanding the role of alkyl chains, a reference structure without alkyl

chains attached to HBC-COOH molecules has also been studied. All results are given in Figure 3.4. It is not surprising to observe a typical van der Waals potential curve is recovered for the case of the reference system as given by the black curve in Figure 3.4. Therefore coronene molecules have very little interaction with the HBC-COOH aromatic backbone.

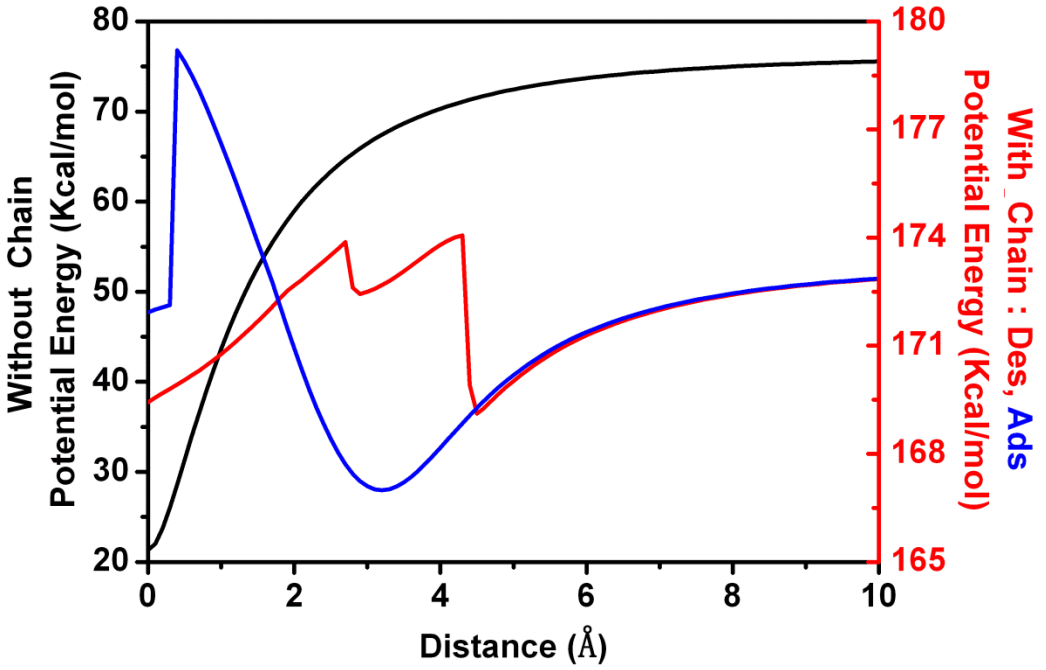

Figure 3.4 Potential energy for HBC-COOH molecule with and without alkyl chains with respect to distance between adsorbates and substrate, where the zero point was taken as the equilibrium position of the coronene moelcules on the substrate (~3.5Å above the substrate).

While for the actual HBC-COOH molecules as given by red and blue curves, very interesting different behavior between the desorption and adsorption process for coronenes in HBC-COOH can be obtained. Both adsorption and desorption process has shown multiple minimum feature. There appears to have more than one potential energy barrier before the coronene molecule getting away from or getting close to the final equilibrium position. Comparing to the potential energy curve of the reference system, the role of alkyl chains can be understood as either hindering the adsorption of coronene molecules into the cavity or hindering the desorption of coronene molecules that have been adsorbed in the cavity. For the adsorption processes, when the coronene molecules are getting closer to the HBC-COOH porous network, they will first feel the van der Waals surface of the alkyl chain above the backbones. Therefore one can observe the first minimum around 3Å (or ~6.5Å above the substrate). The repulsion from the alkyl chains becomes higher when the coronene molecules are getting closer to the substrate. Such high repulsion from the alkyl chains may lead to a potential energy barrier for coronene molecules to be further adsorbed into the cavity. However caution must be taken that such static energy may not reflect the actual dynamics situation, where relaxation of the alkyl chains may lower the adsorption potential energy barrier for the coronene molecules. Regarding the desorption processes, the alkyl chains may play the role of locks that can introduce further potential energy barriers for the coronene molecules to overcome. In the other words, once the coronenes enter the cavities in the 2D nanoporous network formed by HBC-COOH molecules, they may not be able to exit the cavity easily.

Therefore, despite the different contrast of coronene molecules inside individual cavities, most of the cavities are filled with one coronene molecule inside. In addition, it confirms that aliphatic chains are the main root cause for the dynamic process to happen. Therefore, the coronene molecules exist in a dynamic equilibrium between free molecules in solution and trapped molecules in the 2D nanoporous network.

3.4 Conclusion

In conclusion, a novel D_{3h} symmetric HBC tricarboxylic acid molecule **HBC-COOH** can self-assemble into a highly porous and rigid 2D honeycomb network via intermolecular hydrogen bonding interactions at a 1-phenyloctane-HOPG interface. Because of the existence of large-size cavities within the hexagonal lattices, the self-assembled network can act as a supramolecular host system to study the interactions between guest molecules (e.g. coronene) and the nanoporous network.

And in order to explore the optimized condition for this host-guest system, HBC-COOH + Coronene, different ratios between host/guest molecules were conducted. Such as 1:1 as the reference line, ratio of 1: 0.5 and 1: 2 were tested for comparison. With varying the value of host/guest ratio, no significant effect was observed. Most of the pores are filled with coronene molecules inside for all three

kinds of host/guest ratio, although the brightness of each coronene molecule is different among each other.

With the help of molecular mechanics and dynamics, we revealed that despite the different contrast of coronene molecules inside individual cavities, most of the cavities are filled with one coronene molecule inside. Moreover, it confirms that aliphatic chains are acted either as a hindering for coronene molecules to adsorb, or as a shield for trapping the coronene from desorption. Therefore, the coronene molecules exist in a dynamic equilibrium between free molecules in solution and trapped molecules in the 2D nanoporous network.

Chapter 4 PHOTOCURRENT MAPPING IN CHEMICALLY MODULATED GRAPHENE

In this chapter, we show that in addition to the structural behavior of supramolecular assemblies, their functional properties also have a great influence toward the performance of supramolecular electronic devices. Beyond the passive characterization of supramolecular assemblies, light induced photoresponse of large 2D π-conjugated assemblies, graphene, will be investigated. With nanoscale resolution of photocurrent mapping, the chemically modulated graphene-photoresponse is studied systematically.

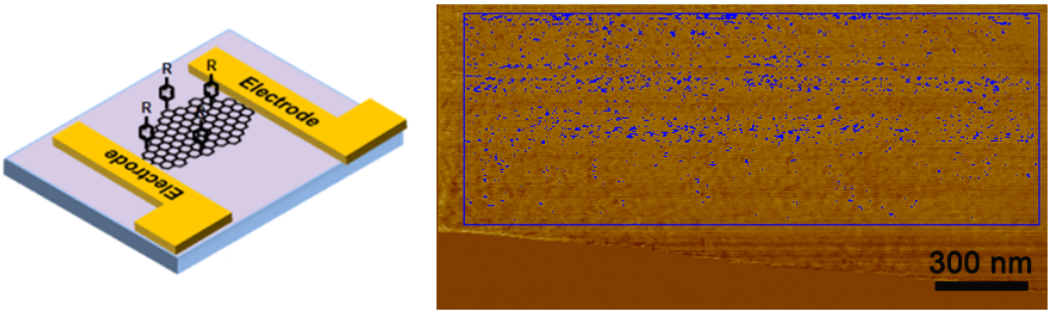

4.1 Introduction

After systematic investigation of how intermolecular interactions affect the self-assembly behavior of some novel organic molecules, another interesting aspect to look for in the field of supramolecular assemblies is their functional properties.

We have shown ways of establishing two dimensional honeycomb networks via specific intermolecular interactions, specifically speaking, via hydrogen bonding, and dipole-dipole interactions. In order to have an extended 2D structure, bottom-up approaches like synthesizing large π-conjugated molecules, then later self-assembly, has been intensively studied.[23, 27, 45, 143, 205, 213] However, these 2D structures are all formed at solid-liquid interface, which makes them difficult to be used for device fabrication directly. Therefore, bearing in mind to look for extended large area of π-conjugated system in the solid state, we found graphene to be the perfect candidates, which can be viewed as a top-down approach to fabricate such 2D π-conjugation extended structure.

Graphene has a perfect 2D atomic structure of sp^2 carbon atoms, and has become a star material due to its unique properties, such as mechanical, electrical, thermal, and optical.[224-232] Particularly, graphene exhibits supreme properties in photonics and optoelectronics, such as wavelength-independent light absorption and high operating bandwidth, which make it one of the most competent and attractive candidates for important applications, such as optical modulator, mode-locked laser, and photodetector.[228, 230, 233-238] Recently, graphene photoresponse has become one of the most important and hot topics among numerous graphene related fields.[239-241] However, one of the challenges has been to generate stable graphene photoresponse, owing to the fast recombination (in picoseconds level) of electron-hole pairs upon light radiation.[242-243] Therefore, to realize how the separation of the photo-generated electron–hole pairs leads to the photoresponse

simply, efficiently, and stably has become the top priority in the field of graphene related photonics.

Most of the current strategies depending on asymmetric electrodes or plasmonic structures have been developed to break the mirror configuration of p-n junctions and realize the photoresponse in graphene.[244-251] Nevertheless, these extrinsic methods suffer from the problem of extracting an insufficient amount of photoelectrons due to a less effective p–n junction. Hence, it is critical to find an intrinsic method to generate the photoresponse of pristine graphene. Graphene covalent functionalization, which transforms hybridized orbitals of graphene carbon atoms from sp^2 to sp^3, can create a bandgap in graphene and may lead to intrinsically changing of its optoelectronic properties with good stability, controllability, and repeatability.[252-253] Meanwhile, the covalent functionalization could also obviously change the surface potential of resulting graphene, which relates to the gas adsorption/desorption closely and could be tuned by different density or types of substituted decorators.[254-255] Thus, it is significant to find a simple and controllable method to realize the photoresponse of graphene based on chemical modulation. This could not only open a bandgap to exploit intrinsic capability of graphene itself in terms of photo-generated electron–hole pairs but also and modulate its ability through interaction between decorated graphene and gas molecules under ambient condition.

Since graphene is very stable, radical reactions are preferred in graphene modifications such as photochemical chlorination,[256] photochemical reaction of peroxide,[257] and diazonium chemistry,[258] wherein diazonium chemistry has been widely used in silicon-based materials for tailoring their electrical properties[258-260] due to easy and controllable operations.[261] Also, the substituent on the phenyl groups (electron-withdrawing/donating groups) can be flexibly altered in diazonium chemistry, which enables functionalizing graphene with various aryl diazonium salts. Hence, the surface potential on graphene can be modulated, which is important to the interaction with gas molecules.[254-255]

In this chapter, we report the fabrication and characterization of graphene-photoresponse devices based on chemical modulated single layer graphene (SLG) with designed decorator. The characterization is not only done with respect to the whole device; local information like current mapping is also obtained by using conductive AFM (C-AFM) at the nanoscale, in order to understand the spatial correlation between graphene-photoresponse and its functionalization.

4.2 Experimental Section

4.2.1 Synthesis of 1-Naphthalene Diazonium Tetrafluoroborate (NaphDT)

The synthesis of NaphDT occurs in a cold environment, supplied by a water-ice bath. The solution of sodium nitrate (45 mg, 0.65 mmol) in Milli-Q water (0.25 mL) was added slowly to 1-naphthylamine (84.4 mg, 0.59 mmol) in 1 M HCl

(1 mL) drop by drop. Then the whole reaction was carried out at about 1 ℃ for 1 hour. After that, 0.6 mL of a saturated solution of sodium tetrafluoroborate/ Milli-Q water was added. The yellowish product of NaphDT was precipitated and then purified by several rinse with cold diethyl ether and acetonitrile. The final product of NaphDT is in power form and about (61.4 mg, 43%). The yield of synthesized phenyldiazonium tetrafluoroborate is 51.3%.

4.2.2 Device Fabrication and Characterization

Single layer graphene was obtained by the mechanical exfoliation method from natural graphite flake on doped silicon wafer with 280 nm SiO_2. Electrodes are thermally evaporated with Au (50 nm) on Ti (10 nm), which were patterned by single E beam lithography. The functionalization of graphene was carried out by immersing the chip in 5 ml of a 10 mmol L^{-1} solution of diazonium salt in SDS solution (1%) in the dark overnight at room temperature (298 K). After functionalization, the chip was cleaned in SDS solution (1 %) and Milli-Q water and then dried in the air. The devices were characterized with a standard probe station and semiconducting parameter analyzer (Keithley 4200). Light irradiation was performed with 500 nm (up to 8 $mWcm^{-2}$) light generated by a 150W (Olympus LG-PS2-5) Xe lamp source. The local area of the graphene device was characterized using a conductive AFM system with TUNA module (Veeco Multimode SPM system with a NanoScope V control station). The probe was coated with 3nm chromium and 20 nm platinum for good conductivity, with a

radius of 20 nm. Each tip was checked by scanning electron microscopy (SEM) to ensure consistent tip radius and good quality of the conductive film. Light irradiation was performed with 500 nm (~ 4.2 $mWcm^{-2}$) light generated by a 150W Gilway halogen lamp source. The power intensity of the light was measured by using a PM100 optical power meter (Thorlabs, GmbH Manufacturing Facility) under the same experimental conditions.

4.3 Results and Discussion

4.3.1 Chemical Modulation and Characterization

In a typical experiment, the SLG device is characterized by scanning electron microscopy (SEM, Figure 4.1b). And then the SLG devices are functionalized with diazonium salts (naphthalene-1-diazonium tetrafluoroborate (NaphDT), 10 mM in 1% sodium dodecyl sulphate (SDS) solution) (Figure 4.1a). The R represents the functional group, in this case, it is one phenyl group. Typical Raman spectra of SLG devices were performed before and after chemical modification. In Figure 4.1c, the SLG can be recognized from the intensity ratio of 2D band to G band (≈ 4-fold),[262] and the absence of D-band provided evidence for the defect-free nature of pristine graphene (black curve); while after the modification, an obvious D band can be observed which can be identified as the formation of the covalent bond and the signal ratio between the D and G line (1370 cm^{-1} to 1540 cm^{-1}) was also elevated which was interpreted as a sign of sp^3 carbon formation.[263] (Figure 4.1c, red curve)

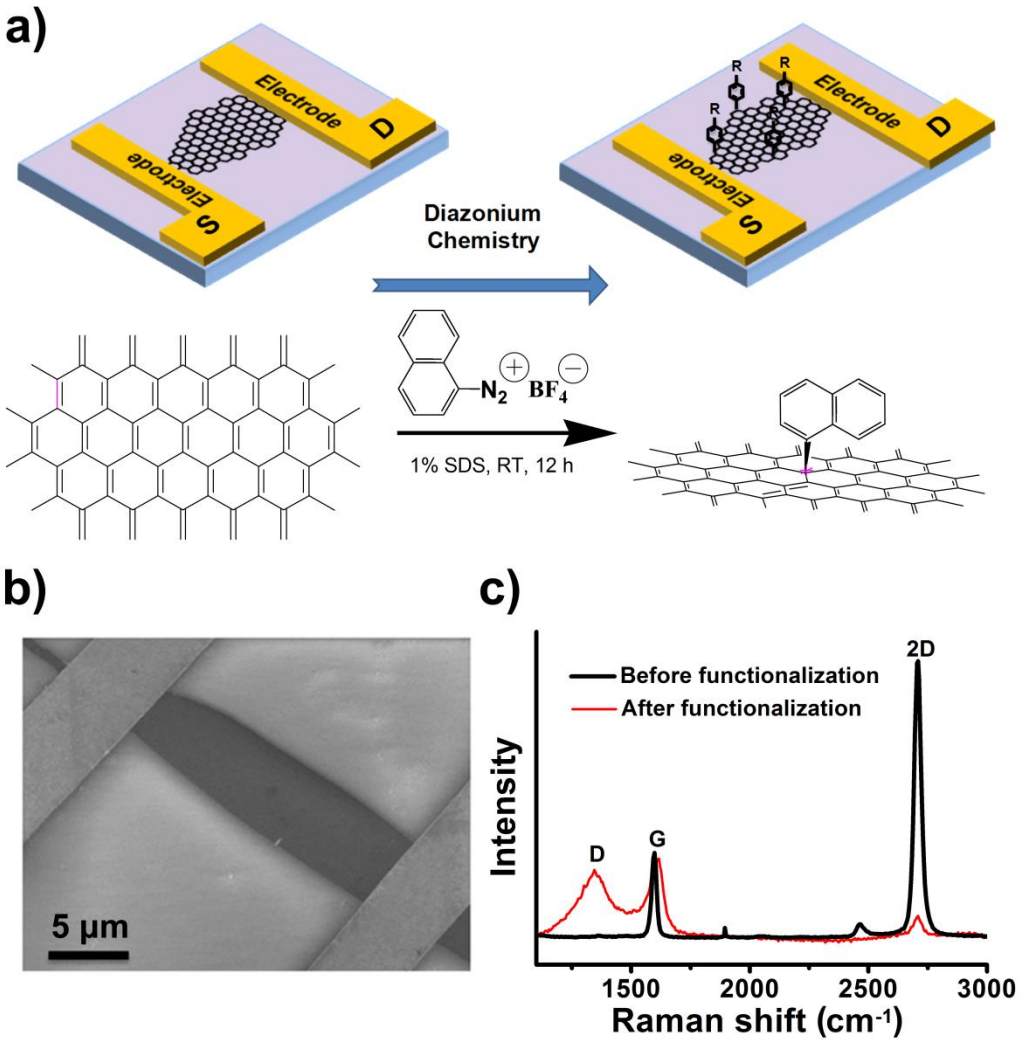

Figure 4.1 Graphene device fabrication and functionalization: a) Schematic illustration of device fabricating using SLG and covalent modified SLG via diazonium chemistry, and radical reaction of diazonium salts with graphene. b) Scanning electron microscopy image of the device. c) Raman spectra of SLG device before (black) and after (red) the covalent decoration.

4.3.2 Device Performance

Current-voltage (*I*-*V*) characteristic behaviors of NaphDT-SLG device was studied as an example in the absence and presence of light illumination (Xe lamp, 500 nm filter and 8 mW cm^{-2}) at ambient conditions. The linear relationship of *I*-*V* curves exhibited is due to the Ohmic contact between graphene and electrodes. (Figure 4.2a) For the SLG device, only weak photoresponse can be observed, however, for the NaphDT-SLG device, repeatable positive photocurrent ΔJ($\Delta J = (J_{irr} - J_o)/J_o \times 100\%$) was acquired by around 25% compared to its original current (Figure 4.2b). Furthermore, the photoresponse changed little with light intensity and wavelengths variation. On one hand, the photoresponse of NaphDT-SLG device is linear up to a total optical incident light on the entire device of 14 μW cm^{-2}, and a ΔI (variation of current) of 21% is observed.

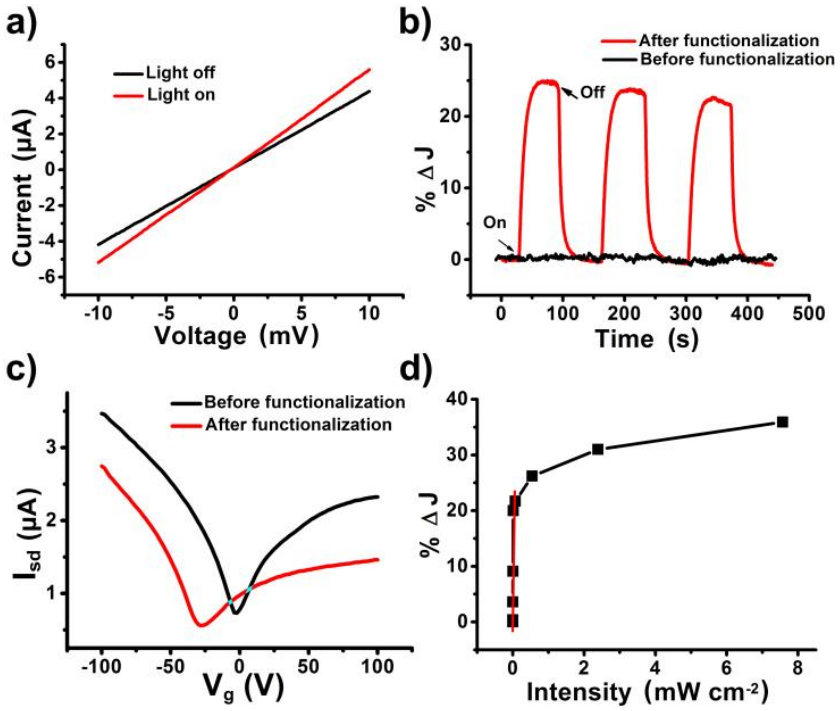

Figure 4.2 Electrical characterization of modified graphene device: a) I-V behaviour of NaphDT modified graphene device with and without light irradiation. b) Photoresponse of graphene device before (black) and after functionalization (red) with NaphDT. c) Gate dependent characteristic behavior of the pristine graphene device before (black) and after (red) the functionalization with NaphDT. d) Relationship of current density variation (ΔJ) and light intensity.

The transfer characteristics of the device were measured by applying a fixed source-drain bias voltage (V_{sd} =10 mV) and sweeping the gate voltage (V_g) between +100 V and -100 V in 1 V steps (Figure 4.2c). An ambipolar behavior with a threshold voltage (V_{th}) at ~ -0.5 V for the pristine graphene device before the

modification of NaphDT has been observed. On the contrary, after the modification, the V_{th} shifted to ~ -27 V indicating that the graphene device possessed an n-type semidonductor behavior. Furthermore, the photoresponse of NaphDT-graphene device is linear up to 14 μW cm^{-2} of optical incident light, accruing 21% variation in current density (Figure 4.2d, red line). Further increase in the light intensity leads to photocurrent saturation due to the screening effect as in conventional photodiodes.[264]

4.3.3 Local Electrical Information by C-AFM

After the device was fabricated and chemical modulation was done via diazonium chemistry, the local area of the modified graphene was tested by C-AFM. One of the electrodes was connected out to the sample holder of C-AFM, and the conductive probe acts as the other electrode and generates morphological and photocurrent images simultaneously with controlled light illumination. The current sensitivity used is 100nA/V and the bias is applied from the sample holder, then to the Au electrode of graphene device, passing through graphene, and then to the conductive tip as shown in Figure 4.3. With this setup, the current image could be obtained at the same time with the topographic image, and the size of each pixel is about 4 nm, which reveals current in a nanoscale spatial distribution.

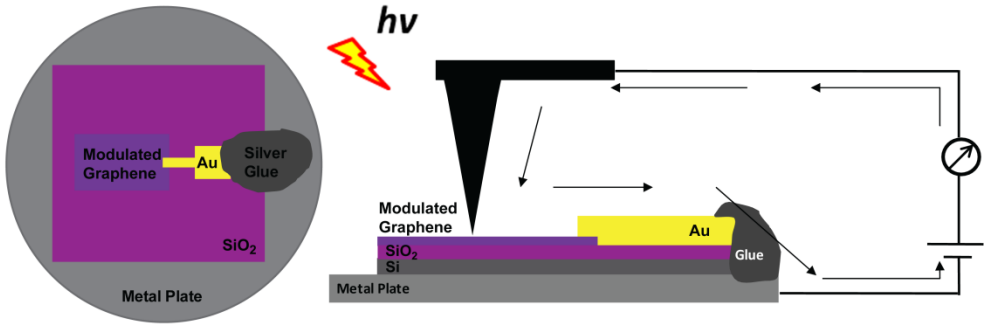

Figure 4.3 Setup of C-AFM for measuring photocurrent mapping at local area of modulated graphene devices.

4.3.4 Control Experiment of Pristine Graphene

Before characterizing the localized area of the modulated graphene device, the device fabricated with pristine graphene without functionalization is measured with C-AFM as a control experiment, in order to see if photoresponse occurs in this case. The topography and thickness profile of a pristine graphene without functionalization is shown in Figure 4.4 for the purpose of clarifying the monolayer feature of graphene.

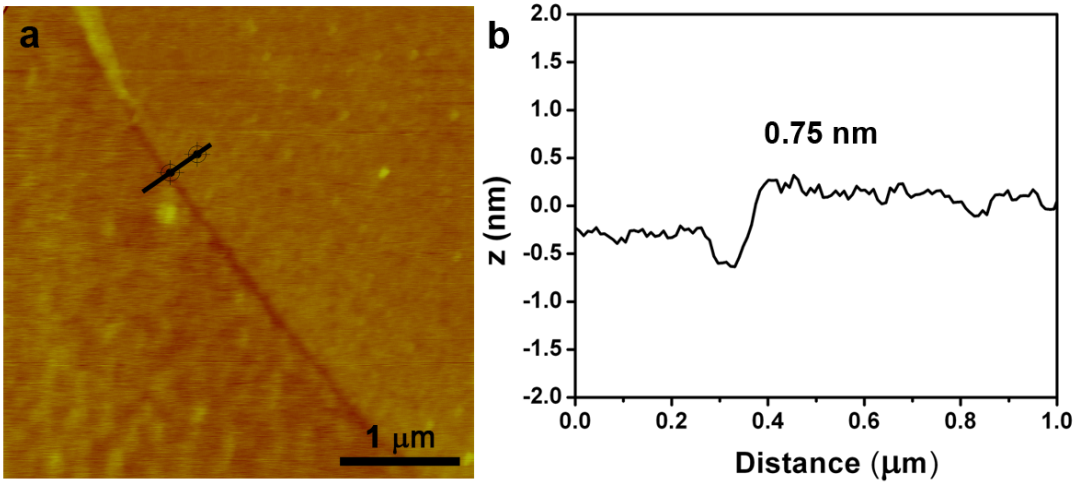

Figure 4.4 Topography of pristine graphene at local area: a) Topography image of pristine graphene by AFM. b) The height profile indicates the thickness of the pristine graphene as 0.75 nm.

Before we tested the photoreponse of the pristine graphene at the nanoscale, we carefully verified the appropriate force onto the graphene from the AFM probe, by getting the current image identical from two subsequent images with opposite scanning directions, to ensure that the measured result is reflecting the real properties of graphene rather than the technical problems, like a contact issue. We find that a conduct force about 125 nN from the tip to graphene surface guarantees the most stable measurement condition, and we try to keep this value for all the measurements done. The value of the contact force is estimated from the spring constant of the conductive probe from thermal tuning and deflection sensitivity from force curve ramping. As you can see the two current images taken under dark and light conditions respectively with a sample bias of 3 mV applied from the sample holder (Figure 4. 5a, b), they have almost the same current value, revealed

from similar color of current mapping. And if we get the profile section at the same location, we can find that there is barely any difference between them (Figure 4.5c). The calculated variation of current value is about 0.3% with regard to original dark current, which indicates it has very weak photoresponse.

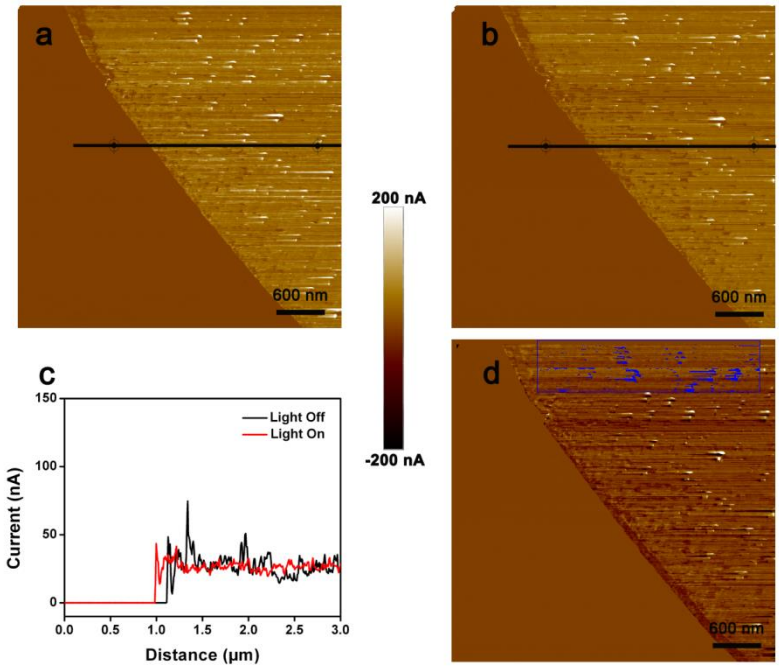

Figure 4.5 Photocurrent mapping of pristine graphene at local area: a) and b) Current mapping of NaphDT modified graphene device with and without light irradiation. c) The photocurrent profile with and without light irradiation, the variation of current is about 0.3% with regard to original dark current. d) The subtraction of current image between a and b; the averaged variation of current value with respect to dark current at the matched area is about 0.5%.

In order to have a more direct evidence of current distribution at the nanoscale, we use the second current image under light, subtract the first image under dark, and by shifting images in the x and y directions, a specific area is matched exactly. Current spikes are generated due to scanning lines occurring during measurement, by eliminating the current spikes manually, we can obtain the averaged value of current in that area, and by dividing the average dark current at the same area, the averaged variation of current is derived as 0.5%, which is as small as the one obtained from current profile, and also comparable with the whole device performance for pristine graphene. Therefore, we could confirm that devices with pristine graphene show very weak photoresponse, and the current mapping by C-AFM is reflecting the true characteristics of the device rather than technical difficulties, such as a contact issue between the tip and graphene.

4.3.5 Photocurrent Mapping with Nanoscale Resolution of NaphDT Modulated Graphene

The graphene is functionalized with diazonium salt, NaphDT, and the current mapping shown in Figure 4.6(a-c) is taken under dark, light and dark conditions. The two currents at the dark condition show similar color, and the light one is brighter than both, indicating that the photocurrent is increased upon light illumination. In order to have a quantitative analysis, current line profiles are obtained for all three conditions, which shows a clearer view of the on-off phenonmenon of photocurrent. The value of current variation with regard to

original dark current is about 54.5%. An averaged value of current increment along the current profile is about 61.5%, calculated from the dotted averaged line. In order to investigate whether this local performance is same with performance of the whole device, the overall device is tested by probe station with a semiconducting parameter analyzer setup. A positive photoresponse has also been obtained; the positive variation of current density could reach as high as 60% with enough stable duration. From here, it also proves the reliability of using C-AFM to exam the local photocurrent mapping of graphene-photoresponse at localized area.

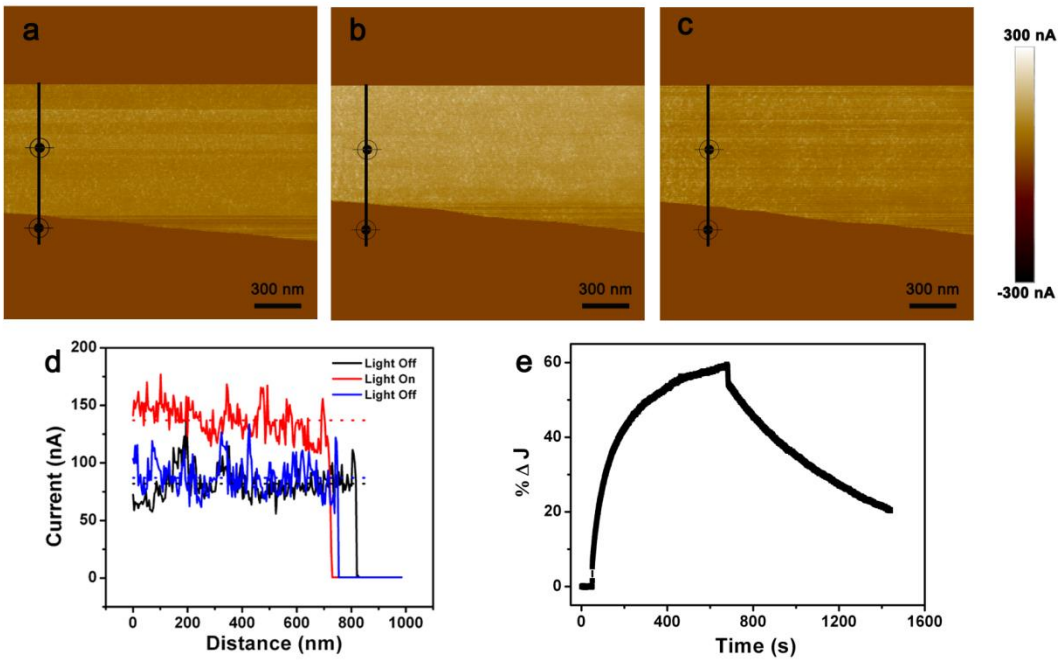

Figure 4.6 Photoresponse of NaphDT modulated graphene: a-c) Current mapping of NaphDT modulated graphene without, with and without light irradiation, respectively. d) The photocurrent profile with without and with light irradiation. The variation of current is about 54.5% with regard to the original

dark current, and the dotted line indicates the averaged current value along the line. e) The current density variation of the device performance tested by probe station and semiconducting parameter analyzer.

In order to explore the spatial correlation between photoresponse and functionalization in a straightforward way, we look the current mapping taken under light and subtracted the dark one, the subtracted image shown in Figure 4.7c. After exclusion of scanning lines and averaging process, the averaged current increment is about 54.7%. And with one more cycle, the averaged current increment with respect to dark current is about 58.2% (Figure 4.7d), which is in accordance with the profile measurement, as well as the whole device performance.

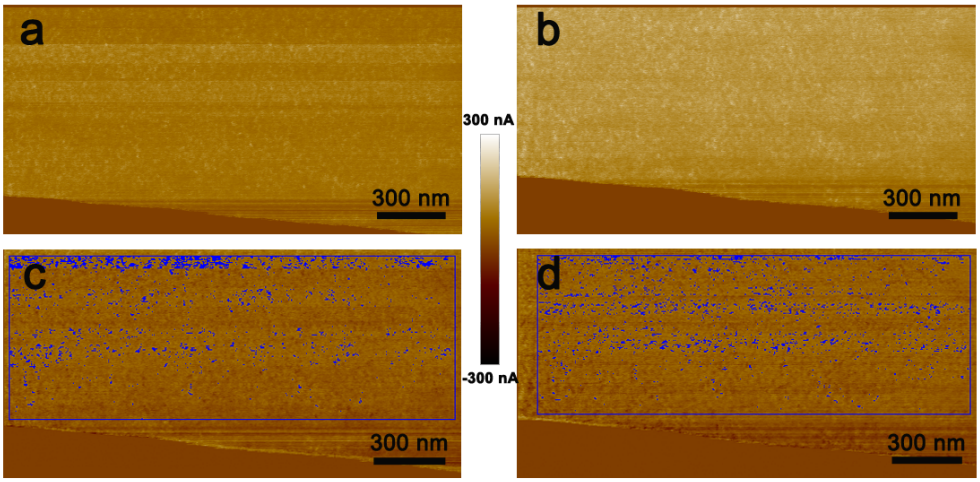

Figure 4.7 Photocurrent mapping of NaphDT modulated graphene: a) and b) The current mapping of NaphDT modulated graphene tested by C-AFM without and with light irradiation. c) Current subtraction image of photocurrent minus dark current for one cycle and another cycle d).

From the subtracted current image, we can see that they have uniform photoreponse throughout the measured area indicated by uniform current distribution. This means that every functionalized pixel (~nm^2) offers a positive photoresponse. Or in other words, the photoresponse and functionalization are correlated at nanoscale distribution. Without these localized electrical information of graphene photoresponse, we could have not concluded a uniform photoresponse is achieved from device performance alone.

4.3.6 Mechanism of Graphene-photoresponse

As previously reported,[265-266] by covalently bonding molecules on graphene, an impurity energy level is generated, that determines the band structure of graphene based devices. To confirm the role of functionalized molecules, theoretical simulation based on a simplified model of 25 benzene rings of NaphDT modified graphene (arranged in 5 × 5 rows) was built to compute the bandgap value. As seen in Figure 4.8a, a band gap of 1.25 eV is produced after NaphDT covalent bonding with grapheme, comparing with no direct bandgap can be observed in graphene before the modification.

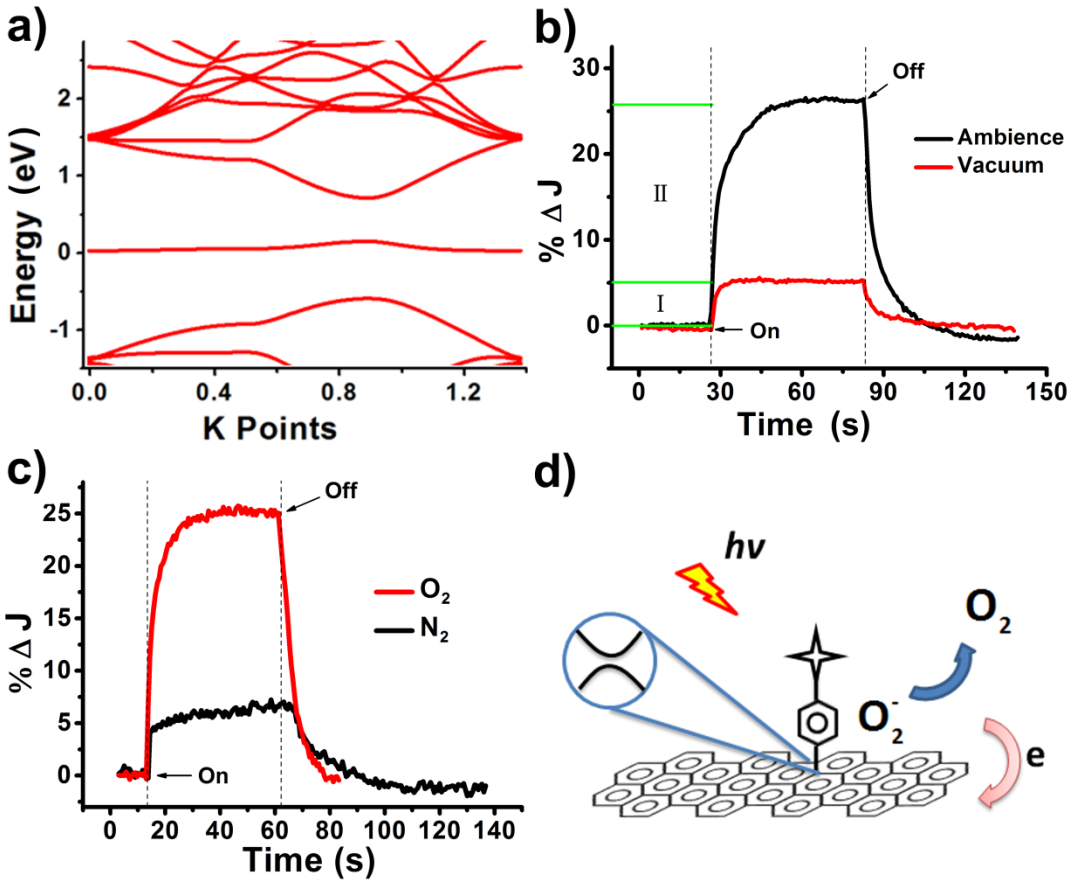

Figure 4.8 Mechanism of graphene photoresponse: (a) Band structure of NaphDT modified graphene in 5×5 graphene superlattice (b) photoreponse behaviour of the graphene device covalently functionalized with NaphDT in ambient condition (black) and vacuum condition (red) (c) photoreponse behaviour of the hybrid device in pure N_2 (1 atm) condition (black) and O_2 (1 atm) condition (red) (d) schematic illustration of bandgap opened by diazonium chemistry and charge injection of gas molecules.

In order to explore the exact role of the newly created bandgap, the photoresponse of NaphDT-graphene was studied in vacuum (1×10^{-6} torr), thereby eliminating the contribution of adsorbed gas molecules (Figure 4.8b).[267-268] Unlike

at ambient condition, the ΔJ under vacuum rapidly reached saturation by around 5.1% (stage I in Figure 4.8b), implying that the remaining 20% of the photoresponse is a result of the charge injection during the adsorption/desorption of gas molecules at ambient condition (stage II in Figure 4.8b). In order to figure out the role of the different gas molecules, the photoresponse of NaphDT-graphene was studied in pure N_2 and O_2 (Figure 4.8c). The photoreponse behavior observed under N_2 is similar as vacuum condition; also photoreponse behavior under O_2 is similar to that under ambient condition. This means that the photoreponse of chemically modified graphene is mainly contributed from the O_2 molecules under ambient condition. By volume, dry air contains 78.09% nitrogen, 20.95% oxygen,[269] therefore the N_2 has almost 4 times of O_2 in volume under ambient. According to Boyle's law[270], which describes how the pressure of a gas tends to decrease as the volume of a gas increases. Therefore, the N_2 tend to have ¼ of the O_2 pressure under ambient condition. In Figure 4.8c, it reveals that even when N_2 has the same amount of pressure as O_2 does, the photocurrent is still much lower than that of O_2. Hence, these results proved that oxygen gas molecules play a crucial role in the enhancement of photoresponse under ambient condition.

Based on the results above, we determined the mechanism of the photoresponse as follows: Initially in the dark, the adsorbed gas molecules took up the electrons from the graphene conduction channel, leading to a depletion of carrier density in the systematic conductance channel. Subsequently, when the device was exposed to light, a few of the gas molecules desorbed from graphene

and released the electrons. Since the graphene device was n-type doped after the modification, the released electrons would consequently result in an increase of carrier density and form a positive photoresponse (Figure 4.8d). Meanwhile, the bandgap formed in graphene would cause the photo-induced activation of an electron from the valence to conduction band, thereby inducing a positive photoresponse. The photoresponse phenomenon we observed could be a result of the two mechanisms.

4.4 Conclusion

In summary, graphene photoresponse was successfully obtained using an easy covalent chemical modulation strategy involving diazonium chemistry. The photoresponse performance is directly correlated with the functionalization, proven by the direct evidence from photocurrent mapping. Bandgap due to the impurities and the interaction of decorated graphene with gas molecules contributed to the large graphene-photoresponse. Most importantly, graphene with modulatable photoresponse is an ideal candidate for more practical applications such as gas sensors, photovoltaics, and photoresponse transistors.

Chapter 5 TUNABLE ELECTRICAL PROPERTIES OF FUNCTIONALIZED DENDRIMERS

In the previous chapters, what we have studied so far is all based on two dimensional structures with a large π-conjugated system. In order to explore more on the relationship between structure and properties, structures with more dimensionality are preferred. In this chapter, we demonstrated a series of π-conjugation-interrupted frameworks (CIFs) possessing real three dimensionality and its electrical properties are probed locally by C-AFM. The uniform layers of dendrimer based nanostructures self-assembled via immersion-dip method and showcased semiconductor properties. Importantly, 2.5th generations (G2.5) assembly was found to be sensitive to dopants, and post-modification of G2.5 nanostructure-based thin film with diazonium salt rendered its electrical properties highly tunable by up to two degrees of magnitude. As a result of the tunable electrical properties of CIFs, we envisage their potential role as active components of memory devices in the future.

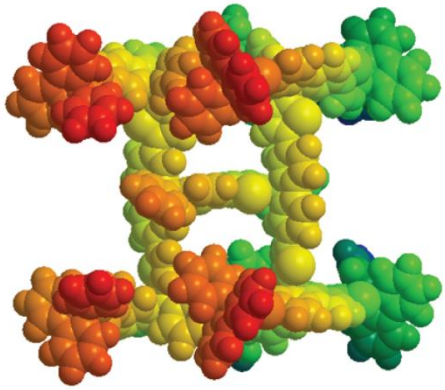

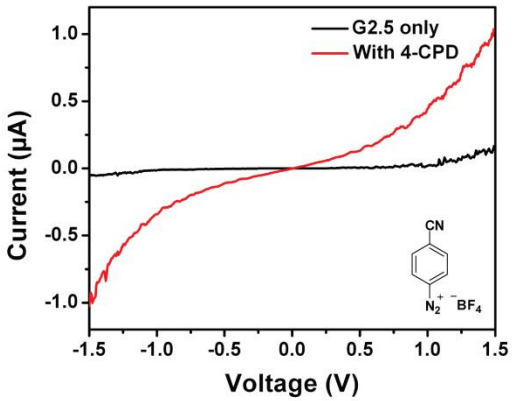

5.1 Introduction

Nanoscale semiconducting molecules are fascinating optoelectronic materials for organic electronics, and electrical properties of thin film organic electronic devices are influenced by both the materials and structures.[271-276] More recently, organic synthesis has become an alternative bottom-up approach for various other molecular nanostuctures with several advantages such as the precise control of structures and size-selectivity.[277-284] Dendrimers are a type of nanoscale semiconducting molecules which offer more degrees of freedom to adjust electronic or exciton behavior via their core, branch and periphery, as compared to linear conjugated polymers.

Desired optoelectronic properties of the dendrimers have been achieved via mechanisms such as intramolecular fluorescence resonance energy transfer (FRET), photoinduced electron transfer (PET), and built-in redox gradients amongst others.[285-290] Dendritic semiconductors have been applied in various organic devices, such as organic light emitting devices (OLEDs),[291-298] organic photovoltaics,[299-301] organic lasers,[302-303] and other applications.[304] In π-conjugation interrupted frameworks (CIFs), a class of dendrimers, the introduction of tetrahedral sp^3 carbon linkage into conjugated areas is favorable for more cubic three-dimensionality. Furthermore, its wide bandgap and large triplet energy levels make it suitable for various electronic host materials.[305-306] However, there are

currently very few examples of such bottom up synthesis and subsequent self-assembled nanostructures in the realm of organic electronics.[307-308]

In this chapter, we demonstrated a series of π-conjugation-interrupted frameworks (CIFs, G0.5-G2.5) via the iterative divergent procedure using the atom-economic C-H bond functionalization of BF_3•Et_2O-mediated Friedel-Crafts reaction at room temperature with the Pd-catalyzed Suzuki carbon-carbon cross-coupling reaction for the synthesis of nanoscale organic semiconductors. The G2.5 CIF consists of bithiophene at the core, 2,7-bithiophenyl-alkyoxyphenylfluorene as branches, and alkyoxyphenylfluorene as end-capped surfaces. The introduction of tetrahedral quaternary carbon into dendrimers can further increase the shape-persistent characteristics proved by the visualization of AM2 simulation, which have the interesting self-similar H-shaped conformations from the first generation to the 2.5^{th} generation. Due to these geometric confirmations, fascinating self-assembly behavior of semiconducting G2.5 dendrimers was observed. Post-modification of this nanostructure-based thin film enabled the tuning of its electrical properties measured by C-AFM, widening potential applications in organic electronics.

5.2 Experimental Section

5.2.1 Synthesis of π-conjugation Interrupted Dendrimers

The synthetic routes of the G0.5-G2.5 dendrimers are outlined in Scheme 1. Firstly, bithiophene, which formed the core, was obtained by the Kumada coupling reactions (i.e. a nickel-catalyzed Grignard-Wurtz cross-coupling reaction involving an arylbromide and a Grignard reagent). The dendrimers G0.5 and G0.5-Br were synthesized by the BFR of unsubstituted and substituted 9-(4-(octyloxy)phenyl)-fluoren-9-ol tertiary alcohol with bithiophene with yields of 93% and 90%, respectively. Secondly, a Suzuki cross-coupling reaction of tetrabromo-substituted G0.5-Br with the thiophene-boric acid of 4.5 equiv under the catalyst of $Pd(PPh_3)_4$ was smoothly conducted to obtain G1 at 70% yield. Similarly, the dendrimers G1.5 and G1.5-Br were synthesized by a repeated BFR with a yield of 85% and 56% respectively, and the second generation dendrimer G2 by the Suzuki cross-coupling reaction with the yield of 80%. Finally, Friedel-Crafts Reaction of G2 was conducted repeatedly to prepare the target dendrimer G2.5 with a nearly 35% yield. The designed chemical structures were confirmed by the characterization of ^{1}H and ^{13}C NMR and elemental analysis.

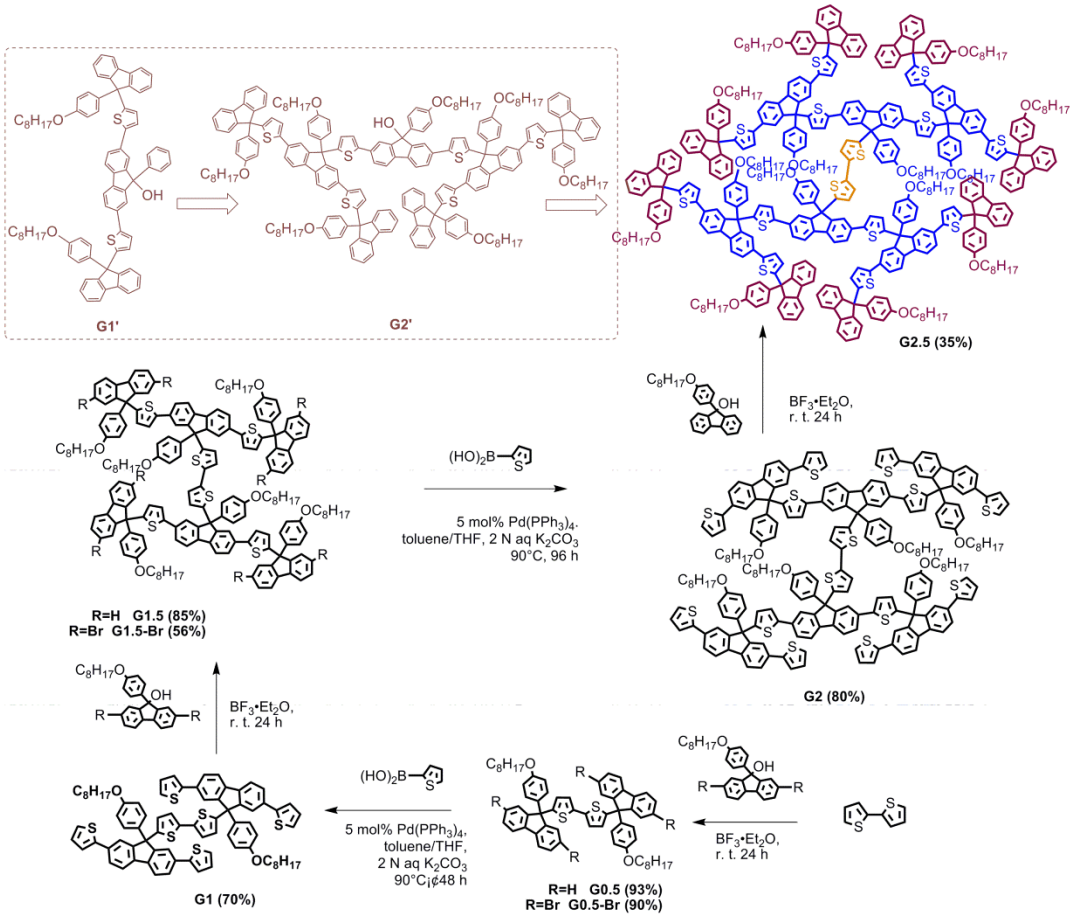

Scheme 5.1 Retrosynthetic analysis of G2.5 and its divergent synthetic route starting from G0.5 via BFR.[309] Reprinted with permission from reference 309. Copyright 2013 Wiley-VCH Verlag GmbH and Co. KGaA.

5.2.2 Synthesis of 4-Cyanophenyl Diazonium Tetrafluoroborate (4-CPD)

The reaction synthesizing 4-CPD is occurring at a cold environment, supplied by water-ice bath. The solution of sodium nitrate (45 mg, 0.65 mmol) in Milli-Q water (0.25 mL) was added slowly to 4-aminobenzonitrile (70 mg, 0.59 mmol) in 1 M HCl (1 ml). drop by drop. And then the whole reaction carried out at

about 1 ℃ for 1 hour. After that, 0.6 mL of a saturated solution of sodium tetrafluoroborate/ Milli-Q water was added. The off-white product was precipitated and then purified by several rinses with cold diethyl ether and acetonitrile. The final product of 4-CPD is in power form (57.6 mg, 45%).

5.2.3 Shape-persistent Characteristics by Visualization of AM2 Simulation

As mentioned earlier, by incorporating the tetrahedral quaternary carbon into dendrimers , it can further increase the shape-persistent characteristics proved by the visualization of AM2 simulation, (Chart 1) which have the interesting self-similar H-shaped conformations from the first generation to the 2.5th generation. The target G2.5 CIF has the size of about 1.7 nm × 3.2 nm × 1.5 nm by molecular mechanics calculations (MM2).

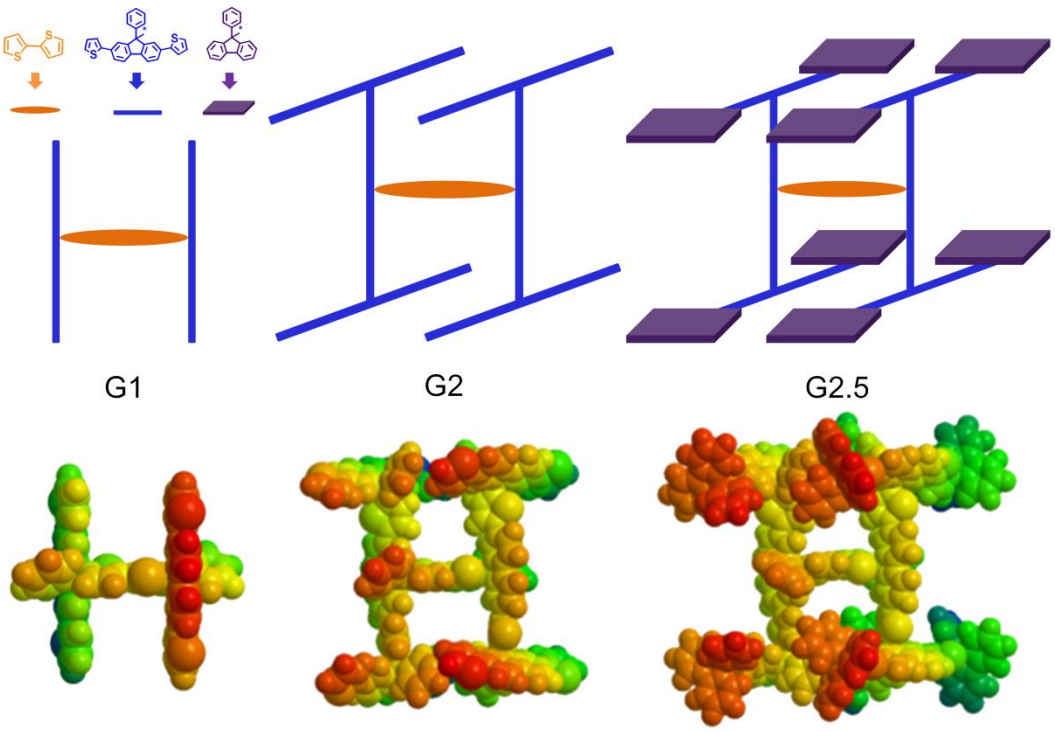

Chart 5.1 CIFs (G1-G2.5) with shape-persistent characteristics proved by the visualization of AM2 simulation.[309] Reprinted with permission from reference 309. Copyright 2013 Wiley-VCH Verlag GmbH and Co. KGaA.

5.2.4 Preparation of Self-assembled Dendrimer Nanostructures

It is well known that thiophene functional groups are able to bond with Au substrates,[310] but this is not necessarily true for all molecules with a functional group of thiophene.[311] Furthermore, the molecular geometry of G2.5 is too complicated to allow the thiophene group to be exposed at the outer layer of the molecular structure, which makes the chance of the G2.5 molecule chemically

binding with Au substrate tremendously small. Therefore, in this self-assembly process, physisorption is the main contribution. Therefore, we created our own protocol, referred to as Immersion-dip method, to form uniform structures on the Au surface. The ultraflat Au substrate was immersed into a G2.5/toluene solution with 1mg/mL concentration for 16 hours. Subsequently, the surface was dip cleaned by toluene three times, and dried. The morphology of the self-assembly was characterized by tapping mode AFM (Veeco Multimode SPM system with a NanoScope V control station).

5.3 Results and Discussion

5.3.1 Electrical Measurement with Conductive AFM

A uniformly conductive Au substrate with an ultraflat surface was required for the following reasons: firstly, for the recognition of molecular structures; secondly, a good contact of tip-molecule-substrate was required to minimize the contact resistance; lastly, to extend the lifetime of a C-AFM tip operated in contact mode, surface roughness determined the lifetime of the tip. With these considerations in mind, an ultraflat Au substrate was fabricated according to the Si/SiO_2 template stripping method.[312]

The procedures of creating such an ultraflat Au include the following four main steps: firstly, wafer and glass need to be thoroughly cleaned by piranha solution, and then the wafer is used as a template, and a layer of Au film (100nm)

is thermally evaporated on, then two component glue is prepared with a specific ratio (10:1), lastly the glass is covered with this glue and pressed onto the Au film on the wafer, after curing, the glass with the Au film is stripped from the wafer, and gives rise to an ultraflat surface. The surface is examined by C-AFM for characteristics of roughness and conductive properties. From Figure 5.1a, it can be found that the Au film is flat in the sense that less than 0.5nm root-mean-square roughness, obtained in the area of $5 \times 5\ \mu m^2$, which can be called an ultraflat film according to the literature.[313] Moreover, the electrical properties are characterized simultaneously shown in Figure 5.1b; a number of I-V curves are measured in order to prove that it reveals the electrical property of Au.

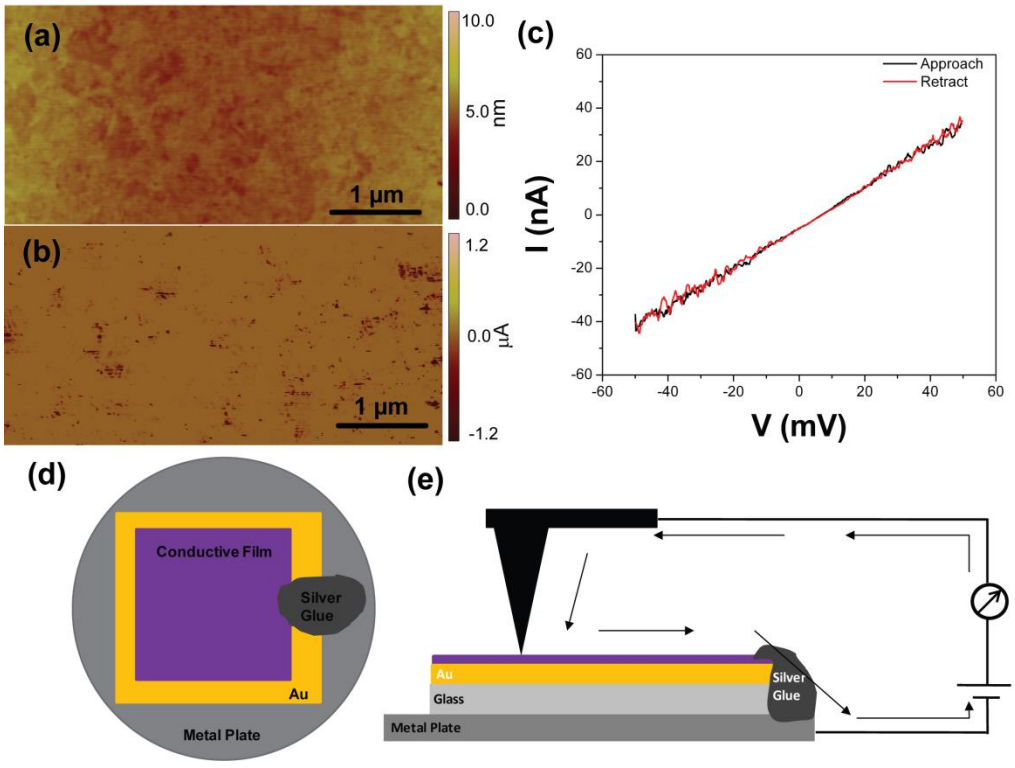

Figure 5.1 C-AFM characterization of an ultraflat Au substrate and experiment

scheme: (a) Topography image of an ultraflat Au substrate (5×2.5 μm^2), the root-mean-square roughness in the size of (5×5 μm^2) is 0.35 nm. (b) Current image obtained simultaneously of that ultraflat Au substrate (5×2.5 μm^2), the value of current flow is larger than 1.2 μA even with a small sample bias (– 6 mV). (C) A set of I-V curves, showing a linear relationship. (d) Top-view of schematic drawing for electrical analysis of CIFs thin films. (e) Side-view of schematic drawing for electrical analysis of CIFs thin films.[309] Reprinted with permission from reference 309. Copyright 2013 Wiley-VCH Verlag GmbH and Co. KGaA.

The electrical properties of G2.5 as well as post-modified G2.5 with 4-CPD were characterized using a conductive AFM system with TUNA module (Veeco Multimode SPM system with a NanoScope V control station). The probe was coated with 3nm chromium and 20 nm platinum for good conductivity, with a radius of 20 nm. Each tip was checked by scanning electron microscope (SEM) to ensure consistent tip radius and good quality of the conductive film. The conductive tip was brought into contact with G2.5 nanostructure based thin film under controlled load (~10 nN) for all experiments. The specific circuit used in the measurements is illustrated in Figure 5.1e. Statistical analysis for the measured data showed good reproducibility and reliability.

5.3.2 Electrical Analysis of G2.5 Nanostructured Assemblies

Upon the synthesis of these organic nano-frameworks with self-similar H-shaped conformation, we envisaged the creation of a new class of nanoscale semiconductors, for application in organic electronics. We fabricated G2.5 dendrimer based nanostructured thin-films on an ultraflat Au substrate, the detailed protocol is elaborated in the experimental section. C-AFM is a powerful tool to explore the current-voltage (I-V) characteristics of self-assembled monolayers,[119, 314] molecular wires,[112, 315] and thin films[316-318] etc. The morphology and electrical properties of the G2.5 nanostructure-based thin film were measured using C-AFM, its key advantage being the ability to correlate the topography and the current image simultaneously. And because of the ability of correlating topography with current images, it allows us to probe the conductive tip onto the targeted area and measured the I-V characteristics in a precise and controllable way. For instance, in the topography image, the G2.5 assemblies were observed as nanostructures with spherical shape and Au substrate were looked like the dark trench; while in the current image with applying a very small voltage bias (-6mV), current were only observable for the Au substrate. Some of the Au substrate (dark trench) is not obvious in the topography image, but negative current contrast was well presented in the current image. Therefore, when we locate the conductive probe to measure the electrical properties of G2.5 assembly, we would try to locate the probe on those assemblies away from the Au substrate (negative current contrast in current image) to avoid sudden current increment, and causing inaccurate measurement as well as burning down the conductive layer of the probe.

Both topography images and I-V measurements were carried out. From Figure 5.2a, it can be seen that the self-assembled structure of G2.5 is spherical in shape due to its dendrimeric nanostructures, which represents one molecule or an aggregate with a number of molecules. Moreover, the nanostructures were assembled in a layer-by-layer fashion, forming layers of films. I-V measurements of the film were tested using C-AFM, which showed typical semiconductor properties in Figure 5.2b. Both approach (voltage is applied from negative bias to positive bias) and retract curves (vice versa) of the I-V measurement were analyzed, indicating no hysteresis in between. 5 – 7 different locations were chosen from which to acquire I-V measurement, which were subsequently averaged. Standard methods of statistical analysis were applied to determine error bars, shown in Figure 5.2c. This also proves that the measurement was stable and reliable during the electrical characterization.

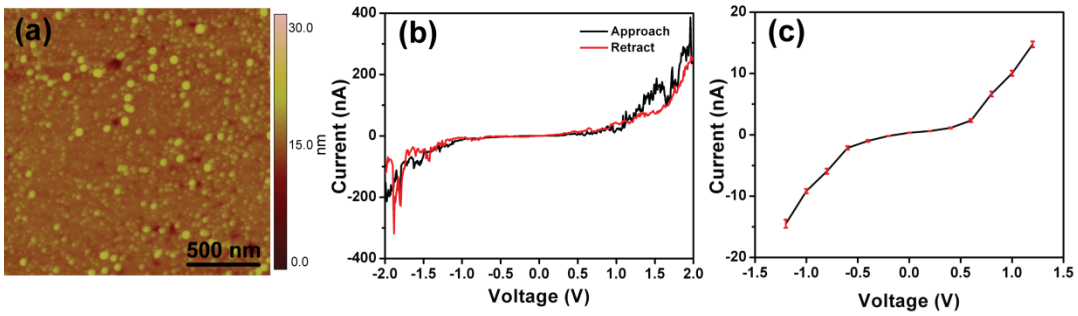

Figure 5.2 Topography and electrical properties of G2.5 assemblies on Au substrate by C-AFM: (a) Topography image of a G2.5 assemblies on Au substrate (2×2 μm^2); (b) A set of I-V curves of G2.5 assembled film (c) Sets of I-V curves with error bars indicated at selected points.[309] Reprinted with

permission from reference 309. Copyright 2013 Wiley-VCH Verlag GmbH and Co. KGaA.

5.3.3 Postfunctionalization and Characterization

So far, it has been demonstrated that G2.5 self-assembled structures are stable in air, readily soluble in common organic solvents and are semiconductors by nature. All of these properties and behaviors made it a suitable candidate for organic electronics. We were struck by the possibility of effectuating an electrically tunable material by incorporating small molecules, in particular, by decorating G2.5 based nanostructured thin film with 4-cyanophenyl diazonium (4-CPD) tetrafluoroborate. From the molecular structure of G2.5, several aryl groups were contained, and from Huang's work on using diazonium salts to decorate graphene, we learnt 4-nitrophenyl diazonium (4-NPD) tetrafluoroborate could bind aryl groups via σ-bonds. With a higher concentration of 4-NPD, the conductivity of the semiconductive surface is significantly altered.[319] Therefore, in our work, we used an excess amount of 4-CPD to react with G2.5, and both topography images and I-V measurements were conducted to examine the outcome. Following the study from Strano,[320] an Au substrate with G2.5 self-assembled film was immersed in 10 mM 4-CPD/water with 1wt% sodium dodecyl sulfate (SDS) for 10 hours, and subsequently cleaned by water with and without 1wt%SDS, and dried. As for the specific binding site of 4-CPD onto G2.5 nanostructure-based thin fil, two kinds of possibilities are considered: one possibility is to bind the aryl group,

which has shown in previous literature;[321] and the other possibility is to bind on the thiophene groups.[322]

The conductivity of G2.5 decorated with 4-CPD is much higher than G2.5 alone as shown in Figure 5.3a. Moreover, a statistical analysis was performed to demonstrate the stability and reliability of the I-V measurement for G2.5 with 4-CPD. Furthermore, AFM images have been presented in Figure 5.4, from which the difference between G2.5 alone and G2.5 with 4-CPD system, can be observed from both the topography and phase images. For both topography and phase images, the scale bar for before and after modification is the same, for a fair comparison. From topography images, the G2.5 with 4-CPD shows a layer of film covered on top of the G2.5 self-assembled aggregates, while this could even be distinguished more clearly from the phase images. Therefore, it proved the existence of 4-CPD on top of G2.5 nanostructure-based thin film. This is another direct evidence to prove the success of incorporating 4-CPD into G2.5 nanostructures besides I-V measurements. Therefore, the electrical properties can be tuned to a large extent by post-modifying the dendrimer with diazonium salt, and this widens the opportunity for this class of dendrimers to be used in the field of organic electronics.

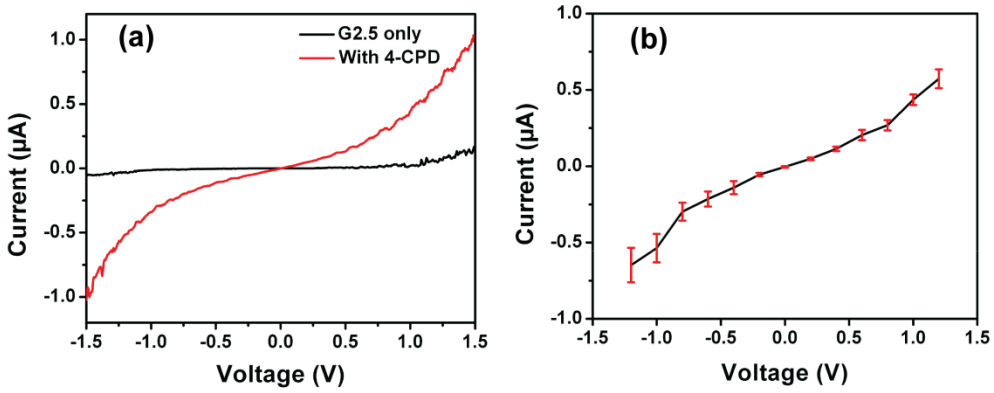

Figure 5.3 Electrical properties of G2.5 assemblies decorated with 4-CPD on Au substrate by C-AFM: (a) I-V curves of both G2.5 alone and G2.5 with diazonium salt decoration; (b) sets of I-V curves with error bars indicated at selected points.[309] Reprinted with permission from reference 309. Copyright 2013 Wiley-VCH Verlag GmbH and Co. KGaA.

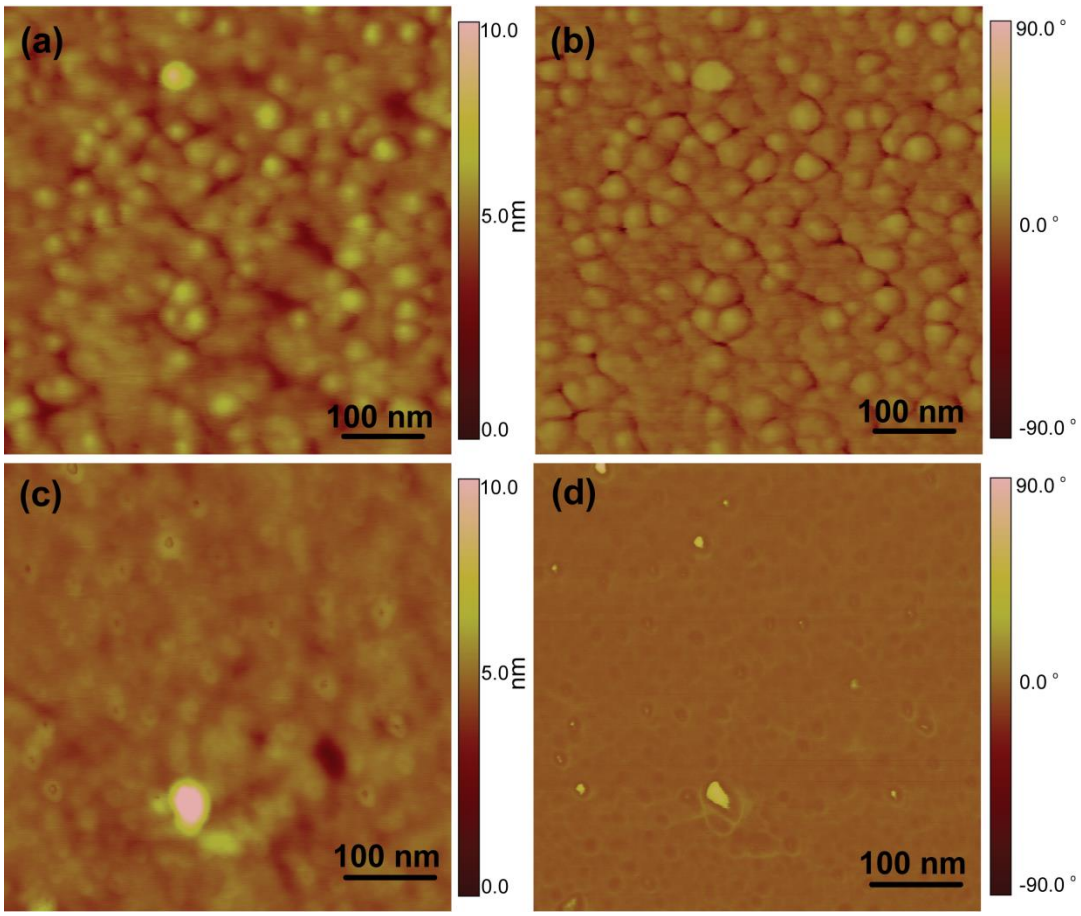

Figure 5.4 AFM topography and phase images of G2.5 before (a and b) and after post-modification with 4-CPD(c and d) respectively.[309] Reprinted with permission from reference 309. Copyright 2013 Wiley-VCH Verlag GmbH and Co. KGaA.

5.4 Conclusion

In summary, G0.5-G2.5, a series of soluble organic nanoframeworks, were synthesized with self-similar H-shaped conformations using an organic bottom-up

synthesis approach via the iterative BFR of tertiary alcohol and Suzuki C-C cross-coupling reactions. The uniform layers of G2.5 nanostructures self-assembled via the immersion-dip method and showcased semiconductor properties, measured by C-AFM. Importantly, G2.5 was found to be sensitive to dopants and post-modification of G2.5 nanostructure based thin film with a diazonium salt, rendering its electrical properties highly tunable by up to two degrees of magnitude. Hence, it has been demonstrated that the π-conjugation-interrupted frameworks and their doped counterparts broaden the options for organic electronics. As a result of the H-shaped conformation and photosensitive properties of CIFs, we envisage their potential role as active components of memory devices and photodetectors in the future.

Chapter 6 CONCLUSIONS AND RECOMMENDATIONS

In this thesis, with the aim of understanding the structural behavior and functional properties of interfacial supramolecular assemblies at different interfaces, varied molecular systems have been investigated systematically with the help of scanning probe microscopy. We have provided key and useful guidance for fabricating molecular and supramolecular electronics in the future. The main conclusions drawn from this study are outlined.

In order to form a 2D honeycomb network at solid-liquid interface, a series of HBC derivatives were designed by considering the balance among molecule-molecule, molecule-substrate and solvent-substrate interactions. Specifically, the intermolecular interaction had a great influence on the outcome of self-assembled moieties. There were two ways to build up a 2D nanoporous network: one way was achieved through intermolecular hydrogen bonding interactions for HBC-COOH as a molecular building block, and the other way was obtained via antiparallel intermolecular dipole-dipole interactions between HBC-CF_3 molecules. We demonstrate the first example showing that intermolecular dipole-dipole interactions can be used to form a 2D porous honeycomb structure. Molecular mechanics and dynamics simulations were performed to prove the detailed functional group interactions as well as the 2D superstructures. In conclusion, a delicate balance between the different substituents of the molecular building blocks

is important for engineering the interfacial supramolecular structures of HBC derivatives.

The purpose of forming such a 2D honeycomb network was to subsequently establish a host-guest. By knowing that the tricarboxylic acid molecule HBC-COOH can self-assemble into a highly porous and rigid 2D honeycomb network at a 1-phenyloctane-HOPG interface, coronene was rationally selected as a guest molecule. It was found that the coronene molecules exist in a dynamic equilibrium between free molecules in solution and trapped molecules in the 2D porous network. By having this 2D rigid porous network, it was possible to try guest molecules with electron withdrawing properties as well; therefore it opens the opportunity to establish a molecular rectifier in the future.

Although a bottom-up approach via self-assembly of π-conjugated molecules for producing such a 2D honeycomb network with sp^2 carbon atoms has been demonstrated with uniform structure and stability, its ability to fabricate those structures into devices remains a challenge due to the liquid environment involved, and it would be even more difficult to functionalize the self-assembled structure for multipurpose device performance. Therefore, a top-down approach to fabricate such a 2D structure was used via exfoliation of graphite, and a solid-state material graphene with perfect 2D honeycomb structure was selected to be the target material. We have proved that graphene photoresponse was successfully obtained using an easy covalent chemical modulation strategy involving diazonium

chemistry. And the photocurrent mapping by using C-AFM has revealed the correlation between homogeneous functionalization and uniform photoresponse of chemically modulated graphene. The mechanism for the photoresponse was due to the interaction of modulated graphene with gas molecules. Most importantly, graphene with modulatable photoresponse is an ideal candidate for more practical applications such as gas sensors, photovoltaics, and photoresponse transistors.

The two-dimensional large π-conjugated system promoted electron transfer from an electronic point of view, while π-conjugation-interrupted dendrimers offered more degrees of freedom both with respect to assembly behavior and electrical properties. Therefore, a series of soluble organic nanoframeworks was synthesized with self-similar H-shaped conformations using organic bottom-up synthesis approach, and the uniform layers of G2.5 nanostructures self-assembled via an immersion-dip method and showcased semiconductor properties, measured by C-AFM. Importantly, G2.5 was found to be sensitive to dopants and post-modification of G2.5 nanostructure based thin film with diazonium salts, rendering its electrical properties highly tunable by up to two degrees of magnitude. Hence, it has been demonstrated that the π-conjugation-interrupted frameworks and their doped counterparts broaden the options for organic electronics. As a result, we envisage their potential role as active components of memory devices and photodetectors in the future.

In conclusion, self-assembly of π-conjugated molecules was conducted at the solid-liquid interface for the purpose of establishing a host-guest system. Graphene was considered as basic building blocks for 2D nanocarbons, and chemically modulated graphene with stable and uniform photoresponse was demonstrated by photocurrent mapping. Last but not least, π-conjugation-interrupted frameworks revealed tunable electrical properties upon dopant decoration. Overall, this study has provided key and useful guidance toward the development of molecular and supramolecular electronics, by correlating the structural behavior and functional properties of different molecular systems at different interfaces.

Recommendation for Future Work

We have demonstrated that current mapping and I-V characteristics of targeted materials were obtained by using C-AFM at the solid-vapor interface, and the structure of the targeted material was at two-dimensional level. Up to now, with the development of molecular electronics, more and more advanced techniques and tools are required to understand fundamental phenomenon at single molecular or single atomic level. For instance, conductance of single molecule has been measured via STM break junction technique,[179] but the measured results are inconsistent from one research group to another, which is due to the unclear molecular conformation of molecules between the metal junctions. Therefore, from a more fundamental point of view, we would like to recommend visualizing

molecular conformational change with respect to bias variation. In order to achieve that, different technique may be required, such as transmission electron microscopy, fluorescence microscopy, Raman spectroscopy and of course the families of scanning probe microscopy.

Both the structural behavior and functional properties of molecular systems in this study used one technique at a time, either by using scanning tunneling microscopy to investigate the self-assembly behavior of HBC derivatives, or by using conductive-AFM to understand the photoresponse of chemically modulated graphene. In the next generation of SPM development, more probes will be recommended to be integrated in one system, and more functional properties could be probed simultaneously, such as the multiple-probe scanning probe microscope developed recently.[323-324]

Beyond the integrated multiple-probe SPM, the testing environment should also be well controlled in the future, for instance, the local characterization of battery performance could be measured by SPM techniques to fundamentally understand the charging and discharging process at a nano or even molecular scale. One of the problems causing shortening battery life is due to strain developed during intercalation and electrochemical reactions.[107] One could apply an alternating current (AC) bias on the sample to obtain oscillatory surface displacement, which is detectable by an SPM tip. Moreover, the amplitude of this oscillation reflects the Li-ion transport, so that it is possible to probe the Li-ion

flow locally and determine the origin of battery failure. It is also recommended to integrate SPM with other techniques, especially those good at obtaining chemical information of materials, such as Raman spectroscopy, so that a set of complementary tools will be utilized to their full potential.

LIST OF PUBLICATIONS

1. **Shao, Q.**; Niu, Z.; Hirtz, M.; Jiang, L.; Liu, Y.; Wang, Z.; Chen, X.* "High-performance and Tailorable Pressure Sensor Based on Ultrathin Conductive Polymer Film" *Small*, **2013**, *9*, smll.201303601.

2. Chang, Y.-Z.[⊥]; **Shao, Q.**[⊥]; Bai, L.-Y.; Ou, C.-J.; Lin, J.-Y.; Xie, L.-H.;* Liu, Z.-D.; Chen, X.;* Zhang, G.-W.; Huang, W.* "Bottom-up Synthesis of Nanoscale Conjugation-Interrupted Frameworks and Their Electrical Properties" *Small* **2013**, *9*, doi:10.1002/smll.201300065.

3. Mu, Z.[⊥]; **Shao, Q.**[⊥]; Ye, J.; Zeng, Z.; Zhao, Y.; Hng, H. H.; Boey, F. Y. C.; Wu, J.;* Chen, X.* "Effect of intermolecular dipole-dipole interactions on interfacial supramolecular structures of C3-symmetric hexa-peri-hexabenzocoronene derivatives" *Langmuir* **2011**, *27*, 1314-1318.

4. Niu, Z.; Luan, P.; **Shao, Q.**; Dong, H,; Li, J.; Chen, J.; Zhao, D.; Cai, L.; Zhou, W.;* Chen, X.;* Xie, S. "A "Skeleton/Skin" Strategy for Preparing Ultrathin Free-Standing Single-Walled Carbon Nanotube/Polyaniline Films for High Performance Supercapacitor Electrodes" *Energy Environ. Sci.* **2012**, *5*, 8726-8733.

5. Du, J.; **Shao, Q.**; Yin, S.; Jiang, L.; Ma, J.; Chen, X.* "Colorimetric Chemodosimeter Based on Diazonium-Gold Nanoparticle Complexes for Sulfite Ion Detection in Solution" *Small* **2012**, *8*, 3412-3416.

6. Du, J.; Jiang, L.; **Shao, Q.**; Liu, X.; Ma, J.; Chen, X.* "Colorimetric Detection of Mercury Ion Based on Plasmonic Nanoparticles" *Small* **2012**, *8*, doi:10.1002/smll.201200811.

7. Meng, F.; Hervault, Y.-M.; **Shao, Q.**; Hu, B.; Norel, L.; Rigaut, S.; Chen, X.* "Orthogonally Modulated Molecular Transport Junctions for Resettable Electronic Logic Gates", *Nat. Commun.* **2013**, *4*, 3023, doi: 10.1038/ncomms4023.

8. Zheng, K.; Du, J.; Zhou, Y. –C.; **Shao, Q.**; Hng, H. H.; Zhang H. –L.*; Chen, X.* "Modulating Graphene Photoresponse by Surface Chemistry", in preparation.

9. Liu, L.; Niu, Z.; **Shao, Q.**; Chen, X.* "Chemically Modified Reduced Graphene Oxide Foam for High-performance Supercapacitors", in preparation.

10. Niu, Z.; Liu, L.; Zhang, L.; Zhu, B.; **Shao, Q.**; Dong, H.; Zhou, W.; Chen, X.*; Xie, S. "A Universal Strategy to Prepare Functional Porous Graphene Hybrid Architectures", in preparation.

11. **Shao, Q.**; Mu, Z.; Ye, J.; Zeng, Z.; Zhao, Y.; Wu, J.;* Chen, X.* "Effect of intermolecular interactions on interfacial supramolecular structures of C_3-symmetric hexa-peri-hexabenzocoronene derivatives" *ICMAT 2011 K-PO2-10* Poster Presentation

$^{\perp}$ These authors contributed equally to this work.

REFERENCES

[1] J.-M. Lehn, M. Mascal, A. Decian, J. Fischer, *Journal of the Chemical Society, Chemical Communications* **1990**, 479-481.

[2] C. T. Seto, G. M. Whitesides, *Journal of the American Chemical Society* **1990**, *112*, 6409-6411.

[3] J. A. Zerkowski, C. T. Seto, D. A. Wierda, G. M. Whitesides, *Journal of the American Chemical Society* **1990**, *112*, 9025-9026.

[4] J. A. Zerkowski, J. P. Mathias, G. M. Whitesides, *Journal of the American Chemical Society* **1994**, *116*, 4305-4315.

[5] M. Fujita, S. Nagao, K. Ogura, *Journal of the American Chemical Society* **1995**, *117*, 1649-1650.

[6] F. Zeng, S. C. Zimmerman, *Chemical Reviews* **1997**, *97*, 1681-1712.

[7] M. Fujita, S.-Y. Yu, T. Kusukawa, H. Funaki, K. Ogura, K. Yamaguchi, *Angewandte Chemie International Edition* **1998**, *37*, 2082-2085.

[8] S. Hiraoka, M. Fujita, *Journal of the American Chemical Society* **1999**, *121*, 10239-10240.

[9] B. Olenyuk, M. D. Levin, J. A. Whiteford, J. E. Shield, P. J. Stang, *Journal of the American Chemical Society* **1999**, *121*, 10434-10435.

[10] L. Brunsveld, B. J. B. Folmer, E. W. Meijer, R. P. Sijbesma, *Chemical Reviews* **2001**, *101*, 4071-4098.

[11] H. Fenniri, P. Mathivanan, K. L. Vidale, D. M. Sherman, K. Hallenga, K. V. Wood, J. G. Stowell, *Journal of the American Chemical Society* **2001**, *123*, 3854-3855.

[12] H. A. Klok, S. Lecommandoux, *Advanced Materials* **2001**, *13*, 1217-1229.

[13] H. Fenniri, B.-L. Deng, A. E. Ribbe, *Journal of the American Chemical Society* **2002**, *124*, 11064-11072.

[14] J. M. C. A. Kerckhoffs, F. W. B. van Leeuwen, A. L. Spek, H. Kooijman, M. Crego-Calama, D. N. Reinhoudt, *Angewandte Chemie International Edition* **2003**, *42*, 5717-5722.

[15] M. Schmittel, V. Kalsani, in *Functional Molecular Nanostructures, Vol. 245* (Ed.: A. D. Schlüter), Springer Berlin Heidelberg, **2005**, pp. 1-53.

[16] A. J. Wilson, *Annual Reports Section "B" (Organic Chemistry)* **2007**, *103*, 174-192.

[17] Y. Wang, H. Xu, X. Zhang, *Advanced Materials* **2009**, *21*, 2849-2864.

[18] S. S. Babu, H. Mohwald, T. Nakanishi, *Chemical Society Reviews* **2010**, *39*, 4021-4035.

[19] M. Suzuki, K. Hanabusa, *Chemical Society Reviews* **2010**, *39*, 455-463.

[20] R. Chakrabarty, P. S. Mukherjee, P. J. Stang, *Chemical Reviews* **2011**, *111*, 6810-6918.

[21] G. Chen, M. Jiang, *Chemical Society Reviews* **2011**, *40*, 2254-2266.

[22] K. Müllen, J. P. Rabe, *Accounts of Chemical Research* **2008**, *41*, 511-520.

[23] J. Wu, W. Pisula, K. Müllen, *Chemical Reviews* **2007**, *107*, 718-747.

[24] F. Jäckel, M. D. Watson, K. Müllen, J. P. Rabe, *Physical Review Letters* **2004**, *92*.
[25] M. D. Watson, F. Jackel, N. Severin, J. P. Rabe, K. Müllen, *Journal of the American Chemical Society* **2004**, *126*, 1402-1407.
[26] T. Böhme, C. D. Simpson, K. Müllen, J. P. Rabe, *Chemistry – A European Journal* **2007**, *13*, 7349-7357.
[27] A. Ciesielski, C.-A. Palma, M. Bonini, P. Samorì, *Advanced Materials* **2010**, *22*, 3506-3520.
[28] J. A. A. W. Elemans, S. De Feyter, *Soft Matter* **2009**, *5*, 721-735.
[29] D. González-Rodríguez, A. P. H. J. Schenning, *Chem. Mat.* **2010**, *23*, 310-325.
[30] S. Müller, K. Müllen, *Philosophical Transactions of the Royal Society A: Mathematical, Physical and Engineering Sciences* **2007**, *365*, 1453-1472.
[31] M. M. S. Abdel-Mottaleb, E. Gomar-Nadal, S. De Feyter, M. Zdanowska, J. Veciana, C. Rovira, D. B. Amabilino, F. C. De Schryver, *Nano Letters* **2003**, *3*, 1375-1378.
[32] J. M. Lehn, in *Design and Synthesis of Organic Molecules Based on Molecular Recognition* (Ed.: G. Binst), Springer Berlin Heidelberg, **1986**, pp. 173-184.
[33] J. M. Lehn, *Pure and Applied Chemistry* **1978**, *50*, 871-892.
[34] J.-M. Lehn, in *Alkali Metal Complexes with Organic Ligands, Vol. 16*, Springer Berlin Heidelberg, **1973**, pp. 1-69.
[35] M. D. Pluth, K. N. Raymond, *Chemical Society Reviews* **2007**, *36*, 161-171.
[36] P. M. Proulx-Curry, N. D. Chasteen, *Coordination Chemistry Reviews* **1995**, *144*, 347-368.
[37] A. Ranganathan, V. R. Pedireddi, C. N. R. Rao, *Journal of the American Chemical Society* **1999**, *121*, 1752-1753.
[38] L. J. Prins, D. N. Reinhoudt, P. Timmerman, *Angewandte Chemie International Edition* **2001**, *40*, 2382-2426.
[39] J.-M. Lehn, *Science* **2002**, *295*, 2400-2403.
[40] V. Percec, M. Glodde, G. Johansson, V. S. K. Balagurusamy, P. A. Heiney, *Angewandte Chemie International Edition* **2003**, *42*, 4338-4342.
[41] M. Lackinger, S. Griessl, W. M. Heckl, M. Hietschold, G. W. Flynn, *Langmuir* **2005**, *21*, 4984-4988.
[42] L. Kampschulte, M. Lackinger, A.-K. Maier, R. S. K. Kishore, S. Griessl, M. Schmittel, W. M. Heckl, *The Journal of Physical Chemistry B* **2006**, *110*, 10829-10836.
[43] S. Lei, K. Tahara, F. C. De Schryver, M. Van der Auweraer, Y. Tobe, S. De Feyter, *Angewandte Chemie International Edition* **2008**, *47*, 2964-2968.
[44] M. Stöhr, M. Wahl, C. H. Galka, T. Riehm, T. A. Jung, L. H. Gade, *Angewandte Chemie International Edition* **2005**, *44*, 7394-7398.
[45] S. De Feyter, F. C. De Schryver, *Chemical Society Reviews* **2003**, *32*, 139-150.
[46] G. Binnig, H. Rohrer, C. Gerber, E. Weibel, *Physical Review Letters* **1982**, *49*, 57-61.

[47] G. Binnig, H. Rohrer, C. Gerber, E. Weibel, *Applied Physics Letters* **1982**, *40*, 178-180.
[48] G. Binnig, H. Rohrer, *Reviews of Modern Physics* **1987**, *59*, 615-625.
[49] G. Binnig, H. Rohrer, *Reviews of Modern Physics* **1999**, *71*, S324-S330.
[50] C. J. Chen, *Introduction to Scanning Tunneling Microscopy: Second Edition*, Oxford University Press, Oxford **2007**.
[51] N. Yao, Z. Wang, *Handbook of Microscopy for Nanotechnology* Springer **2005**.
[52] O. Ivasenko, J. M. MacLeod, K. Y. Chernichenko, E. S. Balenkova, R. V. Shpanchenko, V. G. Nenajdenko, F. Rosei, D. F. Perepichka, *Chemical Communications* **2009**, 1192-1194.
[53] A. LIanes-Pallas, C.-A. Palma, L. Piot, A. Belbakra, A. Listorti, M. Prato, P. Samori, N. Armaroli, D. Bonifazi, *Journal of the American Chemical Society* **2009**, *131*, 509-520.
[54] G. Binnig, H. Rohrer, C. Gerber, E. Weibel, *Physical Review Letters* **1983**, *50*, 120-123.
[55] L. Pleth Nielsen, F. Besenbacher, I. Stensgaard, E. Laegsgaard, C. Engdahl, P. Stoltze, K. W. Jacobsen, J. K. Nørskov, *Physical Review Letters* **1993**, *71*, 754-757.
[56] F. Besenbacher, I. Chorkendorff, B. S. Clausen, B. Hammer, A. M. Molenbroek, J. K. Nørskov, I. Stensgaard, *Science* **1998**, *279*, 1913-1915.
[57] S. Helveg, J. V. Lauritsen, E. Lægsgaard, I. Stensgaard, J. K. Nørskov, B. S. Clausen, H. Topsøe, F. Besenbacher, *Physical Review Letters* **2000**, *84*, 951-954.
[58] J. V. Lauritsen, M. Nyberg, R. T. Vang, M. V. Bollinger, B. S. Clausen, H. Topsøe, K. W. Jacobsen, E. Lægsgaard, J. K. Nørskov, F. Besenbacher, *Nanotechnology* **2003**, *14*, 385.
[59] G. Capellini, M. De Seta, C. Spinella, F. Evangelisti, *Applied Physics Letters* **2003**, *82*, 1772-1774.
[60] R. Otero, Y. Naitoh, F. Rosei, P. Jiang, P. Thostrup, A. Gourdon, E. Lægsgaard, I. Stensgaard, C. Joachim, F. Besenbacher, *Angewandte Chemie International Edition* **2004**, *43*, 2092-2095.
[61] F. Rosei, M. Schunack, P. Jiang, A. Gourdon, E. Lægsgaard, I. Stensgaard, C. Joachim, F. Besenbacher, *Science* **2002**, *296*, 328-331.
[62] J. W. Lyding, T. C. Shen, J. S. Hubacek, J. R. Tucker, G. C. Abeln, *Applied Physics Letters* **1994**, *64*, 2010-2012.
[63] J. A. STROSCIO, D. M. EIGLER, *Science* **1991**, *254*, 1319-1326.
[64] P. Zeppenfeld, C. P. Lutz, D. M. Eigler, *Ultramicroscopy* **1992**, *42–44, Part 1*, 128-133.
[65] G. Meyer, S. Zöphel, K.-H. Rieder, *Physical Review Letters* **1996**, *77*, 2113-2116.
[66] L. Bartels, G. Meyer, K. H. Rieder, *Applied Physics Letters* **1997**, *71*, 213-215.
[67] L. Bartels, G. Meyer, K. H. Rieder, *Physical Review Letters* **1997**, *79*, 697-700.

[68] G. Meyer, L. Bartels, S. Zöphel, E. Henze, K.-H. Rieder, *Physical Review Letters* **1997**, *78*, 1512-1515.
[69] L. Bartels, G. Meyer, K. H. Rieder, D. Velic, E. Knoesel, A. Hotzel, M. Wolf, G. Ertl, *Physical Review Letters* **1998**, *80*, 2004-2007.
[70] D. M. Eigler, C. P. Lutz, W. E. Rudge, *Nature* **1991**, *352*, 600-603.
[71] D. M. Eigler, E. K. Schweizer, *Nature* **1990**, *344*, 524-526.
[72] P. Avouris, *Accounts of Chemical Research* **1994**, *27*, 159-165.
[73] Y. J. Song, S. C. Erwin, G. M. Rutter, P. N. First, N. B. Zhitenev, J. A. Stroscio, *Nano Letters* **2009**, *9*, 4333-4337.
[74] R. Nishitani, H. Liu, H. Iwasaki, *Applied Physics Letters***2012**, *100*, 051102-051104.
[75] A. Ulman, *Chemical Reviews* **1996**, *96*, 1533-1554.
[76] Z. J. Donhauser, D. W. Price, J. M. Tour, P. S. Weiss, *Journal of the American Chemical Society* **2003**, *125*, 11462-11463.
[77] R. Sonnenfeld, P. K. Hansma, *Science* **1986**, *232*, 211-213.
[78] R. Sonnenfeld, J. Schneir, P. K. Hansma, *Modern Aspects of Electrochemistry* **1990**, *21*, 1-28.
[79] K. Itaya, E. Tomita, *Surface Science* **1988**, *201*, L507-L512.
[80] J. Zhang, Q. Chi, J. U. Nielsen, E. P. Friis, J. E. T. Andersen, J. Ulstrup, *Langmuir* **2000**, *16*, 7229-7237.
[81] D. M. Kolb, *Angewandte Chemie International Edition* **2001**, *40*, 1162-1181.
[82] D. M. Kolb, R. Ullmann, T. Will, *Science* **1997**, *275*, 1097-1099.
[83] X.-S. Zhou, L. Liu, P. Fortgang, A.-S. Lefevre, A. Serra-Muns, N. Raouafi, C. Amatore, B.-W. Mao, E. Maisonhaute, B. Schöllhorn, *Journal of the American Chemical Society* **2011**, *133*, 7509-7516.
[84] L.-J. Wan, *Accounts of Chemical Research* **2006**, *39*, 334-342.
[85] J. M. Artés, I. Díez-Pérez, F. Sanz, P. Gorostiza, *ACS Nano* **2011**, *5*, 2060-2066.
[86] S. Chang, S. Huang, J. He, F. Liang, P. Zhang, S. Li, X. Chen, O. Sankey, S. Lindsay, *Nano Letters* **2010**, *10*, 1070-1075.
[87] Z. Matharu, A. J. Bandodkar, V. Gupta, B. D. Malhotra, *Chemical Society Reviews* **2012**, *41*.
[88] S. Huang, J. He, S. Chang, P. Zhang, F. Liang, S. Li, M. Tuchband, A. Fuhrmann, R. Ros, S. Lindsay, *Nature Nanotechnology* **2010**, *5*, 868-873.
[89] M. Tsutsui, M. Taniguchi, K. Yokota, T. Kawai, *Nature Nanotechnology* **2010**, *5*, 286-290.
[90] H. Sakaguchi, H. Matsumura, H. Gong, *Nature Materials* **2004**, *3*, 551-557.
[91] G. Binnig, C. F. Quate, C. Gerber, *Phys. Rev. Lett.* **1986**, *56*, 930-933.
[92] J. A. A. W. Elemans, I. De Cat, H. Xu, S. De Feyter, *Chemical Society Reviews* **2009**, *38*, 722-736.
[93] T. Kudernac, S. Lei, J. A. A. W. Elemans, S. De Feyter, *Chemical Society Reviews* **2009**, *38*, 402-421.
[94] J. A. A. W. Elemans, S. Lei, S. D. Feyter, *Angewandte Chemie International Edition* **2009**, *48*, 7298-7332.

[95] M. nakamura, H. Yanagisawa, S. Kuratani, M. Lizuka, K. Kudo, *Thin Solid Films* **2003**, *438-439*, 360-364.
[96] G. Cheng, P. F. Siles, F. Bi, C. Cen, D. F. Bogorin, C. W. Bark, C. M. Folkman, J.-W. Park, C.-B. Eom, G. Medeiros-Ribeiro, J. Levy, *Nature Nanotechnology* **2011**, *6*, 343-347.
[97] M. E. Greene, C. R. Kinser, D. E. Kramer, L. S. C. Pingree, M. C. Hersam, *Microscopy Research and Technique* **2004**, *64*, 415-434.
[98] L. Schmidt-Mende, A. Fechtenkötter, M. K, E. Moons, R. H. Friend, J. D. MacKenzie, *Science* **2001**, *293*, 1119-1122.
[99] A. Bensimon, A. Simon, A. Chiffaudel, V. Croquette, F. Heslot, D. Bensimon, *Science* **1994**, *265*, 2096-2098.
[100] J. Hu, M. Wang, H. U. G. Weier, P. Frantz, W. Kolbe, D. F. Ogletree, M. Salmeron, *Langmuir* **1996**, *12*, 1697-1700.
[101] N. H. Thomson, S. Kasas, Smith, H. G. Hansma, P. K. Hansma, *Langmuir* **1996**, *12*, 5905-5908.
[102] B. S. Li, B. D. Sattin, M. C. Goh, *Nano Letters* **2006**, *6*, 1474-1478.
[103] B. A. Ashcroft, Q. Spadola, S. Qamar, P. Zhang, G. Kada, R. Bension, S. Lindsay, *Small* **2008**, *4*, 1468-1475.
[104] D. Kim, N.-K. Chung, J. S. Kim, J. W. Park, *Soft Matter* **2010**, *6*, 3979-3984.
[105] M. Leitner, N. Mitchell, M. Kastner, R. Schlapak, H. J. Gruber, P. Hinterdorfer, S. Howorka, A. Ebner, *ACS Nano* **2011**, *5*, 7048-7054.
[106] D. M. Eigler, F. K. Schweizer, *Nature* **1990**, *344*, 524-526.
[107] S. V. Kalinin, N. Balke, *Advanced Materials* **2010**, *22*, E193-E209.
[108] J. Gutierrez, A. Tercjak, I. Mondragon, *Journal of the American Chemical Society* **2010**, *132*, 873-878.
[109] L. Luo, C. D. Frisbie, *Journal of the American Chemical Society* **2010**, *132*, 8854-8855.
[110] S. H. Choi, C. Risko, M. C. R. Delgado, B. Kim, J.-L. Brédas, C. D. Frisbie, *Journal of the American Chemical Society* **2010**, *132*, 4358-4368.
[111] S. H. Choi, C. D. Frisbie, *Journal of the American Chemical Society* **2010**, *132*, 16191-16201.
[112] S. Ho Choi, B. Kim, C. D. Frisbie, *Science* **2008**, *320*, 1482-1486.
[113] M. Wanunu, A. Vaskevich, S. R. Cohen, H. Cohen, R. Arad-Yellin, A. Shanzer, I. Rubinstein, *Journal of the American Chemical Society* **2005**, *127*, 17877-17887.
[114] A. V. Tivanski, G. C. Walker, *Journal of the American Chemical Society* **2005**, *127*, 7647-7653.
[115] C. Chu, J.-S. Na, G. N. Parsons, *Journal of the American Chemical Society* **2007**, *129*, 2287-2296.
[116] N. E. Sosa, C. Chen, J. Liu, S. Xie, T. J. Marks, M. C. Hersam, *Journal of the American Chemical Society* **2010**, *132*, 7347-7354.
[117] J. M. Mativetsky, E. Treossi, E. Orgiu, M. Melucci, G. P. Veronese, P. Samorì, V. Palermo, *Journal of the American Chemical Society* **2010**, *132*, 14130-14136.

[118] Z. Wei, D. Wang, S. Kim, S.-Y. Kim, Y. Hu, M. K. Yakes, A. R. Laracuente, Z. Dai, S. R. Marder, C. Berger, W. P. King, W. A. de Heer, P. E. Sheehan, E. Riedo, *Science* **2010**, *328*, 1373-1376.
[119] X. D. Cui, A. Primak, X. Zarate, J. Tomfohr, O. F. Sankey, A. L. Moore, T. A. Moore, D. Gust, G. Harris, S. M. Lindsay, *Science* **2001**, *294*, 571-574.
[120] D. S. Seferos, A. S. Blum, J. G. Kushmerick, G. C. Bazan, *Journal of the American Chemical Society* **2006**, *128*, 11260-11267.
[121] S. De Feyter, F. C. De Schryver, *Journal of Physical Chemistry B* **2005**, *109*, 4290-4302.
[122] K. Tahara, S. Lei, D. Mossinger, H. Kozuma, K. Inukai, M. Van der Auweraer, F. C. De Schryver, S. Hoger, Y. Tobe, S. De Feyter, *Chemical Communications* **2008**, *0*, 3897-3899.
[123] D. Mössinger, J. Hornung, S. Lei, S. De Feyter, S. Höger, *Angewandte Chemie International Edition* **2007**, *46*, 6802-6806.
[124] M. Fischer, G. Lieser, A. Rapp, I. Schnell, W. Mamdouh, S. De Feyter, F. C. De Schryver, S. Höger, *Journal of the American Chemical Society* **2003**, *126*, 214-222.
[125] K. Tahara, S. Lei, W. Mamdouh, Y. Yamaguchi, T. Ichikawa, H. Uji-i, M. Sonoda, K. Hirose, F. C. De Schryver, S. De Feyter, Y. Tobe, *Journal of the American Chemical Society* **2008**, *130*, 6666-6667.
[126] S. J. H. Griessl, M. Lackinger, F. Jamitzky, T. Markert, M. Hietschold, W. M. Heckl, *Langmuir* **2004**, *20*, 9403-9407.
[127] S.-S. Li, B. H. Northrop, Q.-H. Yuan, L.-J. Wan, P. J. Stang, *Accounts of Chemical Research* **2008**, *42*, 249-259.
[128] S. De Feyter, F. C. De Schryver, *The Journal of Physical Chemistry B* **2005**, *109*, 4290-4302.
[129] K. Tahara, S. Furukawa, H. Uji-i, T. Uchino, T. Ichikawa, J. Zhang, W. Mamdouh, M. Sonoda, F. C. De Schryver, S. De Feyter, Y. Tobe, *Journal of the American Chemical Society* **2006**, *128*, 16613-16625.
[130] S. Lei, K. Tahara, X. Feng, S. Furukawa, F. C. De Schryver, K. Müllen, Y. Tobe, S. De Feyter, *Journal of the American Chemical Society* **2008**, *130*, 7119-7129.
[131] S. Furukawa, H. Uji-i, K. Tahara, T. Ichikawa, M. Sonoda, F. C. De Schryver, Y. Tobe, S. De Feyter, *Journal of the American Chemical Society* **2006**, *128*, 3502-3503.
[132] X. Cheng, A. Ver Heyen, W. Mamdouh, H. Uji-i, F. De Schryver, S. Höger, S. De Feyter, *Langmuir* **2006**, *23*, 1281-1286.
[133] X. Chen, S. Lenhert, M. Hirtz, N. Lu, H. Fuchs, L. Chi, *Accounts of Chemical Research* **2007**, *40*, 393-401.
[134] S.-S. Li, B. H. Northrop, Q.-H. Yuan, L.-J. Wan, P. J. Stang, *Accounts of Chemical Research* **2009**, *42*, 249-259.
[135] L.-J. Wan, *Accounts of Chemical Research* **2006**, *39*, 334-342.
[136] L. Dong, W. Li, W.-S. Li, *Nanoscale* **2011**, *3*, 3447-3461.
[137] X. Zhang, X. Jiang, K. Zhang, L. Mao, J. Luo, C. Chi, H. S. O. Chan, J. Wu, *The Journal of Organic Chemistry* **2010**, *75*, 8069-8077.

[138] A. P. H. J. Schenning, E. W. Meijer, *Chemical Communications* **2005**, *0*, 3245-3258.
[139] B. R. Kaafarani, *Chem. Mat.* **2010**, *23*, 378-396.
[140] X. Feng, M. Liu, W. Pisula, M. Takase, J. Li, K. Müllen, *Advanced Materials* **2008**, *20*, 2684-2689.
[141] J. S. Wu, W. Pisula, K. Müllen, *Chemical Reviews* **2007**, *107*, 718-747.
[142] S. Ito, P. T. Herwig, T. Bohme, J. P. Rabe, W. Rettig, K. Müllen, *Journal of the American Chemical Society* **2000**, *122*, 7698-7706.
[143] F. Jäckel, M. Ai, J. Wu, K. Müllen, J. P. Rabe, *Journal of the American Chemical Society* **2005**, *127*, 14580-14581.
[144] P. Samorì, A. Fechtenkötter, F. Jäckel, T. Böhme, K. Müllen, J. P. Rabe, *Journal of the American Chemical Society* **2001**, *123*, 11462-11467.
[145] P. Samorì, A. Fechtenkötter, E. Reuther, M. Watson, N. Severin, K. Müllen, J. Rabe, *Advanced Materials* **2006**, *18*, 1317-1321.
[146] D. Wasserfallen, I. Fischbach, N. Chebotareva, M. Kastler, W. Pisula, F. Jackel, M. D. Watson, I. Schnell, J. P. Rabe, H. W. Spiess, K. Müllen, *Advanced Functional Materials* **2005**, *15*, 1585-1594.
[147] X. L. Feng, W. Pisula, T. Kudernac, D. Q. Wu, L. J. Zhi, S. De Feyter, K. Müllen, *Journal of the American Chemical Society* **2009**, *131*, 4439-4448.
[148] X. L. Feng, J. S. Wu, M. Ai, W. Pisula, L. J. Zhi, J. P. Rabe, K. Müllen, *Angewandte Chemie-International Edition* **2007**, *46*, 3033-3036.
[149] A. P. H. J. Schenning, P. Jonkheijm, F. J. M. Hoeben, J. van Herrikhuyzen, S. C. J. Meskers, E. W. Meijer, L. M. Herz, C. Daniel, C. Silva, R. T. Phillips, R. H. Friend, D. Beljonne, A. Miura, S. De Feyter, M. Zdanowska, H. Uji-i, F. C. De Schryver, Z. Chen, F. Würthner, M. Mas-Torrent, D. den Boer, M. Durkut, P. Hadley, *Synthetic Metals* **2004**, *147*, 43-48.
[150] J. Puigmartí-Luis, A. Minoia, H. Uji-i, C. Rovira, J. Cornil, S. De Feyter, R. Lazzaroni, D. B. Amabilino, *Journal of the American Chemical Society* **2006**, *128*, 12602-12603.
[151] A. Miura, Z. Chen, H. Uji-i, S. De Feyter, M. Zdanowska, P. Jonkheijm, A. P. H. J. Schenning, E. W. Meijer, F. Würthner, F. C. De Schryver, *Journal of the American Chemical Society* **2003**, *125*, 14968-14969.
[152] H. Uji-i, A. Miura, A. Schenning, E. W. Meijer, Z. Chen, F. Würthner, F. C. De Schryver, M. Van der Auweraer, S. De Feyter, *ChemPhysChem* **2005**, *6*, 2389-2395.
[153] J. Zhang, F. J. M. Hoeben, M. J. Pouderoijen, A. P. H. J. Schenning, E. W. Meijer, F. C. De Schryver, S. De Feyter, *Chemistry – A European Journal* **2006**, *12*, 9046-9055.
[154] M. Rief, M. Gautel, F. Oesterhelt, J. M. Fernandez, H. E. Gaub, *Science* **1997**, *276*, 1109-1112.
[155] M. Rief, F. Oesterhelt, B. Heymann, H. E. Gaub, *Science* **1997**, *275*, 1295-1297.
[156] G. Francius, D. Alsteens, V. Dupres, S. Lebeer, S. De Keersmaecker, J. Vanderleyden, H. J. Gruber, Y. F. Dufrene, *Nature Protocols* **2009**, *4*, 939-946.

[157] Y. Gilbert, M. Deghorain, L. Wang, B. Xu, P. D. Pollheimer, H. J. Gruber, J. Errington, B. Hallet, X. Haulot, C. Verbelen, P. Hols, Y. F. Dufrêne, *Nano Letters* **2007**, *7*, 796-801.
[158] J. J. Heinisch, V. Dupres, D. Alsteens, Y. F. Dufrene, *Nature Protocols* **2010**, *5*, 670-677.
[159] N. Liu, T. Bu, Y. Song, W. Zhang, J. Li, W. Zhang, J. Shen, H. Li, *Langmuir* **2010**, *26*, 9491-9496.
[160] S. A. Claridge, J. J. Schwartz, P. S. Weiss, *ACS Nano* **2011**, *5*, 693-729.
[161] T. Puntheeranurak, I. Neundlinger, R. K. H. Kinne, P. Hinterdorfer, *Nature Protocols* **2011**, *6*, 1443-1452.
[162] T. Hoffmann, L. Dougan, *Chemical Society Reviews* **2012**, *41*, 4781-4796.
[163] L. A. Wenzler, G. L. Moyes, G. N. Raikar, R. L. Hansen, J. M. Harris, T. P. Beebe, L. L. Wood, S. S. Saavedra, *Langmuir* **1997**, *13*, 3761-3768.
[164] Y. Z. Liu, S. H. Leuba, S. M. Lindsay, *Langmuir* **1999**, *15*, 8547-8548.
[165] M. Schneider, M. Zhu, G. Papastavrou, S. Akari, H. Möhwald, *Langmuir* **2002**, *18*, 602-606.
[166] Y. Zhang, C. Liu, W. Shi, Z. Wang, L. Dai, X. Zhang, *Langmuir* **2007**, *23*, 7911-7915.
[167] M. Kudera, C. Eschbaumer, H. E. Gaub, U. S. Schubert, *Advanced Functional Materials* **2003**, *13*, 615-620.
[168] G. Hummer, A. Szabo, *Accounts of Chemical Research* **2005**, *38*, 504-513.
[169] L. Grill, K.-H. Rieder, F. Moresco, S. Stojkovic, A. Gourdon, C. Joachim, *Nano Letters* **2006**, *6*, 2685-2689.
[170] V. K. Yadavalli, J. G. Forbes, K. Wang, *Langmuir* **2006**, *22*, 6969-6976.
[171] M. E. Drew, A. Chworos, E. Oroudjev, H. Hansma, Y. Yamakoshi, *Langmuir* **2009**, *26*, 7117-7125.
[172] M. Geisler, B. N. Balzer, T. Hugel, *Small* **2009**, *5*, 2864-2869.
[173] N. de Souza, *Nature Methods* **2012**, *9*, 873-877.
[174] M. Frei, S. V. Aradhya, M. Koentopp, M. S. Hybertsen, L. Venkataraman, *Nano Letters* **2011**, *11*, 1518-1523.
[175] B. C. Stipe, M. A. Rezaei, W. Ho, *Physical Review Letters* **1999**, *82*, 1724-1727.
[176] J. I. Pascual, *Physical Review Letters* **2001**, *86*, 1050-1053.
[177] M. Grobus, *Physical Review Letters* **2005**, *94*, 136802.
[178] N. Tao, *Journal of Materials Chemistry* **2005**, *15*, 3260-3263.
[179] B. Xu, N. J. Tao, *Science* **2003**, *301*, 1221-1223.
[180] C. Li, I. Pobelov, T. Wandlowski, A. Bagrets, A. Arnold, F. Evers, *Journal of the American Chemical Society* **2008**, *130*, 318-326.
[181] W. Haiss, R. J. Nichols, H. van Zalinge, S. J. Higgins, D. Bethell, D. J. Schiffrin, *Physical Chemistry Chemical Physics* **2004**, *6*, 4330-4337.
[182] W. Haiss, H. van Zalinge, D. Bethell, J. Ulstrup, D. J. Schiffrin, R. J. Nichols, *Faraday Discuss* **2006**, *131*, 253-264.
[183] J. L. Xia, I. Diez-Perez, N. J. Tao, *Nano Letters* **2008**, *8*, 1960-1964.
[184] K. Liu, X. Wang, F. Wang, *ACS Nano* **2008**, *2*, 2315-2323.
[185] Q. Lu, K. Liu, H. Zhang, Z. Du, X. Wang, F. Wang, *ACS Nano* **2009**, *3*, 3861-3868.

[186] A. Mishchenko, D. Vonlanthen, V. Meded, M. Bürkle, C. Li, I. V. Pobelov, A. Bagrets, J. K. Viljas, F. Pauly, F. Evers, M. Mayor, T. Wandlowski, *Nano Letters* **2009**, *10*, 156-163.
[187] T. Hines, I. Diez-Perez, J. Hihath, H. Liu, Z.-S. Wang, J. Zhao, G. Zhou, K. Müllen, N. Tao, *Journal of the American Chemical Society* **2010**, *132*, 11658-11664.
[188] S. Martin, W. Haiss, S. J. Higgins, R. J. Nichols, *Nano Letters* **2010**, *10*, 2019-2023.
[189] J. Hihath, C. Bruot, H. Nakamura, Y. Asai, I. Díez-Pérez, Y. Lee, L. Yu, N. Tao, *ACS Nano* **2011**, *5*, 8331-8339.
[190] E. Leary, M. T. González, C. van der Pol, M. R. Bryce, S. Filippone, N. Martín, G. Rubio-Bollinger, N. s. Agraït, *Nano Letters* **2011**, *11*, 2236-2241.
[191] M. Kiguchi, S. Nakashima, T. Tada, S. Watanabe, S. Tsuda, Y. Tsuji, J. Terao, *Small* **2012**, *8*, 726-730.
[192] Z. Li, T.-H. Park, J. Rawson, M. J. Therien, E. Borguet, *Nano Letters* **2012**, *12*, 2722-2727.
[193] Y. Jiang, Q. Huan, L. Fabris, G. C. Bazan, W. Ho, *Nature Chemistry* **2013**, *5*, 36-41.
[194] X. D. Chen, S. Lenhert, M. Hirtz, N. Lu, H. Fuchs, L. F. Chi, *Accounts of Chemical Research* **2007**, *40*, 393-401.
[195] S. S. Li, B. H. Northrop, Q. H. Yuan, L. J. Wan, P. J. Stang, *Accounts of Chemical Research* **2009**, *42*, 249-259.
[196] L. J. Wan, *Accounts of Chemical Research* **2006**, *39*, 334-342.
[197] T. Kudernac, S. B. Lei, J. Elemans, S. De Feyter, *Chemical Society Reviews* **2009**, *38*, 402-421.
[198] Z. C. Mu, L. J. Shu, H. Fuchs, M. Mayor, L. F. Chi, *Journal of the American Chemical Society* **2008**, *130*, 10840-10841.
[199] Z. C. Mu, X. Y. Yang, Z. Q. Wang, X. Zhang, *Langmuir* **2004**, *20*, 8892-8896.
[200] C. V. Yelamaggad, A. S. Achalkumar, D. S. S. Rao, S. K. Prasad, *The Journal of Organic Chemistry* **2007**, *72*, 8308-8318.
[201] V. Percec, E. Aqad, M. Peterca, J. G. Rudick, L. Lemon, J. C. Ronda, B. B. De, P. A. Heiney, E. W. Meijer, *Journal of the American Chemical Society* **2006**, *128*, 16365-16372.
[202] Liu, J. J. Gooding, *Langmuir* **2006**, *22*, 7421-7430.
[203] H. Sun, *The Journal of Physical Chemistry B* **1998**, *102*, 7338-7364.
[204] Z. Mu, Q. Shao, J. Ye, Z. Zeng, Y. Zhao, H. H. Hng, F. Y. C. Boey, J. Wu, X. Chen, *Langmuir* **2010**, *27*, 1314-1318.
[205] A. Stabel, P. Herwig, K. Müllen, J. P. Rabe, *Angewandte Chemie International Edition* **1995**, *34*, 1609.
[206] P. Samorí, N. Severin, C. D. Simpson, K. Müllen, J. P. Rabe, *Journal of the American Chemical Society* **2002**, *124*, 9454.
[207] F. Jäckel, M. Ai, J. Wu, K. Müllen, J. P. Rabe, *Journal of the American Chemical Society* **2005**, *127*, 14580.

[208] K. Tahara, S. Furukawa, H. Ujii, T. Uchino, T. Ichikawa, J. Zhang, W. Mamdouh, M. Sonoda, F. C. D. Schryver, S. D. Feyter, Y. Tobe, *Journal of the American Chemical Society* **2006**, *128*, 16613.
[209] R. Lazzaroni, A. Calderone, G. Lambin, J. P. Rabe, J. Brédas, *Synthetic Metals* **1991**, *525*, 41.
[210] D. J. Duchamp, R. E. March, *Acta Crystallographica* **1969**, *25*, 5.
[211] M. Lackinger, S. Griessl, W. A. Heckl, M. Hietschold, G. W. Flynn, *Langmuir* **2005**, *21*, 4984-4988.
[212] S. J. H. Griessl, M. Lackinger, F. Jamitzky, T. Markert, M. Hietschold, W. M. Heckl, *Langmuir* **2004**, *20*, 9403.
[213] F. J. M. Hoeben, P. Jonkheijm, E. W. Meijer, A. P. H. J. Schenning, *Chemical Reviews* **2005**, *105*, 1491-1546.
[214] M. M. S. Abdel-Mottaleb, S. De Feyter, M. Sieffert, M. Klapper, K. Müllen, F. C. De Schryver, *Langmuir* **2003**, *19*, 8256-8261.
[215] S. Stepanow, M. Lingenfelder, A. Dmitriev, H. Spillmann, E. Delvigne, N. Lin, X. B. Deng, C. Z. Cai, J. V. Barth, K. Kern, *Nature Materials* **2004**, *3*, 229-233.
[216] S. Stepanow, N. Lin, D. Payer, U. Schlickum, F. Klappenberger, G. Zoppellaro, M. Ruben, H. Brune, J. V. Barth, K. Kern, *Angewandte Chemie-International Edition* **2007**, *46*, 710-713.
[217] G. Schull, L. Douillard, C. Fiorini-Debuisschert, F. Charra, F. Mathevet, D. Kreher, A. J. Attias, *Nano Letters* **2006**, *6*, 1360-1363.
[218] Y. H. Liu, S. B. Lei, S. X. Yin, S. L. Xu, Q. Y. Zheng, Q. D. Zeng, C. Wang, L. J. Wan, C. L. Bai, *Journal of Physical Chemistry B* **2002**, *106*, 12569-12574.
[219] F. C. F, C. Santato, F. Rosei, *Topics in Current Chemistry* **2008**, *283*, 203.
[220] L. Kampschulte, M. Lackinger, A. K. Maier, R. S. K. Kishore, S. Griessl, M. Schmittel, W. M. Heckl, *Journal of Physical Chemistry B* **2006**, *110*, 10829.
[221] Z. Ma, Y. Y. Wang, P. Wang, H. Wei, Y. B. Li, S. B. Yang, Y. L. Yang, X. L. Fan, C. Wang, *ACS Nano* **2007**, *1*, 160.
[222] S. J. H. Griessl, M. Lackinger, F. Jamitzky, T. Markert, M. Hietschold, W. M. Heckl, *Journal of Physical Chemistry B* **2004**, *108*, 11556.
[223] L. Piot, A. Marchenko, J. Wu, K. Müllen, D. Fichou, *Journal of the American Chemical Society* **2005**, *127*, 16245.
[224] K. S. Novoselov, A. K. Geim, S. V. Morozov, D. Jiang, Y. Zhang, S. V. Dubonos, I. V. Grigorieva, A. A. Firsov, *Science* **2004**, *306*, 666-669.
[225] K. S. Novoselov, A. K. Geim, S. V. Morozov, D. Jiang, M. I. Katsnelson, I. V. Grigorieva, S. V. Dubonos, A. A. Firsov, *Nature* **2005**, *438*, 197-200.
[226] J. C. Meyer, A. K. Geim, M. I. Katsnelson, K. S. Novoselov, T. J. Booth, S. Roth, *Nature* **2007**, *446*, 60-63.
[227] M. H. Gass, U. Bangert, A. L. Bleloch, P. Wang, R. R. Nair, A. K. Geim, *Nature Nanotechnology* **2008**, *3*, 676-681.
[228] R. R. Nair, P. Blake, A. N. Grigorenko, K. S. Novoselov, T. J. Booth, T. Stauber, N. M. R. Peres, A. K. Geim, *Science* **2008**, *320*, 1308-1308.

[229] M. J. Allen, V. C. Tung, R. B. Kaner, *Chemical Reviews* **2009**, *110*, 132-145.
[230] M. Liu, X. B. Yin, E. Ulin-Avila, B. S. Geng, T. Zentgraf, L. Ju, F. Wang, X. Zhang, *Nature* **2011**, *474*, 64-67.
[231] L. P. Biro, P. Nemes-Incze, P. Lambin, *Nanoscale* **2012**, *4*, 1824-1839.
[232] R. S. Edwards, K. S. Coleman, *Nanoscale* **2013**, *5*, 38-51.
[233] F. N. Xia, T. Mueller, Y. M. Lin, A. Valdes-Garcia, P. Avouris, *Nature Nanotechnology* **2009**, *4*, 839-843.
[234] B. Sensale-Rodriguez, T. Fang, R. S. Yan, M. M. Kelly, D. Jena, L. Liu, H. L. Xing, *Applied Physics Letters***2011**, *99*.
[235] H. Zhang, D. Y. Tang, R. J. Knize, L. M. Zhao, Q. L. Bao, K. P. Loh, *Applied Physics Letters***2010**, *96*.
[236] J. L. Xu, X. L. Li, J. L. He, X. P. Hao, Y. Z. Wu, Y. Yang, K. J. Yang, *Applied Physics Letters***2011**, *99*.
[237] L. Prechtel, L. Song, D. Schuh, P. Ajayan, W. Wegscheider, A. W. Holleitner, *Nature Communications* **2012**, *3*.
[238] Q. L. Bao, H. Zhang, B. Wang, Z. H. Ni, C. H. Y. X. Lim, Y. Wang, D. Y. Tang, K. P. Loh, *Nature Photonics* **2011**, *5*, 411-415.
[239] F. Bonaccorso, Z. Sun, T. Hasan, A. C. Ferrari, *Nature Photonics* **2010**, *4*, 611-622.
[240] Q. Bao, K. P. Loh, *ACS Nano* **2012**, *6*, 3677-3694.
[241] P. Avouris, *Nano Letters* **2010**, *10*, 4285-4294.
[242] F. N. Xia, T. Mueller, R. Golizadeh-Mojarad, M. Freitag, Y. M. Lin, J. Tsang, V. Perebeinos, P. Avouris, *Nano Letters* **2009**, *9*, 1039-1044.
[243] J. Park, Y. H. Ahn, C. Ruiz-Vargas, *Nano Letters* **2009**, *9*, 1742-1746.
[244] T. Mueller, F. N. A. Xia, P. Avouris, *Nature Photonics* **2010**, *4*, 297-301.
[245] M. C. Lemme, F. H. L. Koppens, A. L. Falk, M. S. Rudner, H. Park, L. S. Levitov, C. M. Marcus, *Nano Letters* **2011**, *11*, 4134-4137.
[246] N. M. Gabor, J. C. W. Song, Q. Ma, N. L. Nair, T. Taychatanapat, K. Watanabe, T. Taniguchi, L. S. Levitov, P. Jarillo-Herrero, *Science* **2011**, *334*, 648-652.
[247] J. C. W. Song, M. S. Rudner, C. M. Marcus, L. S. Levitov, *Nano Letters* **2011**, *11*, 4688-4692.
[248] T. J. Echtermeyer, L. Britnell, P. K. Jasnos, A. Lombardo, R. V. Gorbachev, A. N. Grigorenko, A. K. Geim, A. C. Ferrari, K. S. Novoselov, *Nature Communications* **2011**, *2*.
[249] Y. Liu, R. Cheng, L. Liao, H. L. Zhou, J. W. Bai, G. Liu, L. X. Liu, Y. Huang, X. F. Duan, *Nature Communications* **2011**, *2*.
[250] F. H. L. Koppens, D. E. Chang, F. J. G. de Abajo, *Nano Letters* **2011**, *11*, 3370-3377.
[251] S. Thongrattanasiri, F. H. L. Koppens, F. J. G. de Abajo, *Physical Review Letters* **2012**, *108*.
[252] A. Hirsch, J. M. Englert, F. Hauke, *Accounts of Chemical Research* **2012**.
[253] J. Park, M. Yan, *Accounts of Chemical Research* **2012**.
[254] G. Konstantatos, M. Badioli, L. Gaudreau, J. Osmond, M. Bernechea, F. P. de Arquer, F. Gatti, F. H. Koppens, *Nature Nanotechnology* **2012**.

[255] Y. Lu, M. B. Lerner, Z. J. Qi, J. J. Mitala, J. H. Lim, B. M. Discher, A. T. C. Johnson, *Applied Physics Letters***2012**, *100*.
[256] B. Li, L. Zhou, D. Wu, H. L. Peng, K. Yan, Y. Zhou, Z. F. Liu, *ACS Nano* **2011**, *5*, 5957-5961.
[257] H. T. Liu, S. M. Ryu, Z. Y. Chen, M. L. Steigerwald, C. Nuckolls, L. E. Brus, *Journal of the American Chemical Society* **2009**, *131*, 17099-+.
[258] J. M. Englert, C. Dotzer, G. A. Yang, M. Schmid, C. Papp, J. M. Gottfried, H. P. Steinruck, E. Spiecker, F. Hauke, A. Hirsch, *Nature Chemistry* **2011**, *3*, 279-286.
[259] M. Nakaya, M. Aono, T. Nakayama, *ACS Nano* **2011**, *5*, 7830-7837.
[260] T. He, D. A. Corley, M. Lu, N. H. Di Spigna, J. L. He, D. P. Nackashi, P. D. Franzon, J. M. Tour, *Journal of the American Chemical Society* **2009**, *131*, 10023-10030.
[261] F. M. Koehler, A. Jacobsen, K. Ensslin, C. Stampfer, W. J. Stark, *Small* **2010**, *6*, 1125-1130.
[262] A. C. Ferrari, J. C. Meyer, V. Scardaci, C. Casiraghi, M. Lazzeri, F. Mauri, S. Piscanec, D. Jiang, K. S. Novoselov, S. Roth, A. K. Geim, *Physical Review Letters* **2006**, *97*.
[263] R. J. Nemanich, J. T. Glass, G. Lucovsky, R. E. Shroder, *J Vac Sci Technol A* **1988**, *6*, 1783-1787.
[264] N. Li, X. W. Li, S. Demiguel, X. G. Zheng, J. C. Campbell, D. A. Tulchinsky, K. J. Williams, T. D. Isshiki, G. S. Kinsey, R. Sudharsansan, *Ieee Photonic Tech L* **2004**, *16*, 864-866.
[265] H. Zhang, E. Bekyarova, J. W. Huang, Z. Zhao, W. Z. Bao, F. L. Wang, R. C. Haddon, C. N. Lau, *Nano Letters* **2011**, *11*, 4047-4051.
[266] W. J. Yu, L. Liao, S. H. Chae, Y. H. Lee, X. F. Duan, *Nano Letters* **2011**, *11*, 4759-4763.
[267] H. Xu, Y. Chen, W. Xu, H. Zhang, J. Kong, M. S. Dresselhaus, J. Zhang, *Small* **2011**, *7*, 2945-2952.
[268] H. Xu, Y. Chen, J. Zhang, H. Zhang, *Small* **2012**, *8*, 2833-2840.
[269] S. A. Crowe, L. N. Dossing, N. J. Beukes, M. Bau, S. J. Kruger, R. Frei, D. E. Canfield, *Nature* **2013**, *501*, 535-538.
[270] J. W. Draper, *A Text-book on Chemistry*, Harper & Brothers, New York **1862**.
[271] L. Li, W. Hu, H. Fuchs, L. Chi, *Advanced Energy Materials* **2011**, *1*, 188-193.
[272] F. W. Zeng, S. C. Zimmerman, *Chemical Reviews* **1997**, *97*, 1681-1712.
[273] L. H. Xie, Y. Z. Chang, J. F. Gu, R. J. Sun, J. W. Li, X. H. Zhao, W. Huang, *Acta Physico-Chimica Sinica* **2010**, *26*, 1784-1794.
[274] L. H. Y. Xie, C. R.; Lai, W. Y.; Fan, Q. L.; Huang, W., *Progress in Polymer Science* **2012**, *37*, 1192-1264.
[275] M. Halik, H. Klauk, U. Zschieschang, G. Schmid, S. Ponomarenko, S. Kirchmeyer, W. Weber, *Advanced Materials* **2003**, *15*, 917-922.
[276] B. Dong, F. Huo, L. Zhang, X. Yang, Z. Wang, X. Zhang, S. Gong, J. Li, *Chemistry- A European Journal* **2003**, *9*, 2331-2336.

[277] A. C. Grimsdale, K. Müllen, *Angewandte Chemie International Edition* **2005**, *44*, 5592-5629.
[278] J. Cai, P. Ruffieux, R. Jaafar, M. Bieri, T. Braun, S. Blankenburg, M. Muoth, A. P. Seitsonen, M. Saleh, X. Feng, K. Müllen, R. Fasel, *Nature* **2010**, *466*, 470-473.
[279] S. Hitosugi, W. Nakanishi, T. Yamasaki, H. Isobe, *Nature Communications* **2011**, *2*, 492.
[280] R. Jasti, J. Bhattacharjee, J. B. Neaton, C. R. Bertozzi, *Journal of the American Chemical Society* **2008**, *130*, 17646-17647.
[281] H. Takaba, H. Omachi, Y. Yamamoto, J. Bouffard, K. Itami, *Angewandte Chemie International Edition* **2009**, *48*, 6112-6116.
[282] L. T. Scott, E. A. Jackson, Q. Zhang, B. D. Steinberg, M. Bancu, B. Li, *Journal of the American Chemical Society* **2011**, *134*, 107-110.
[283] A. A. Fokin, L. V. Chernish, P. A. Gunchenko, E. Y. Tikhonchuk, H. Hausmann, M. Serafin, J. E. P. Dahl, R. M. K. Carlson, P. R. Schreiner, *Journal of the American Chemical Society* **2012**, *134*, 13641-13650.
[284] T. N. Hoheisel, S. Schrettl, R. Szilluweit, H. Frauenrath, *Angewandte Chemie International Edition* **2010**, *49*, 6496-6515.
[285] M. K. R. Fischer, T. E. Kaiser, F. Wurthner, P. Bauerle, *Journal of Materials Chemistry* **2009**, *19*, 1129-1141.
[286] M. Guo, X. Z. Yan, T. Goodson, *Advanced Materials* **2008**, *20*, 4167-4171.
[287] K. R. J. Thomas, A. L. Thompson, A. V. Sivakumar, C. J. Bardeen, S. Thayumanavan, *Journal of the American Chemical Society* **2005**, *127*, 373-383.
[288] X. Y. Cao, W. B. Zhang, J. L. Wang, X. H. Zhou, H. Lu, J. Pei, *Journal of the American Chemical Society* **2003**, *125*, 12430-12431.
[289] A. Pron, M. Baumgarten, K. Mullen, *Org. Lett.* **2010**, *12*, 4236-4239.
[290] J. L. Wang, Z. M. Tang, Q. Xiao, Y. G. Ma, J. Pei, *Org. Lett.* **2009**, *11*, 863-866.
[291] T. S. Qin, W. Wiedemair, S. Nau, R. Trattnig, S. Sax, S. Winkler, A. Vollmer, N. Koch, M. Baumgarten, E. J. W. List, K. Mullen, *Journal of the American Chemical Society* **2011**, *133*, 1301-1303.
[292] X. L. Meng, W. H. Zhu, H. Tian, *Prog. Chem.* **2007**, *19*, 1671-1680.
[293] P. L. Burn, S. C. Lo, I. D. W. Samuel, *Advanced Materials* **2007**, *19*, 1675-1688.
[294] C. H. Chen, J. T. Lin, M. C. P. Yeh, *Org. Lett.* **2006**, *8*, 2233-2236.
[295] T. W. Kwon, M. M. Alam, S. A. Jenekhe, *Chem. Mat.* **2004**, *16*, 4657-4666.
[296] J. L. Wang, Y. Zhou, Y. F. Li, J. Pei, *Journal of Organic Chemistry* **2009**, *74*, 7449-7456.
[297] Z. H. Zhao, H. Jin, Y. X. Zhang, Z. H. Shen, D. C. Zou, X. H. Fan, *Macromolecules* **2011**, *44*, 1405-1413.
[298] G. J. Zhou, W. Y. Wong, B. Yao, Z. Y. Xie, L. X. Wang, *Angewandte Chemie International Edition* **2007**, *46*, 1149-1151.
[299] S. C. Lo, P. L. Burn, *Chemical Reviews* **2007**, *107*, 1097-1116.

[300] C. Q. Ma, E. Mena-Osteritz, T. Debaerdemaeker, M. M. Wienk, R. A. J. Janssen, P. Bauerle, *Angewandte Chemie International Edition* **2007**, *46*, 1679-1683.
[301] J. L. Wang, C. M. Zhong, Z. M. Tang, H. B. Wu, Y. G. Ma, Y. Cao, J. Pei, *Chemistry – An Asian Journal* **2010**, *5*, 105-113.
[302] W. Y. Lai, R. D. Xia, Q. Y. He, P. A. Levermore, W. Huang, D. D. C. Bradley, *Advanced Materials* **2009**, *21*, 355-360.
[303] W. Y. Lai, Q. Y. He, R. Zhu, Q. Q. Chen, W. Huang, *Advanced Functional Materials* **2008**, *18*, 265-276.
[304] N. Niamnont, R. Mungkarndee, I. Techakriengkrai, P. Rashatasakhon, M. Sukwattanasinitt, *Biosens. Bioelectron.* **2010**, *26*, 863-867.
[305] X. H. Li, Z. Chen, Q. Zhao, L. Shen, F. Y. Li, T. Yi, Y. Cao, C. H. Huang, *Inorganic Chemistry* **2007**, *46*, 5518-5527.
[306] K. Bronk, S. Thayumanavan, *Journal of Organic Chemistry* **2003**, *68*, 5559-5567.
[307] D. J. Liu, S. De Feyter, M. Cotlet, U. M. Wiesler, T. Weil, A. Herrmann, K. Mullen, F. C. De Schryver, *Macromolecules* **2003**, *36*, 8489-8498.
[308] R. Bauer, D. Liu, A. V. Heyen, F. De Schryver, S. De Feyter, K. Müllen, *Macromolecules* **2007**, *40*, 4753-4761.
[309] Y.-Z. Chang, Q. Shao, L.-Y. Bai, C.-J. Ou, J.-Y. Lin, L.-H. Xie, Z.-D. Liu, X. Chen, G.-W. Zhang, W. Huang, *Small* **2013**, doi:10.1002/smll.201300065.
[310] M. H. Dishner, J. C. Hemminger, F. J. Feher, *Langmuir* **1996**, *12*, 6176-6178.
[311] J. Youn, G. R. Dholakia, H. Huang, J. W. Hennek, A. Facchetti, T. J. Marks, *Advanced Functional Materials* **2012**, *22*, 1856-1869.
[312] E. A. Weiss, G. K. Kaufman, J. K. Kriebel, Z. Li, R. Schalek, G. M. Whitesides, *Langmuir* **2007**, *23*, 9686-9694.
[313] E. A. Weiss, G. K. Kaufman, J. K. Kriebel, Z. Li, R. Schalek, G. M. Whitesides, *Langmuir* **2007**, *23*, 9686-9694.
[314] V. B. Engelkes, J. M. Beebe, C. D. Frisbie, *Journal of the American Chemical Society* **2004**, *126*, 14287-14296.
[315] B. Kim, S. H. Choi, X. Y. Zhu, C. D. Frisbie, *Journal of the American Chemical Society* **2011**, *133*, 19864-19877.
[316] H. J. Lee, J. Lee, S.-M. Park, *Journal of Physical Chemistry B* **2010**, *114*, 2660-2666.
[317] Y. Domi, M. Ochida, S. Tsubouchi, H. Nakagawa, T. Yamanaka, T. Doi, T. Abe, Z. Ogumi, *J. Phys. Chem. C* **2011**, *115*, 25484-25489.
[318] D. A. Kamkar, M. Wang, F. Wudl, T.-Q. Nguyen, *ACS Nano* **2012**, *6*, 1149-1157.
[319] P. Huang, H. Zhu, L. Jing, Y. Zhao, X. Gao, *ACS Nano* **2011**, *5*, 7945-7949.
[320] R. Sharma, J. H. Baik, C. J. Perera, M. S. Strano, *Nano Letters* **2010**, *10*, 398-405.
[321] S. Milanesi, M. Fagnoni, A. Albini, *The Journal of Organic Chemistry* **2004**, *70*, 603-610.

[322] O. Haak, C.-B. Jeoung, A. Pawlik, P. Boldt, W. Grahn, C.-B. J. A. P. P. B. W. G. F.-H. K. H. L. H.-P. Weitzel, F.-H. Kreuzer, H. Leigeber, H.-P. Weitzel, *Journal of Chemical Research, Synopses* **1998**, 630-631.

[323] H. Watanabe, C. Manabe, T. Shigematsu, M. Shimizu, *Applied Physics Letters***2001**, *78*, 2928-2930.

[324] T. Nakayama, O. Kubo, Y. Shingaya, S. Higuchi, T. Hasegawa, C.-S. Jiang, T. Okuda, Y. Kuwahara, K. Takami, M. Aono, *Advanced Materials* **2012**, *24*, 1675-1692.